POLITECNICO DI MILANO
DIPPARTIMENTO DI ELETTRONICA E INFORMAZIONE
DOCTORAL PROGRAMME INFORMATION TECHNOLOGY

A TOTAL ATTENUATION TIME SERIES SYNTHESIZER FOR NON-GEOSTATIONARY SATELLITE LINKS

Doctoral Dissertation of:
Luciano Machado Tomaz

Supervisor:
Prof. Carlo Capsoni

Tutor:
Prof. Carlo Riva

The Chair of the Doctoral Program:
Prof. Barbara Pernici

2020 – XXXI Cycle

Abstract

THE development of space communications is increasingly dependent on the direct knowledge (satellite experiments) and on the output of ad-hoc developed tools (prediction methods) that enable to understand and quantify the main impairments affecting wave propagation. In recent times, the high frequency bands (Ku and Ka) are extensively used in commercial and military applications while the Q/V bands are expected to be used in the next future. It follows that the knowledge and the study of the propagation problems at such very broad range have become a critical issue. Moreover, the Low Earth Orbit (LEO) and Middle Earth Orbit (MEO) satellites, widely used in remote sensing and Earth Observation (EO) applications, are nowadays becoming more and more interesting also for television broadcasting and direct-to-user communications due to the fact of being closer to the Earth surface. These satellite configurations have shorter orbital periods with respect to GEO and lower signal propagation delays. Also, since the signal propagation paths are shorter, the requested transmission power is also smaller, which allows building small and low-cost satellites (although in a larger number). While in the geostationary satellites (GEO) applications the position (geometrical parameters) of the link remains static and only the weather presents variability, in non-GEO (NGEO) satellites applications, in addition to the meteorological changes, it is necessary to consider that the satellite in the short orbital period is seen from the ground station at variable values of azimuth and elevation thus making the modelling task very challenging. This thesis presents a model of a Total Attenuation Time Series Synthesizer for NGEO satellite links. The development of time series synthesizers allows the simulation of the time varying condition of the channel and represents the today most advanced propagation prediction tool. In fact, a time series synthesizer is the basic instrument for the development and testing of the Propagation Impairment Mitigation Techniques (PIMTs), which represent the best approach for an effective design of a satellite communication system operating at microwave frequencies.

Keywords:Propagation; NGEO Satellites; Tropospheric Attenuation.

Acknowledgements

First and foremost I would like to thank God. You have given me the grace and the strength to complete this work. I could never have done this without the faith I have in You, the Almighty.

I want to express my profound gratitude to my supervisor, Carlo Capsoni, for his support during these four years. I am also thankful to professor Lorenzo Luini, who contributed with his knowledge for the development of this work. I would like to extend my sincere thanks to my friends from the department: Atul, Eric, Dario, Alberto, Marouan, and Omran, for their friendship and support.

I cherish the friendship I had and take this opportunity to thank each one of my friends who have been an inestimable encouragement. My Brazilian friends Paulo, Ewerton (a.k.a. Abel), Isabel, Mara, Davide (almost a Brazilian guy), and Ulisses Trevisan.

Finally, I express my deep gratitude for my family: My wife, Lucimar, my son, Victor, and my parents (*in memoriam*), Geraldo Eci Tomaz and Geralda Custódia Machado Tomaz, to whom I owe everything.

Il y a dans le monde et qui marche parallèlement à la force de mort et de contrainte, une force énorme de persuasion qui s'appelle la culture.

— Albert Camus

To my parents (*in memoriam*)
A.M.D.G.

Contents

List of Figures

List of Tables

CHAPTER 1

Introduction

SINCE the first well know article published in 1945 by Arthur C. Clark [1] — where the characteristics of the synchronous orbit are discussed together with the possibility of global coverage with only three satellites — and the first in-orbit satellite, Sputnik, launched in October 4, 1957 by the USRR, satellite-based communications experienced a rapid development and nowadays they are exploring new areas and new applications. The horizon of the satellite systems applications has expanded far beyond its first ambitions. Remote sensing and Earth Observation (EO), e.g., are currently two of the most significant fields of satellite applications, but the list also includes atmospheric monitoring, space exploration, military secure communications, spying, and so on [2]. This progression is still requiring an increase research effort towards the development of new more advanced models and technologies, and the setup of experiments to fully analyse advantages and limitations of using of the microwave frequency bands.

We can define a communication satellite basically as an electronic package placed in orbit whose primary objective is to initiate or assist communication transmission or messages from one point to another through the space [3]. There are, in general, four types of satellites classified according to the height of the orbit: GEO (Geostationary); HEO (High Elliptical Orbiting); MEO (Middle-Earth Orbiting); and LEO (Low-Earth Orbiting).

Satellites can also be classified according to the in-orbit mass and specifically there are large, medium, mini, micro, nano, pico or femto satellites. This classification is shown in Table 1.1. The group that goes from femto to mini satellites is also named small satellites [3].

The satellite services are defined by the International Telecommunication Union (ITU) and include the following:

Table 1.1: *Classification according to the in-orbit mass*

Satellite class	In-orbit mass (kg)
Large	>1000
Medium	500-1000
Mini	100-500
Micro	10-100
Nano	1-10
Pico	0.1-1
Femto	<0.1

- Fixed Satellite Services (FSS) that supports the communication between antennas that are in positioned in fixed points;
- Broadcast Satellite Services (BSS) that use high powered beams to deliver radio and television to the users;
- and Mobile Satellite Services (MSS) that provide telecommunications services to users that are potentially moving with their terminals. Nowadays it includes connectivity not only for land-based users, but also for maritime and aeronautical ones.

The satellite communications technology has been developing rapidly in the last decades in order to seek increasingly larger bandwidths as requested by new services. This requires the use of higher and higher frequency carriers (in the Ka and Q/V bands) to allow for the development of broadband systems with terabyte data traffic. At such frequencies the extra path attenuation due to the constituents of the atmosphere in the different meteorological situations can be very severe. Other effects include, depolarization, scintillations (i.e. rapid fluctuations of the magnitude, frequency, phase or polarization caused by turbulences in the atmosphere) and reduction of coherence bandwidth of the signal. Besides these issues, satellite communication networks have several advantages such as the possibility of a global coverage, scalability, broadcasting capability, and reliability. According to [4] satellite-based services are "an excellent candidate to provide broadband integrated Internet access".

1.1 GEO Satellites

A satellite is defined as geosynchronous when the height of the orbit is around 35,786 km, the orbit inclination close to zero degrees and an eccentricity lower than 0.001. The angular rotation of the satellite is the same of the Earth around its axis. At the beginning of this century there were around 200 geostationary satellites in orbit around the world [5]. Today, they are 376 according to [6].

The advantages of GEO satellites can be summarized as follows: it is possible to provide a global coverage (with the exception of the polar areas) with only three GEO satellites; they can be continuously connected to the Earth; they are able to generate spot beams continuously pointed towards the regions of desired coverage and the in-orbit lifetimes are longer in comparison with what can be obtained with other orbits (between 15 and 20 years). Nonetheless, GEO satellites have also some drawbacks: as the distance between the ground and the satellite is extremely large, the free space path

loss (FSO) is also large, as it increases with the square of the distance; the signal delay is important (in the order of one quarter of second); and their costs are quite high [7].

1.2 Non-GEO Satellites

The increasing demand for communications services on-the-move — e.g. video, music, voice — is creating a window of opportunity for the non-geostationary satellite systems. New constellations, like the O3b mPOWER [8],aim to provide a large range of services with great flexibility, efficiency, and scalability in a network that includes both GEO and NGEO (Non-GEO) satellites. There are basically three configurations of NGEO satellites:

HEO satellites: they follow an elliptical orbit which distance from the Earth surface varies between 18,000 and 35,000 km and the swing is used to optimize the coverage in specific zones [3]. In general, they are used for providing a better coverage in the areas at high North or South latitudes.

MEO orbits are, in turn, circular and range from 8,000 to 18,000 km above Earth's surface. In comparison to GEO, MEO satellites have lower costs and signal delays, but more satellites are required to provide the full Earth coverage. Also, the FSO for MEO satellite links is inherent lower with respect to the GEO links due to the shorter distance. A MEO constellation is able to provide a global coverage with few satellites (few as 10, with orbital period ranging from 8 to 12 hours [9]) and also the tracking, telemetry, and command (TT&C) system is not so complex.

LEO satellites, in turn, occupy orbits ranging from 160 to 1,600 km above the Earth's surface and are suitable for mass production techniques due to their small size and easiness to be launched when compared to MEO, HEO, and GEO systems. LEO satellite links can reach now almost any latitude. LEO orbits are designed in order to assure that satellite's altitude is high enough to avoid significant deceleration due to atmospheric friction, and low enough to avoid intense levels of protons bombardment in the inner Van Allen belt [9]. The orbital inclination angle ranges from 0°(equatorial) to 90°(polar) and also slightly beyond (sun-synchronous) [3]. The low orbit leads to short orbital periods, which require a larger number of satellites, but smaller propagation delay. LEO orbits can also be adjusted in order to concentrate the coverage at lower latitudes [7].

Since the signal propagation path is shorter, the required transmission power is also smaller, which allows building small and low-cost satellites. However, as the orbital period is shorter, a LEO satellites constellation is needed for a 24-hour coverage. Each satellite within the constellation has a fixed position with respect to the others, and acts as a switching node while connected to its neighbours by intersatellite links (ISL). For continuous time coverage with a minimum outage, the number of satellites of the constellation must be increased; their number depends on the orbit of the satellite, the beamwidth of the onboard and of the earth station antennas and the traffic handling capacity. An example of LEO constellation is Iridium, consisting in 66 satellites distributed in six orbital planes, that was deployed in 1998. Each satellite in this constellation has 48 spot beams and four neighbours are connected by ISL operating at K band.

With the developments expected in the next future, it will be possible to access

residential meter readings, access vehicle plates, and monitor traffic flow. LEO satellite systems are in general classified in two types: "Big LEO" and "Little LEO" systems. The ”Big LEO” systems have a big number of satellites between 10 and 66 and are mostly devoted to personal voice communications. Systems called "Little LEO" are smaller not only in terms of number of satellites but also in relation to their overall capability, and are thought to provide services like paging, messaging and position location.

While in GEO applications the position, and therefore the geometrical parameters of the radio link, remain static and only the meteorological conditions varies in time, in LEO applications in addition to the meteorological changes, it is necessary to consider the satellite movement in a short orbital period both in azimuth and in elevation and it makes the modelling task very challenging. In fact, the minimum and maximum ranges during each passage of the satellite is dependent on the orbital altitude while the probability distribution function (PDF) of the elevation angles of the satellite as seen by the Earth station is affected by the orbital inclination angle and the latitude of the ground station.

The development of time series synthesizers allows the simulation of the time varying condition of the channel and represents the today most advanced propagation prediction tool. In fact, a time series synthesizer is the basic instrument for the development and testing of the Propagation Impairment Mitigation Techniques (PIMTs), which represent the best approach for an effective design of advanced satellite communication systems operating at microwave frequencies.

1.3 Propagation Atmospheric Impairments

It is known that slant path radiowave propagation is affected by atmospheric impairments [5]. Propagation phenomena are mainly originated in the troposphere (the lowest part of the atmosphere around the Earth up to about 16 km in height) and in the ionosphere (from about 60 km to 450 km of altitude). Because we are interested in frequencies above 10 GHz [10], the effect of the ionosphere is almost negligible and as such we will focus our attention only on the tropospheric propagation. Figure 1.1 shows the pressure and temperature profiles along the layers of the atmosphere.

The troposphere is the lowest layer of the atmosphere and contains around 80% of the mass present in the atmosphere and 99% of the water vapor, which concentration changes with the latitude [11]. It is within the troposphere that the Earth-space links experience the major propagation impairments, which are caused by the presence of both gaseous (especially water vapor and oxygen) and hydrometeors constituents (rain, snow, cloud particles, etc.). The most important impairments are: attenuation, depolarization, increasing in thermal noise of the system, amplitude and phase scintillations (particularly at low elevation angles), change in the angle-of-arrival of the signal, and amplitude and phase dispersion (of specific interest for wideband transmissions). These effects are highly dependent on the link parameters such as: frequency of operation, elevation angle, ground-station altitude, and local meteorology [12]. The thickness of the troposphere changes in function of the latitude, decreasing from the equator (around 16 km) to the poles (8-12 km).

The troposphere is the lowest layer of the atmosphere and contains around 80% of

the mass present in the atmosphere and 99% of the water vapor which concentration changes with the latitude [11]. It is within the troposphere that the Earth-space links experience the major propagation impairments, which due to the presence of both gaseous (especially water vapor and oxygen) and hydrometeors constituents (rain, snow, cloud particles, etc.) in this layer. The most important impairments that occur in the troposphere are: attenuation, depolarization, increasing in thermal noise of the system, amplitude and phase scintillations (particularly for low elevation angles), change in the angle-of-arrival of the signal, and amplitude and phase dispersion (especially for wideband transmissions). These impairments are highly dependent on the following parameters of the link: frequency of operation, elevation angle, ground-station altitude, and local meteorology [12]. The thickness of the troposphere changes in function of the latitude, decreasing from the equator (around 16 km) to the poles (8-12 km).

Table 1.2 shows the various frequency bands used for satellite communications.

At Ku band, the fade margin of the system can be increased in order to compensate for the extra path attenuation due to rain. However, at higher frequencies the fade levels are so large that it is not feasible either technically and/or economically to use this approach and more sophisticated techniques must be implemented (PIMTs) [13]. Nevertheless, moving to higher frequencies offers several advantages: a less congested spectrum, higher available bandwidth, a reduced interference potential and higher possibility of miniaturization [14]. As the economics of the satellite communication depends strongly on system size, the miniaturization, especially of the antennas, is a key feature.

1.3.1 Gaseous Attenuation

Oxygen and water vapor are the atmospheric gases attenuating the millimetre waves, through an absorption process. This process occurs as the result of a quantum level change in the rotation energy of the molecule that happens at a specific resonant frequency [12]. The molecules of oxygen and water vapor have permanent electric and magnetic dipole moments that are excited by the electromagnetic waves, oscillating and rotating. In this process the molecules absorb energy which is reradiated isotropically [15]. The other atmospheric components, like nitrogen, argon and carbon dioxide, have no resonance frequencies up to 100 GHz and their effect can be neglected [12].

Table 1.2: *Microwave frequency bands for satellite communication [2]*

Band	Frequency (GHz)
L band	1-2
S band	2-4
C band	4-8
X band	8-12
Ku band	12-18
K band	18-27
Ka band	27-40
V band	40-74
W band	75-110

1.3.2 Clouds and Fog Attenuation

Clouds attenuation is associated with the presence of suspended droplets (cloud liquid water content), however, according to [16], for frequencies beyond the Ka band also the effect of ice clouds is not negligible.

The clouds attenuation value is dependent on the link elevation being almost proportional to the path length [2]. Figure 1.2 shows how strongly dependent is the cloud attenuation on the frequency and on the link elevation.

Fog, in turn, has no significant impact on tropospheric propagation up to around 100 GHz. The typical liquid density in fog is between 0.05 g/m^3 (for medium fog) and 0.5 g/m^3 (for thick fog).

1.3.3 Tropospheric scintillations

The atmosphere, despite some degree of horizontal homogeneity, has an inherent inhomogeneity produced by turbulent motion [17]. Because of that, satellite links are also affected by tropospheric scintillations. Basically, scintillations are rapid fluctuations on the amplitude, phase, angle of arrival, and polarization of the signal. Scintillations increase with frequency and path length thus becoming very significant for low elevation angles. A prediction method for the estimation of scintillations along fixed satellite links is provided by the Recommendation ITU-R P.618-13 [18] while for LEO satellite links an interesting procedure is presented in [19].

Tropospheric scintillations have a strong correlation with temperature as well as with the humidity of air. The higher the temperature and the humidity, the higher is the amplitude of the tropospheric scintillation for a given earth-space link. There is also correlation with wind velocity: high correlation with wind speed but low correlation with its direction. The presence of rain along the path however does not affect significantly the amplitude of scintillations. The effect of rain in the scintillations is only related to the low frequency end of the power spectra [20].

The existence of clouds along the link is another factor that increases tropospheric scintillations. According to [5] there is a strong correlation between the presence of cumulus clouds and the intensity of tropospheric scintillation.

The amplitude of the scintillations depends also on the diurnal and seasonal cycles. The peaks coinciding with the most humid and hot periods. In addition, there is a dependence on the latitude and the effects of scintillations increase especially at higher latitudes. The variations in the longitude, on the other hand, for a fixed latitude seems to be negligible.

1.3.4 Rain Attenuation

Rain, in turn, is the strongest source of impairments in satellite links. Losses are caused mainly by raindrops absorption and scattering mechanisms. These effects occur at every frequency but are obviously more significant at the higher ones, where the wavelength is smaller and closer to the rain drop sizes. At frequencies above 10 GHz the imaginary part of the complex permittivity of water becomes significant and then it is not possible to consider the raindrop as a lossless dielectric [5]. Mathematically, the attenuation is the sum of the components produced by scattering and absorption. A

schematic presentation of both mechanisms is shown in Figure 1.3. In addition to attenuation, rain also causes depolarization. This effect is s more significant beyond 15 GHz and is caused by the flattering of the spherical raindrops exposed to the atmosphere drag [2].

The rain structures are usually classified in three types: cyclonic storm, convective rain and stratiform rain [12].

Cyclonic storms (or hurricanes) are circular storms with diameters ranging from 50 to 200 km. They move at a speed of 10 to 20 kilometres per hour. Their height to the melting layer can arrive to 8 km and the rain rates are much higher than 25 mm/h.

Convective rain structures have in general an extent of several kilometres and the duration of the highest rain rate is only several minutes. Convective rain cells extend to heights well above the average melting layer level due to the convective upwelling.

Stratiform, in turn, is the most common rain structure at mid-latitudes regions. They have an extension that can arrive to hundreds of kilometres and a duration exceeding one hour with rain rates well below 25 mm/h.

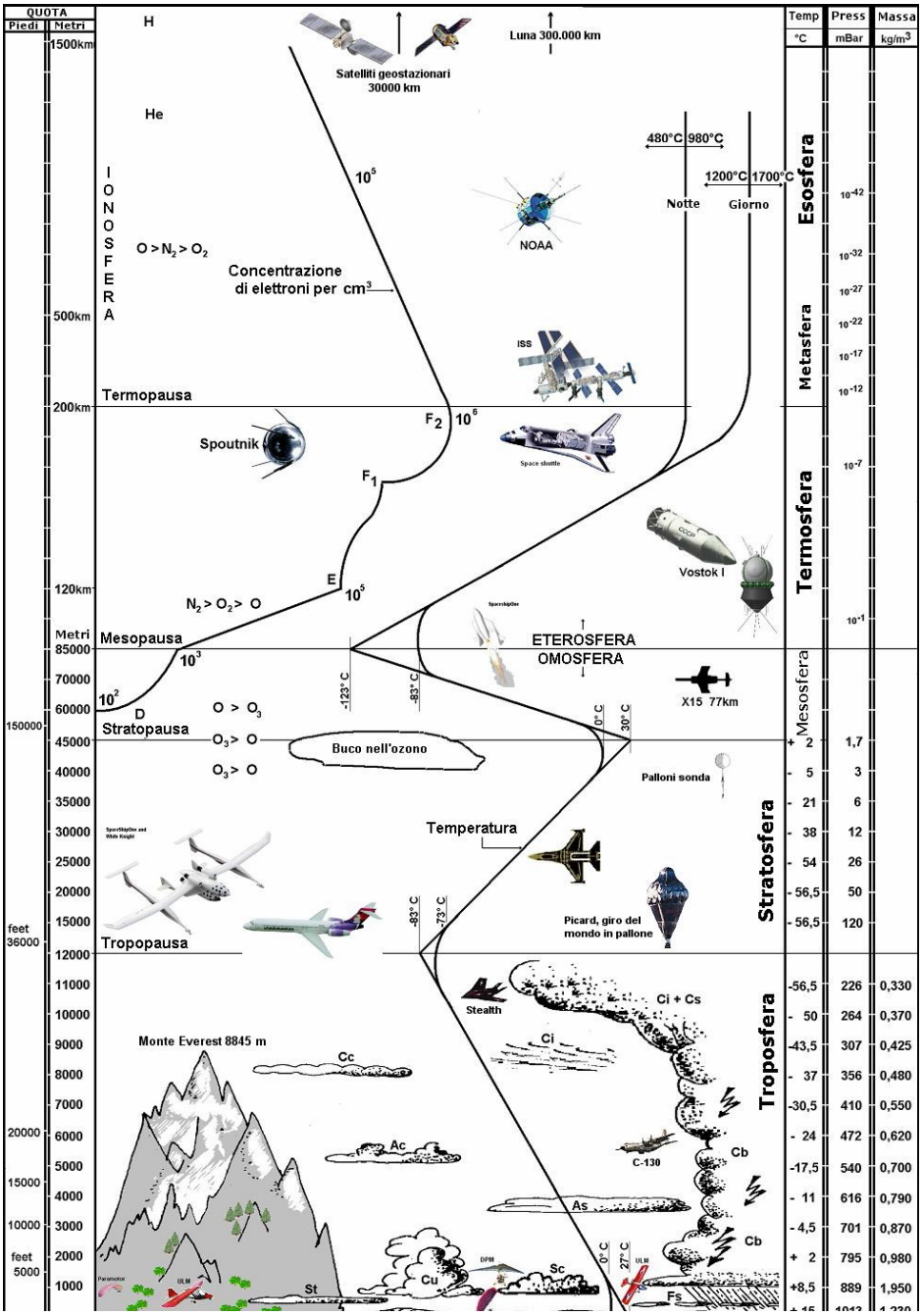

Figure 1.1: *Earth's atmosphere: pressure and temperature distribution [11]*

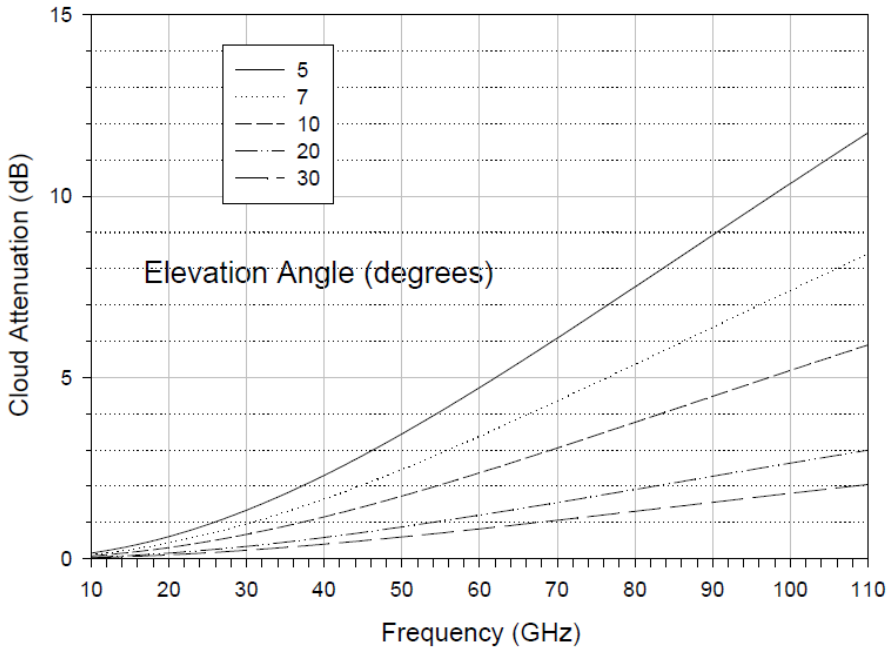

Figure 1.2: *Total cloud attenuation and its dependence on the frequency and on the elevation [12]*

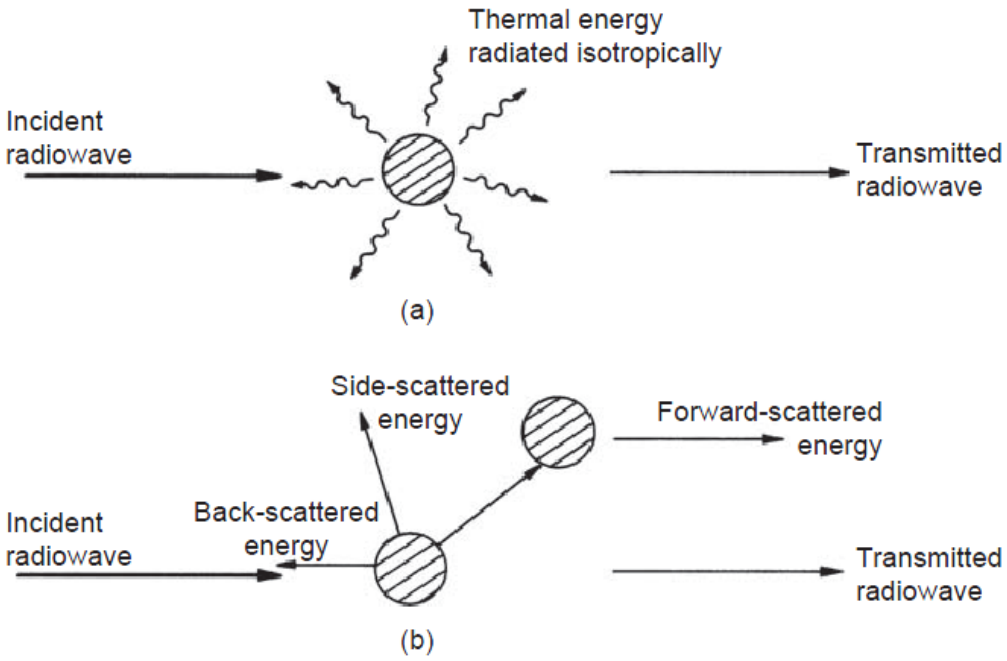

Figure 1.3: *The two mechanisms that causes losses in the electromagnetic wave while propagating trough a path filled with rain droplets [5]: (a) absorption; (b) scattering*

1.4 Propagation Impairment Mitigation Techniques

To make feasible the use of satellites operating at frequencies above 20 GHz where the extra path attenuations can be very high, it is necessary to adopt specific solutions because the standard technique of oversizing the power of the transmitters or the antennas sizes is not feasible and even not economic. Such specific solutions, indicated as PIMTs [21],used to enhance the Quality of Service (QoS) and availability of the system are based on the peculiarities of the propagation medium such as the spatial behaviour of the atmosphere. Some techniques make use of "resources" available also on board, such as a reconfigurable antenna and/or the adaptive coding and modulation (ACM) [11].

A sensing system detects the propagation impairment and, accordingly an algorithm chose the most adequate set of parameters of the selected PIMPT, in real time [22]. Basically, the attenuation effects can be counteracted by using power control, signal processing, and diversity techniques.

In general, PIMTs, independently of the type, perform the following functions:

- Monitor the quality of the link by means of continuous measurements of the propagation conditions;
- Provide the short-term estimation of the channel behaviour;
- Set the parameters of the system based on the short-term estimation.

1.4.1 Power Control Techniques

Essentially, the power control consists in the variation of the effective isotropic radiated power (EIRP) of the signal to enhance the carrier-to-noise ratio (C/N). Hence, the transmitter power is adjusted to compensate some modification in the dynamic characteristics of the channel. The adjustment can occur either at the ground station (uplink power control (ULPC) or earth station EIRP control) or at the satellite itself (downlink power control (DLPC) or satellite EIRP control). This power control can be implemented in two different ways: using an open loop control system, where the adjustment of the transmitted power is done based on the most recent measurements of the received power; or using a closed loop power control system, in which the adjustment is done based on reported power measurements over the channel.

1.4.2 Power Control Techniques

The possibility to compensate the degrading effects by using signal processing refers basically to adaptive transmission techniques, i.e., to modifications in the coding, modulation or data rate of the signal. These techniques can be classified in three categories, namely hierarchical coding (HC), hierarchical modulation (HM) and data rate reduction (DRR). The later one consists in the reduction of the information data rate during the periods in which the system monitoring indicates a deep fading. The HM reduces the spectral efficiency when the C/N decreases in function of the propagation impairments. The HC coding, on the other hand, is based on the increasing on the redundancy, thus decreasing the error probability [13].

1.4.3 Diversity Techniques

The diversity techniques are countermeasures against rain attenuation. As rain is the main factor of attenuation in satellite links, the diversity techniques are the most efficient PIMTs. There are different types of diversity that can be used to mitigate the fading, they are: site diversity (SD), orbital diversity (OD), frequency diversity (FD), and time diversity (TD). SD and OB are techniques exploring the knowledge on the spatial structure of rain. TD and FD are based on the temporal and spectral dependence of rain, respectively.

Site diversity consists in the use of two or more Earth stations, separated by a distance of at least 10 km, to receive the same information. This can be done because the heavy precipitation is usually concentrated in small areas, as the convective rain cells have in general a diameter that goes up to 10 km. The use of two differently located ground stations ensures that the probability of strong fading at both of them is significantly lower than the probability of strong fading at each individual site. From the signals received in the two sites, the less affected by fading or a combination of both (using techniques to maximize the C/N) is selected, thus increasing the system availability. Indeed, site diversity is in principle the most effective among the diversity techniques. Its application presents anyway some complexity since it requires a terrestrial link between the ground stations and it is very difficult to implement from the transmitter side [23]. The main parameters determining the gain of a site diversity system are the site separation and the baseline orientation angle. The former is the distance (D) between the Earth-stations and the latter is the angle (Φ) between the line joining the stations and the direction of the propagation path [12]. Figure 1.4 shows a diagram with a typical site diversity configuration with two Earth-stations. The optimal condition occurs when D is sufficiently large and Φ is closer to 90°.

However, site diversity become more complex to implement in case of Tx than in Rx as there is a need of a synchronization mechanism for the transmission chain of the ground stations that work in diversity mode.

The applicability of SD is generally economically unviable for counteracting fading at user terminals due to their low-cost requirements. This makes SD suitable for the gateways in the Satcom scenarios in which the availability is higher in the feeder-link than in the user-link.

Orbital diversity also called satellite diversity, consists basically in allowing the Earth station to choose between different satellites. It is less effective than site diversity due to the higher correlation between the paths. Due to the low gain provided by this technique, if it is not possible to take advantage of the capability for resource-sharing with several ground sites, the use of orbital diversity is economically unfeasible [12].

Frequency diversity is a technique that requires a payload operating in two different frequency bands. When a deep fade occurs, the traffic is switched to a lower frequency where however, the bandwidth is smaller and, with it, the capacity.

Time diversity is a relatively new technique that is applicable only to services where time delays can be tolerated. With this technique, the signal occurring during high fade periods is retransmitted by taking into account an estimation of the fade duration, i.e. it takes advantage of the rainfall process's time decorrelation. At the receiver, among the different copies of the transmitted information the one with the highest signal to noise ratio (SNR) is selected [24]. A further advantage is the economic aspect, because

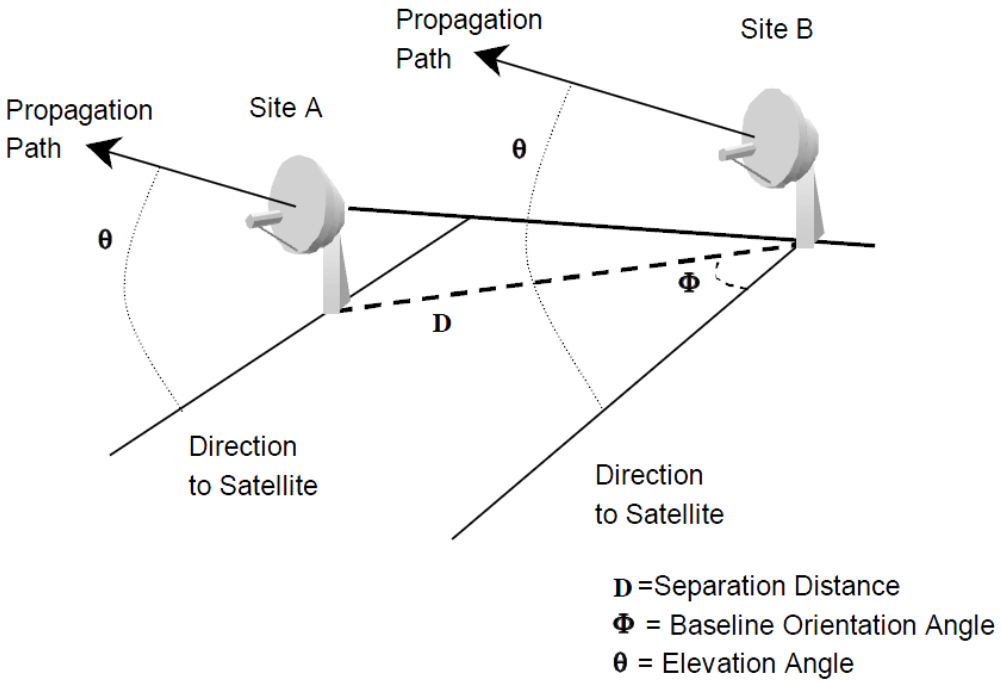

Figure 1.4: *Typical two site diversity configuration [5].*

this technique does not require to duplicate the network equipment. One of the main drawbacks is the reduction in the effective data rate. The references [13] and [21] provide a good overview and comparisons between the PIMTs.

1.5 Thesis outline

This subsection presents the structure and a brief summary of the next chapters.

- Chapter 2 presents a review on the attenuation time series synthesizers for satellite links that are present in the literature and their main characteristics, advantages, and disadvantages;
- Chapter 3 Provide an overview of the proposed total attenuation time series synthesizer for NGEO satellites;
- Chapter 4 describes the MultiEXCELL model and the rain maps database obtained from it that was used for the modelling procedures implemented in this work;
- Chapter 5 presents a model for scaling rain attenuation long-term statistics in function of the elevation angle and shows the results of this model applied to two different sites;
- Chapter 6 introduces a procedure to generate time series of rain attenuation for low elevation angles based in the summation of measured rain events present in the ITALSAT database;

- Chapter 7 presents a scaling model for time series that is able to receive as input a time series generated for a low elevation angle and scale it for all the range of elevations;
- Chapter 8 discuss the azimuthal variation of the attenuation due to rain and proposes a model to quantify this variation in a probability basis;
- Chapter 9 discuss the scaling in terms of elevation of clouds and water vapor attenuation in satellite links;
- Chapter 10 presents the application of the model as well as the fade duration and fade slope analysis;
- Chapter 11 draw some conclusions and proposes some future works.

CHAPTER 2

Review of Attenuation Time Series Synthesizers For Satellite Links

In this chapter we present an overview on the attenuation time series synthesizers (ATSS) for satellite communications available in the literature.

They represent the most sophisticated tool for the design of advanced satellite communication systems as they provide a statistically meaningful set of attenuation events with high temporal detail (one sample per second or even higher) that maintain the basic temporal dynamic properties of the radio channel.

2.1 Time Series Synthesizers

ATSS generate a set of time series that are similar to real measurements as they have the capability of reproducing the following characteristics of the channel:

- Long-term statistics of rain or total attenuation;
- Fade slope and fade duration characteristics and statistics;
- Scintillations characteristics;

The approach used can be either, statistical, analytical or with a physical sound basis and also a combination of the previous ones. Each approach has its own advantages and drawbacks.

2.1.1 Rain Attenuation Time Series Synthesizers

2.1.1.1 Stochastic models

In general, the statistical models make some physical assumptions and have their parameters derived from long-term measurements [25]. Most of these are based on the theory proposed by T. Maseng and P. Bakken in [26] — hence the name of Maseng-Bakken based models. The Maseng-Bakken models use two main assumptions about the rain attenuation process:

- It is possible to model the long-term distribution of rain attenuation as a log-normal distribution;
- Rain attenuation can be converted into a first order stationary Markov process by using the non-linear transformation presented in (2.1).

$$X = \frac{ln(A_{rain} - m)}{\sigma} \tag{2.1}$$

Where A_{rain} is the rain attenuation in dB, m is the mean, and σ is the standard deviation of the log-normal distribution of rain attenuation. In addition, the first order stationary Markov processes can be characterized by autocorrelation functions described by the expression (2.2).

$$R_X(\tau) = exp(-\beta|\tau|) \tag{2.2}$$

The rain attenuation time series is generated from a discrete white gaussian noise $n(t)$ that pass through a low-pass filter and is then transformed from a normal to a log-normal distribution in a memoryless non-linear device and calibrated in order to match the rain attenuation statistics of the site of interest. The block diagram of the model is shown in Figure 2.1. This ATSS is defined by the following five parameters::

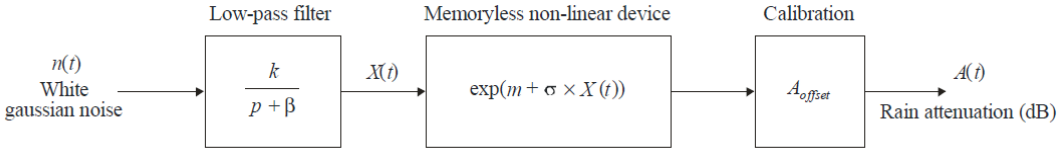

Figure 2.1: *Block diagram of the rain attenuation time series synthesizer [27].*

- m: mean of the log-normal rain attenuation distribution;
- σ: standard deviation of the lognormal distribution;
- p: rain annual probability;
- β: parameter that describes the time dynamics (s^{-1});
- A_{offset}: value that adjusts the time series to match the probability of rain (dB).

The values of m and σ are retrieved from the CCDF of rain attenuation vs. probability of occurrence. These rain attenuation statistics can be obtained either from measured data or (when no measurements are available) by prediction methods. The model proposed in [28] is also based on the Maseng-Bakken assumptions with some difference in the implementation.

Among the statistical models there are also the ones based on statistical conditional probabilities, as the models proposed by Van de Kamp [29], by Fiebig [30] and by Lacoste et al. [31]. These models are based on the assumption that the value of attenuation is going to be equal to a determined value at time $t + \Delta t$, given the information of one or two previous values A_0 at time t, and A_{-1} at time $t - \Delta t$.

2.1.1.2 Models based on meteorological analysis

The models based on the meteorological analysis and forecasting were initially introduced in [32] and [33]. These methods use weather forecast and/or radar data to derive the time series of attenuation and were firstly proposed for SHF and EHF bands. Authors in [32] use the outputs from two models: The Meteorological Office Unified Model (a numerical weather prediction model) and the Meteorological Office radar network (C-band radars).

The work presented in [33] is also based on data provided by two models of numerical weather prediction, the Meteorological Office Unified Model mentioned previously and the system MM5 by the Pennsylvania State University together with the National Centre for Atmospheric Research.

The basic idea behind both models is to convert the atmospheric parameters such as temperature, pressure, humidity, and wind velocity into tropospheric attenuation induced by rain, clouds, oxygen, water vapor, etc.

2.1.1.3 Models based on measurements

More related to this work are the models based on propagation measurements like the ones proposed in [11] and [23].These models use direct measurements collected during a long-lasting campaign at Ka and V bands (1994-2000) in the framework of the ITALSAT satellite propagation experiment. The basic idea underlying these models is that the process of the falling rain (i.e. rain events) is statistically the same worldwide; what changes from site to site is the probability of occurrence of the different classes of rain events (i.e., stratiform and convective). Therefore, a very large database of time series collected in one single site can be adequately used to reproduce statistically the main features of rain attenuation in any site. The models consist in a proper selection of a set of measured time series in order to reproduce the attenuation for the selected site, with possible scaling (not strictly necessary) in terms of frequency, elevation and rain height.

In [34] the authors present an ATSS for joint rain attenuation conditions in multiple sites. The model is based on the same mathematical method used in [35] and uses the same ITALSAT database. The rain events present in the database are divided into 1-hour periods referred to as "epochs" and the rainy and not rainy epochs in each site are described through a correlated binary process. This allows the generation of both rainy and no rainy conditions in multiple sites distributed over a large area while maintaining the spatial and temporal variability of rain. The model showed very good results when tested against experimental time series for fixed satellite scenarios.

2.1.1.4 Models based on the synthesis of rain rate series and its conversion to attenuation

The Synthetic Storm Technique, the method proposed in [36] is based on the synthesis of the rain rate space series and its conversion to attenuation. It starts from the rain rate

time series of rain rate, collected with a rain gauge, and is able to generate rain attenuation time series for any frequency, polarization, elevation (above 20°), and location. Rain rate time series (recorded at one point and averaged over 1-minute time or less) are converted to a rain rate spatial series along a line, by using an estimate of the storm translation speed and with a convolution integral, a synthetic storm is obtained. The predictions of the model are not significantly sensitive to variations in the storm translation speed which value is obtained from measurements at 700 mbar pressure level, usually provided by meteorological services.

The model gives good results when compared with experimental data, however, its main drawback is that it requires experimental rain rate time series for the site where simulations are needed.

2.1.1.5 Rain attenuation time series models for non-geostationary satellites

Unlike the rain attenuation time series synthesizers for geostationary satellites, the ones for non-geostationary (NGEO) satellites (MEO and LEO) have not been yet exhaustively investigated. For these links, besides the spatial variation of rain it is also necessary to consider the variability in time of the link geometry across the rain structure. Figure 2.2 shows a schematic view of a non-geostationary satellite passage. Note that LR_k, the length of the link interested by rain at the k-th time interval does not depend only on the rain height (h_r), on the site height (h_s), and on the elevation angle as it happens in the geostationary links, but also on the height of the satellite orbit (that determines how fast is going to be its passage), and on the variations of both elevation and azimuth.

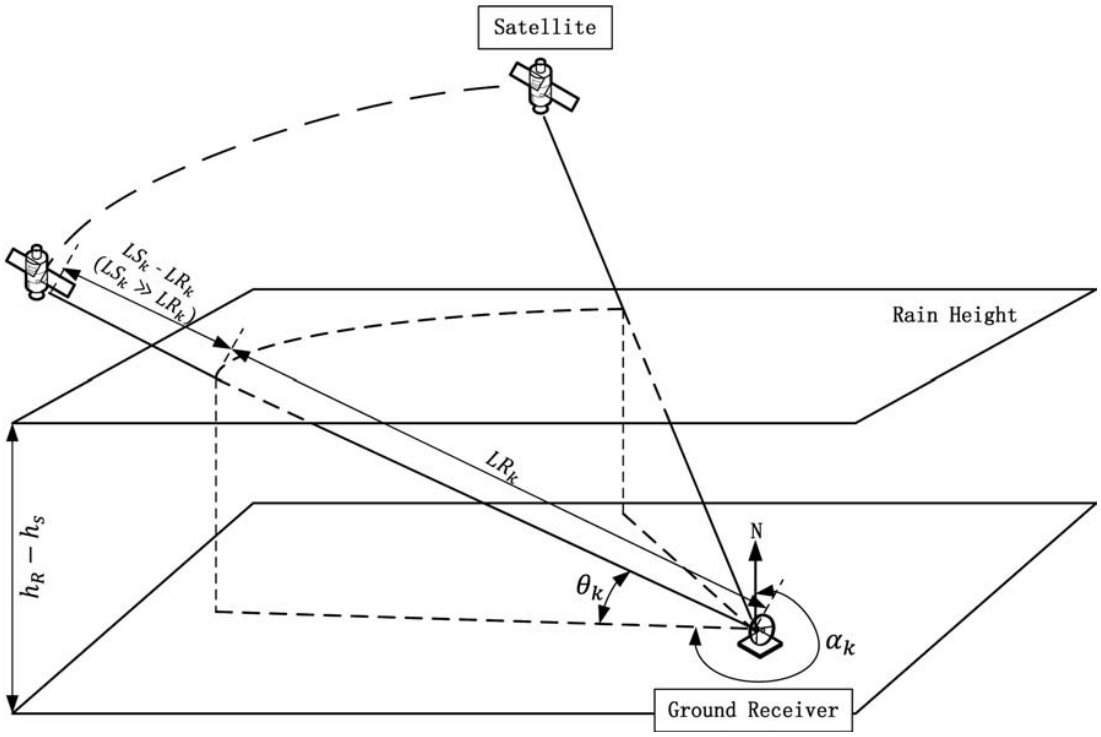

Figure 2.2: *Non-geostationary satellite path across the rain structure [37].*

Indeed, there is a lack of statically significant measurements campaigns for these

satellites. In [38] and [39] an analytical model for the time series generation of rain attenuation is presented. The model is basically an extended version of the Maseng-Bakken one and uses the first-order stochastic differential equations (SDEs) while considering the time dependence with the elevation angle. The main difference with respect to the traditional Maseng-Bakken used for geostationary satellites is the fact that the parameters of the SDEs are time (and, by consequence, elevation) dependent. The model incorporates the PDF of the elevation angle into the long-term statistics of rain attenuation.

2.1.2 Total Attenuation Time Series Synthesizers

2.1.2.1 ITU-R Model

The ITU-R Recommendation P.1853-1 [27] presents a tropospheric attenuation time series synthesizer in which is able to generate rain, clouds, water vapor and oxygen attenuations as well as tropospheric scintillations time series.Figure 2.3 shows the block diagram of the model with the combination of all the attenuation components. The tropospheric attenuation components are obtained as follows:

- The rain attenuation time series are generated with the procedure depicted in Figure 2.1;
- The attenuation due to clouds is obtained by the retrieving of the Integrated Liquid Water Content (ILWC) through a log-normal content and its translation into cloud attenuation with procedure proposed in the ITU-R Recommendation P.840-8 [40];
- Water vapor attenuation in turn is obtained by the retrieving of the Integrated Water Vapour Content (IWVC) through a Weibull distribution and its conversion to attenuation according to the procedure described in the ITU-R Recommendation P.676-11 [41]
- The attenuation due to oxygen is assumed as constant and derived using the Recommendations P.676-11 and P.1510-1 [42];
- Finally, the tropospheric scintillations are assumed as a low-pass filtered white gaussian noise as shown in Figure 2.4.

2.1.2.2 Polimi Model

The author of [11] presents a model able to synthesize total tropospheric attenuation for fixed satellite links. Figure 2.5 shows the block diagram of the synthesizer. The output [$A_{TOT}(t)$] is the total tropospheric attenuation which the link is subjected to at a time t and is a composition of the attenuations due to oxygen [A_{OXY}], water vapor [$A_V(t)$], clouds [$A_L(t)$], and rain [$A_R(t)$]. The synthesis of the rain attenuation time series is based on the principle described in subsection 2.1.1.3 and uses the previously mentioned ITALSAT database. More details on this procedure and on the ITALSAT database are given in Chapter 6.

The synthesis of the water vapor and the liquid water time series in turn follow a procedure analogue the one used to rain. The Integrated Water Vapour Content (IWVC)

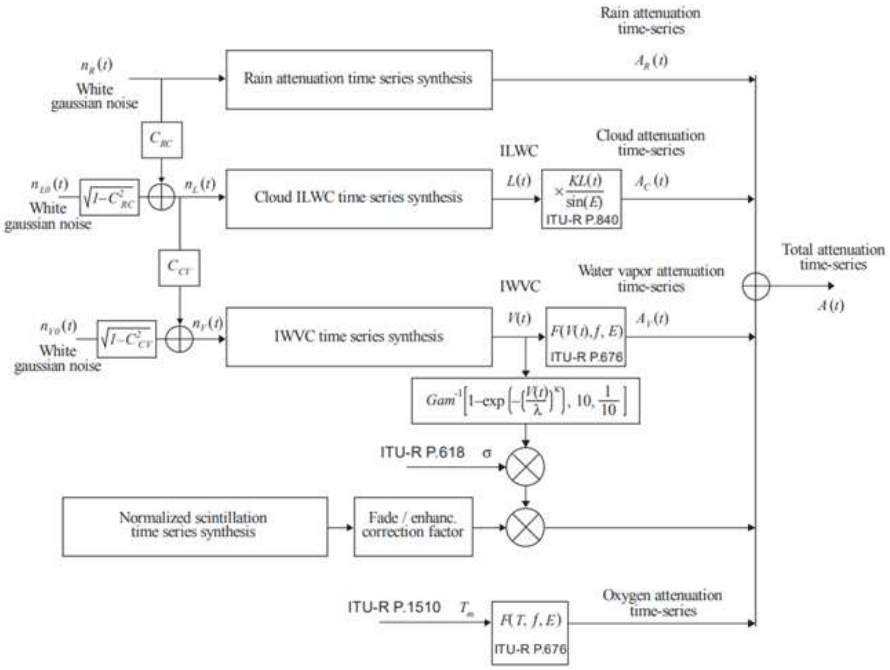

Figure 2.3: *Block diagram of the tropospheric time series synthesizers presented in [27]*
.

and Integrated Liquid Water Content (ILWC) are extracted from the Brightness Temperature measured by a microwave radiometer. The radiometric database consists in seven years (1994 - 2000) of measurements performed by a two channels microwave radiometer at 23.8 and 31.6 GHZ in Spino d'Adda at 37.7° elevation. . This is done by using the retrieval coefficients obtained from the so called RAOBS FERAS database that consists in ten years (1980-1989) of radiosounding measurements of vertical profiles of pressure, temperature, and relative humidity detected at 0 and 12 UTC in non-rainy conditions in 350 sites over the world. The rain events embedded in the ILWC and IWVC time series are detected and removed using three ancillary co-located measured databases, namely: a raingauge 7 years (1994-2000) database collect next to the radiometer in Spino d'Adda, sampled each minute, and with an availability close to 100% of time; a beacon receiver database from the ITALSAT experiment; and the Sky Status Indicator (SSI) that is extracted by the radiometric measurements.

The database is divided in fixed frames of daily time series aiming to maintain the synchronous variation between the quantities of IWVC and ILWC since it was observed an annual trend of the minimum and maximum values of IWVC, the daily average, and the daily maximum value of ILWC. This database is divided in classes (8 for ILWC and 5 for IWVC) according to the maximum value of each quantity. The water vapor and clouds attenuation time series is obtained by a proper selection of daily frames of database that reproduce the CCDFs of ILWC and IWVC for the selected site.

The oxygen attenuation is assumed to be constant and retrieved with the procedures described in the ITU-R recommendations P.1510-1 and and P.676-11.

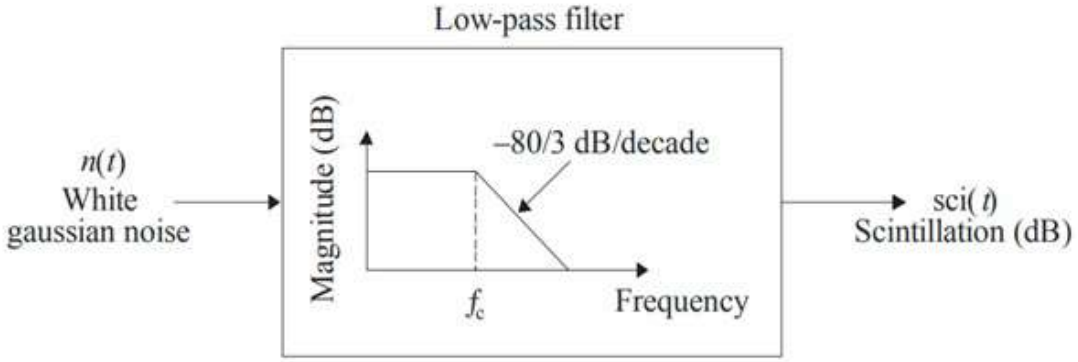

Figure 2.4: *Scintillations time series synthesizer diagram [27]*
.

The block CTA is the implementation of a Cloud Detection Algorithm based on the division of the RAOBS database according to the vertical extent of clouds. This algorithm is able to discriminate rainy from non-rainy clouds in such a way that when a cloud is classified as rainy a rain attenuation event is superposed to the attenuation due to the cloud. More detail on the CTA are given in the Appendix A of [11].

The present work uses as one of the main references the work developed in [11] modify and improve its application to non-geostationary Earth-satellite links.

2.1.3 Final Remarks

In this chapter we provided a brief review of the attenuation time series synthesizers used for propagation purposes present in the literature, describing their advantages and disadvantages and assumptions that support them. Rain ATSS along GEO and LEO (only one) satellite links are presented as well as the ones for GEO satellite that consider also the other components of attenuation (water vapour, clouds and oxygen).

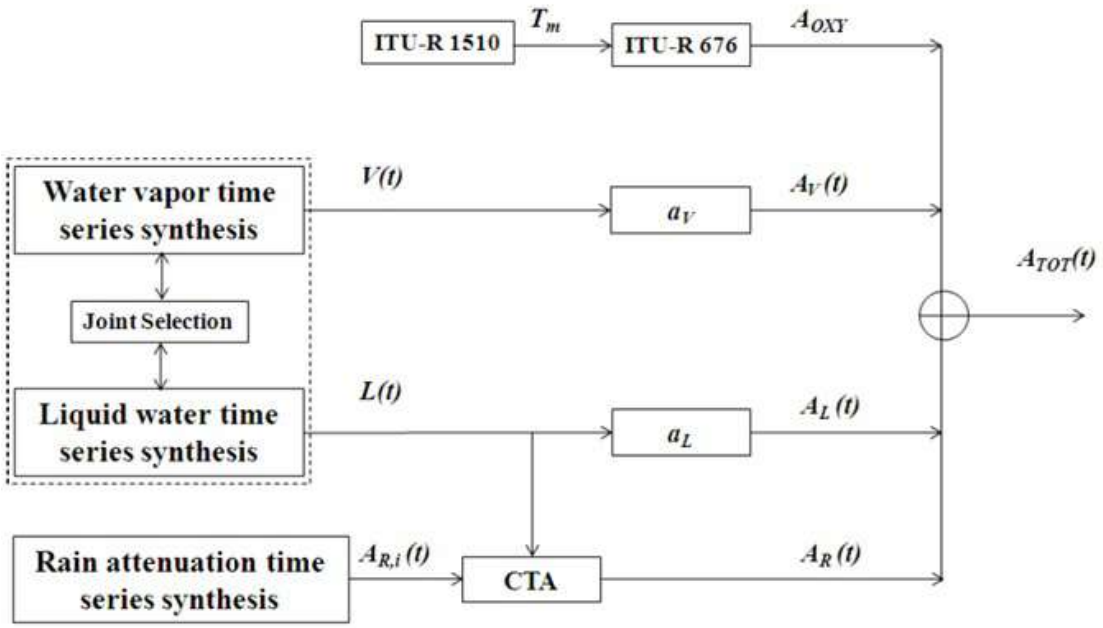

Figure 2.5: *Block diagram of the time series synthesizer presented in [11]*

.

CHAPTER 3

Overview of Our Total Attenuation Time Series Synthesizer for NGEO Satellite Systems

As mentioned in Section 1.2, the use of NGEO satelitte constellations is increasing in the last decades. The variations both in azimuth and elevation angles introduce significant differences on the evaluation and modelling of the propagation aspects when compared with the GEO satellite systems in which these angles are fixed.

The philosophical approach at the basis of the total attenuation time series synthesizer for non-geostationary satellites we are going to present in this PhD work is the development of a model that maintains as much as possible a physical sound basis.

This chapter outlines our proposal model, whose various steps are then detailed and discussed in the following chapters from 5 to 9.

3.1 Rain Attenuation Time Series Generator

Figure 3.1 shows the block diagram where the complete model is depicted. The basic inputs to the model are:

- the orbit of the satellite (that can be obtained either by a commercial software like STK, Two-line Element set [TLE] data, or even analytically);
- the ground station parameters (site height and rain height);
- the CCDF of rain attenuation of the site (measured or predicted) at the minimum elevation angle considered in the satellite orbit: The reason is that it is more accurate to obtain all the data of the synthesizer by a scaling up from the reference curve.

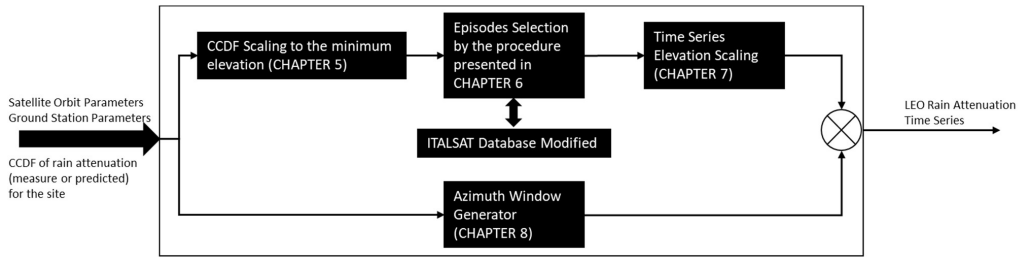

Figure 3.1: *Block diagram of the rain attenuation time series generator for NGEO satellite systems.*
.

If, as expected, the CCDF of $A_{dB}(\theta_{min})$ is not available, the most accurate one of the site (measured from GEO or predicted from a model at a GEO elevation) will be scaled down to θ_{min} with the procedure presented in Chapter 5.

The scaled CCDF is the input of the block that gives in the output a set of time series of rain attenuation following the procedure described in Chapter 6. These time series are then scaled in terms of elevation following the steps also detailed in Chapter 7 in such a way to maintain the full temporal correlation with the generating one.

As for the variations of the attenuation in azimuth, from the simulations performed we got the confirmation of our preliminary assumption: for modelling purposes they are independent from the elevation variations and as such they are treated separately. As a consequence, each output rain attenuation time series consists in the one obtained in the previous step (elevation variation) combined with the binary output of the block Azimuth Window Generator that implements the procedure described in Chapter 8.

3.2 Water Vapor and Clouds Attenuation Time Series

Chapter 9 is dedicated to the analysis of the water vapor and clouds attenuation time series. It will be shown that the scaling of water vapor attenuation in terms of elevation can be done by using a simple geometric relation. Moreover, due to the more uniform distribution of water vapor with respect to rain or clouds, it is not necessary to apply to it the concept of an azimuth window. The water vapor attenuation time series generator makes reference to the one proposed in [11] with the addition of the elevation scaling mechanism, as shown in Figure 3.2. For the clouds attenuation time series, in turn,

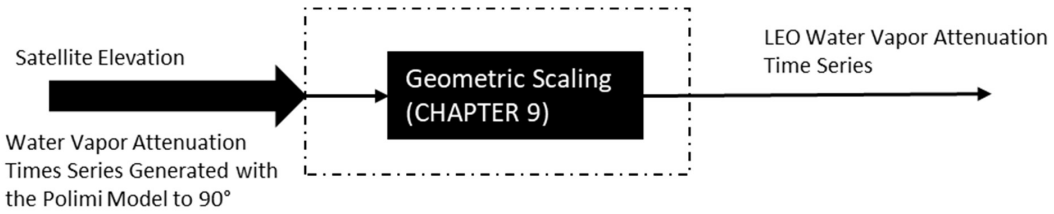

Figure 3.2: *Water vapor scaling block diagram.*

we propose in Chapter 9 a method for scaling up them from the minimum elevation, analogously to the one developed in Chapter 7 for rain. A possible development of an azimuth window generator for clouds is indicated as one of the future works although, on a statistical basis, it does not seem to be strictly necessary.

3.3 Oxygen Attenuation Time Series

The oxygen attenuation is simply scaled from the vertical to the desired elevation angle with the cosecant relation and its value is obtained by Recommendations P.676-11 and P.1510-1. We assume that oxygen distribution is uniform in azimuth.

3.4 Total Attenuation Time Series Synthesis

The total attenuation time series synthesis is obtained by properly summing up the contributions detailed above. The summing procedure that must maintain a relationship among the different contributions follows the one proposed in [11] and illustrated in Figure 2.5, i.e. which makes the use of the block CTA (Cloud Type Algorithm).

3.5 NGEO orbit generation

The generation of the NGEO orbits for purposes of simulations (Chapter 10) used in this work was done following the procedure described in [43], which consists in retrieve the elevation and azimuth from the orbital parameters applying the Simplified General Perturbation model SGP4 to propagate the satellite position and velocity. More details on the satellite scenario to which the orbits were generated are given are given in Chapter 10.

3.6 Final Remarks

This chapter presented a summary of the models that will be addressed in the next chapters of this thesis. We have here described the procedure used to convert separately the various components of tropospheric attenuation obtained from direct measurements at a fixed elevation to any requested elevation and then how they must be summed up into a total attenuation time series for a NGEO satellite link.

It is important to clarify that the procedure described is for generating the average process. For the instantaneous one we introduce the use of some variations that will be introduced in chapter 10.

CHAPTER 4

Reference Rain Attenuation Database

In this chapter we introduce the MultiEXCELL rain attenuation database used in this work. This database was obtained by simulations carried out on the rain rate maps provided by the MultiEXCELL model. These simulations were fundamental for the development of the models during this PhD. research.

4.1 MultiEXCELL Model

The propagation-oriented MultiEXCELL (Multi EXponential CELL) rain field model — described in [44], and extensively validated for several propagation-oriented applications ([45], [46], and [47] — generates realistic rain fields composed by an ensemble of synthetic aggregates each one containing exponentially shaped rain cells after the EXCELL model [48].

The aim of MultiEXCELL model is to join the advantages of two previous models: EXCELL [48] and HYCELL [49]with the aim to preserve (and enhance) the simple and manageable mathematical expressions of rain cells proposed by EXCELL (a model particularly oriented to propagation applications) while overcoming its major drawback to be inherently a small-scale model. EXCELL is, in fact, a model that generates isolated cells defined as "the continuous area inside which rain rate is higher than a given threshold" [50], set to 5 mm/h, with size limited to 20 km circa. They have the simple analytical exponential shaped profile described in (4.1).

$$R(\rho) = R_M e^{-(\frac{\rho}{\rho_0})^{\frac{2}{k}}} \tag{4.1}$$

where R is the rain rate in mm/h, ρ is the distance from the cell center, R_M is the maximum rain rate of the cell and ρ_0 is the equivalent radius for which $\rho_0 = R_M/e$. Finally, k is the shape factor and — for an exponential cell — its value is 2. Different

values of k, as e. g. k=1 or k=3, give Gaussian and hyper-exponential cell profiles respectively. Figure 4.1 depicts the shape of a typical exponential cell.

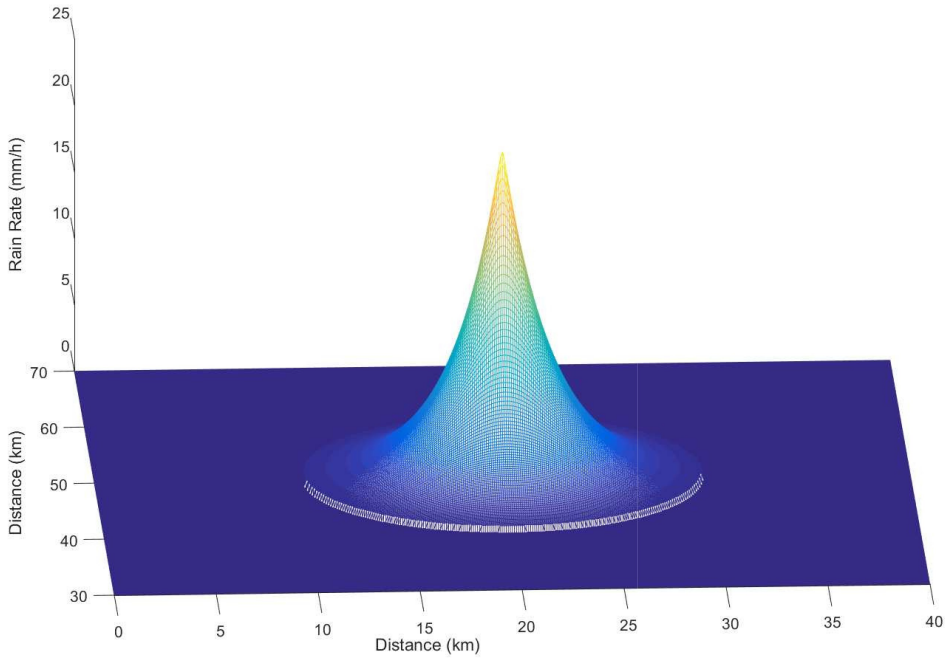

Figure 4.1: *Example of exponential rain cell.*

However, MultiEXCELL uses a revised parametrization based on the information obtained by radar maps NPC (*Nastri Pioggia Cartesianizzata*) database. This database is the result of a long-term measurement campaign from 1988 to 1992 that collected several rain events in radar maps with a S-band Doppler weather radar located at Spino D'Adda (latitude 45.4° N, longitude 9.5° E, altitude 84 m a.m.s.l), a few kilometers East of Milan, Italy [44].

In order to allow mid/large-scale applications, particularly important for simulations of complex TLC systems, MultiEXCELL generates synthetic rain fields based on aggregates of exponential rain cells. It considers that rain cells tend to aggregate into larger rain structures as shown in Figure 4.2 where we can see that the rain structure delimited by the ellipse on the right has inside two rain cells close one to the other (red circles): i.e. they form an aggregate. According to [49] this aggregation procedure tends to be more remarkable as the rain cell intensity increases. In the MultiEXCELL model, these aggregates are defined as the area with rain rate exceeding a specified level (1 mm/h) and having inside two or more peaks greater than 5 mm/h. More than one aggregate can be present in a rain map. Using a procedure based on a double aggregative process, MultiEXCELL is able to synthesize sets of rain fields maintaining the site specific 1-minute integrated rainfall statistics as well as the rainfall spatial distribution. The double aggregative process consists in (1) clustering the cells into aggregates and (2) combine the aggregates in the rain map by reproducing the local fractional rainy area distribution, a parameter derived from coarse meteorological information extracted from ECMWF (European Centre for Medium-range Weather Forecast) ERA-40

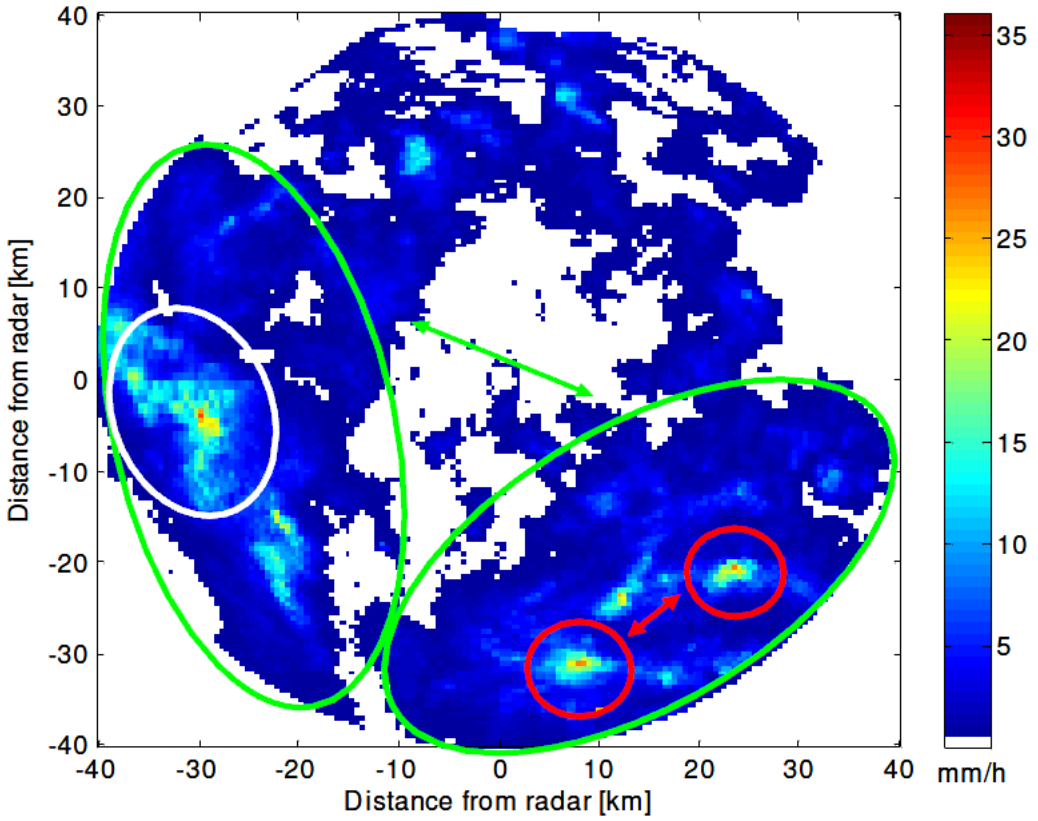

Figure 4.2: *Typical rain field that illustrates the aggregative process observed by a radar located at Spino d'Adda.*

database. MultiEXCELL assumes also a constant vertical rain profile from the ground up to the 0°C isotherm height.

This complex description of the rain field is particularly important for the evaluation of non-geostationary links performance, in which the path length across rain becomes longer and longer with the decreasing of the elevation angle. Thus, the probability that more than one cell (or aggregate) simultaneously interacts with the link increases strongly.

Using MultiEXCELL, 578 synthetic rain maps were generated, whose ensemble reproduces the long-term local rain intensity statistics (the only input to the model) and maintain the spatial distribution of rain at Spino D'Adda. Figure 4.3 shows a sample rain map provided by the model.

In this work, the reference site is Spino D'Adda, Italy . The map dimension is 230 km x 230 km and the spatial resolution is 1 km x 1 km. Maps generated to another site — Miami, USA — were used in order to have some validation for the models. For Miami, we obtained 570 maps with the same dimensions and the same space resolution of the ones generated for Spino D'Adda. The input of the model, in this case, is the long-term rain rate CCDF of Miami.

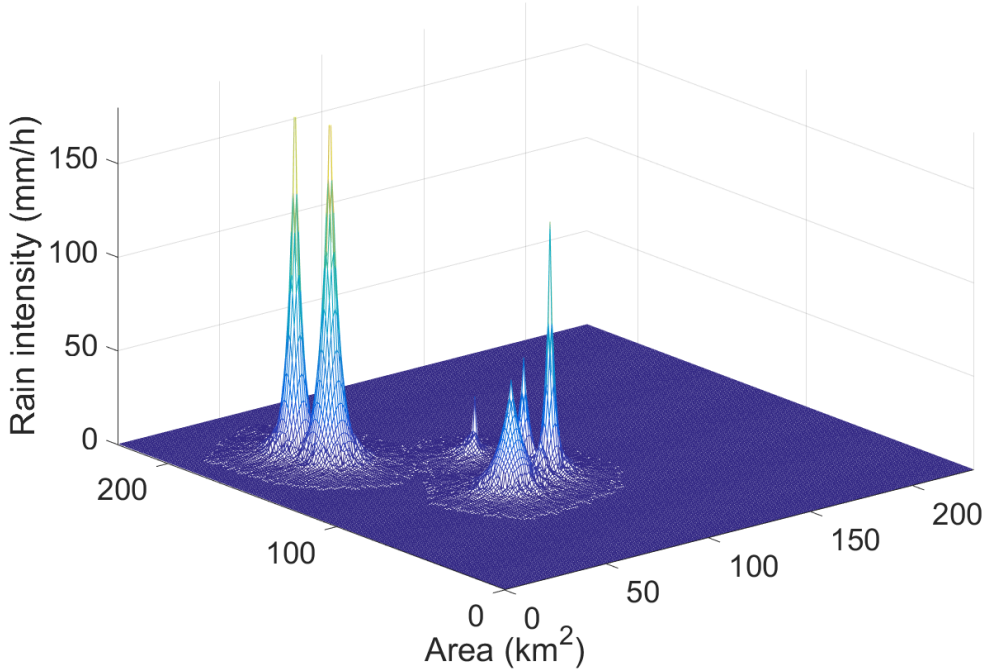

Figure 4.3: *Sample of the rain maps generated by the MultiEXCELL model.*

4.2 Retrieval of Rain Attenuation from the MultiEXCELL Maps

Starting from the rain rate maps, the corresponding specific attenuation maps can be easily obtained by applying the well known power law presented in (4.2).

$$\gamma(x,y) = k[R(x,y)]^{\alpha} \tag{4.2}$$

where $\gamma(x,y)$ is the specific attenuation at each pixel of the map in dB/km; $R(x,y)$ is the rain rate in mm/h of the pixel, and the parameters k and α are dependent on frequency, polarization and elevation angle, and are also function of the Drop Size Distribution (DSD), as well as of the refractivity index of water which, in turn, depends on its temperature. These parameters can be evaluated with the procedure presented in ITU-R recommendation P.838-3 [51]. The values of k and α are retrieved by the equations (4.3) and (4.4).

$$k = \frac{k_H + k_V + [k_H - k_V]cos^2(\theta)cos(2\tau)}{2} \tag{4.3}$$

$$\alpha = \frac{k_H\alpha_H + k_V\alpha_V + [k_H\alpha_H - k_V\alpha_V]cos^2(\theta)cos(2\tau)}{2k} \tag{4.4}$$

Where the subscripts H and V stand for horizontal and vertical polarizations respectively, θ is the elevation angle and τ is the polarization angle. For circular polarization, τ must be set to 45°. The recommendation P.838-3 provides a table of the values for k_H, k_V, α_H, and α_V at different frequencies.

Once obtained the specific attenuation, the amount of rain attenuation in dB along the slant path can be evaluated by integration as in (4.5).

$$A(dB) = \int_0^L \gamma dL \tag{4.5}$$

where L_s is the effective slant-path length across the rain in km that depends on the elevation angle and the rain height — the difference between the mean annual 0°C isotherm height above mean sea level and the height of the site — derived from the procedure proposed in ITU-R Recommendation P.618-13 [18]. Figure 4.4 illustrates the position of these parameters in a schematic Earth-satellite links.

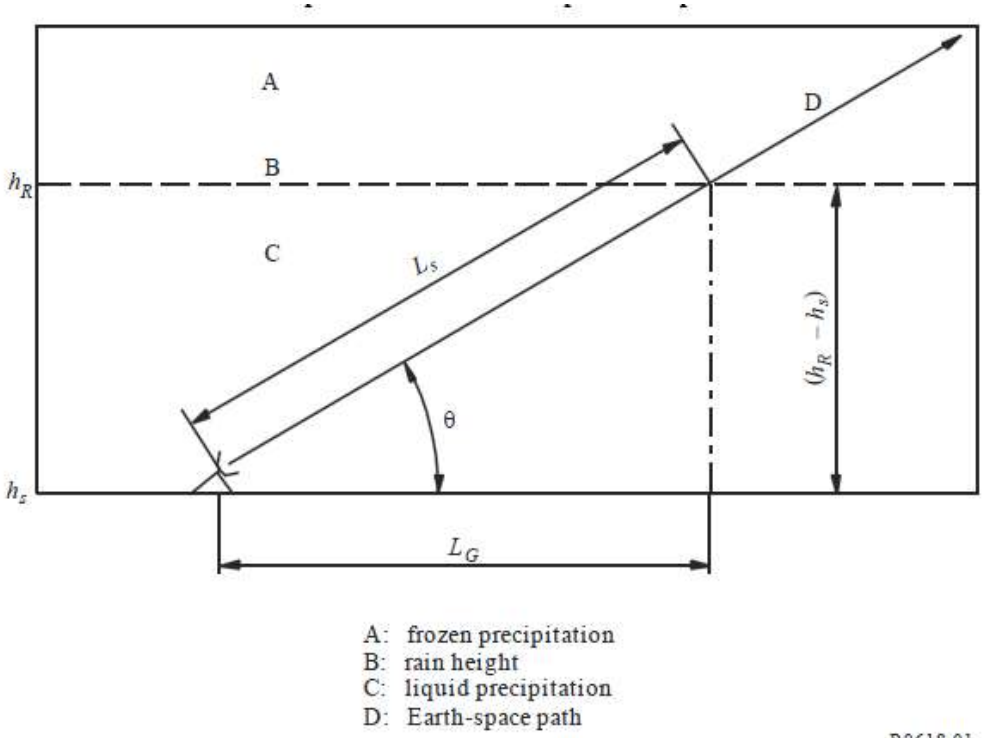

Figure 4.4: *Schematic diagram of an earth space link [18]*

As the simulations we were interested in are for elevations greater or equal to 5°, the evaluation of L_s does not considers the Earth curvature and can be expressed as in (4.6).

$$L_S = \frac{H_R - H_S}{sin(\theta)} \tag{4.6}$$

The simulations were performed by evaluating the attenuation with defined link parameters (elevation angle, azimuth, frequency and rain height) and with the ground station set in each pixel of each rain map. In this way we were able to obtain an amount of data sufficient for the generation of long-term statistics. In order to validate the overall procedure, results from simulations at 39.6 GHz and an elevation angle of 37.7° were compared with long term measured attenuation collected in the framework of the ITALSAT propagation experiment at Spino d'Adda as it is depicted in Figure 4.5. It can be seen that the results show a very good agreement with the reference, even at

low probability levels that are the most critical to obtain because of the need of a large amount of attenuation data.

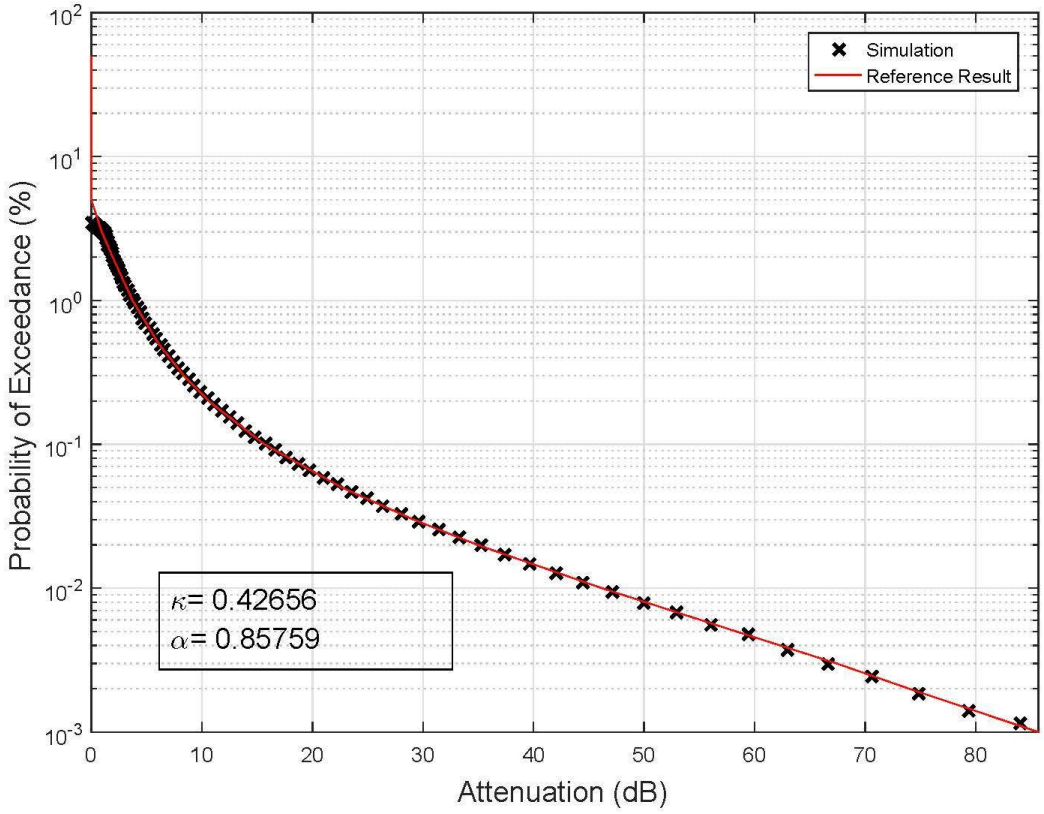

Figure 4.5: *Annual exceedance probability obtained in relation to a reference result (39.6 GHz, circular polarization).*

Especially at very low elevations, depending on the position of the ground station, the horizontal projection of L_s exceeds the boundary of the map: to maintain the same number of data whichever the elevation considered it was necessary to extend the rain field, which is achieved by placing alongside the first map a second one with approximately the same rain coverage (which is acceptable when considering no significant changes in the local orography). The solution adopted consists in randomly pick up, within the map database, one with a similar rain coverage (with 20% of tolerance). It is important to clarify that the ground station positions are confined to the pixels of the first map. The second one serves only as an extension of the map when the integration procedure arrives to the border.

All the simulations performed assume that the rain structures do not change in time during the passage of a LEO satellite, which indeed is not strictly the case [52]. Nonetheless, as the LEO passage lasts a few minutes and since the main objective of these simulations is to extract parameters that impacts the long-term statistics of rain attenuation, it turns out that it is possible to use this static approach for sake of modelling convenience while maintaining a good level of accuracy. In case of MEO satellites links this assumption is more critical since the passages are longer.

4.3 Final Remarks

In this chapter we described the database used for the majority of the modelling procedures proposed in this work. We summarized the rationality behind the MultiEXCELL rain field model and described the procedure to retrieve the rain attenuation from the rain maps provided by MultiEXCELL.

CHAPTER 5

Elevation Scaling of Rain Attenuation Statistics

Due to the lack of long-term measurements of rain attenuation on a large range of link elevations at the same site, the use of a scaling technique for the $A(\theta)$ CCDFs becomes essential. In this chapter we present a method to scale the CCDF of rain attenuation starting from the CCDF along the zenithal path. The rationale assumption is that the attenuation CCDF at 90° elevation is directly related to the local rain probability $P(R)$ being the path length constant and equal to the rain height.

The implementation of the procedure described in this chapter results in the block "CCDF Scaling to the minimum elevation" in Figure 3.1.

5.1 Modelling the scaling factor

To model the scaling factor, it was first necessary to model the variation of $P_0(\theta)$, the probability to have rain attenuation along the link, which increases with the decrease of path elevation.

The scaling factor for P_0 is $SF_0(\theta)$ is defined in (5.1).

$$SF_0(\theta) = \frac{P_0(90°)}{P_0(\theta)} \tag{5.1}$$

where $P_0(90°)$ and $P_0(\theta)$ are the long-term probability to have rain attenuation along the vertical path, and along a slant path (θ ranging from 1° to 89°), respectively. A satisfactory model for $SF_0(\theta)$ is given by the following simple formula in (5.2).

$$SF_0(\theta) = 1.741\theta^{-0.6015} + 0.8931 \tag{5.2}$$

with θ is expressed in degrees. Figure 5.1 shows the values of $SF_0(\theta)$ obtained from simulations and from the power law model in (5.2), which indicates a very good fitting accuracy.

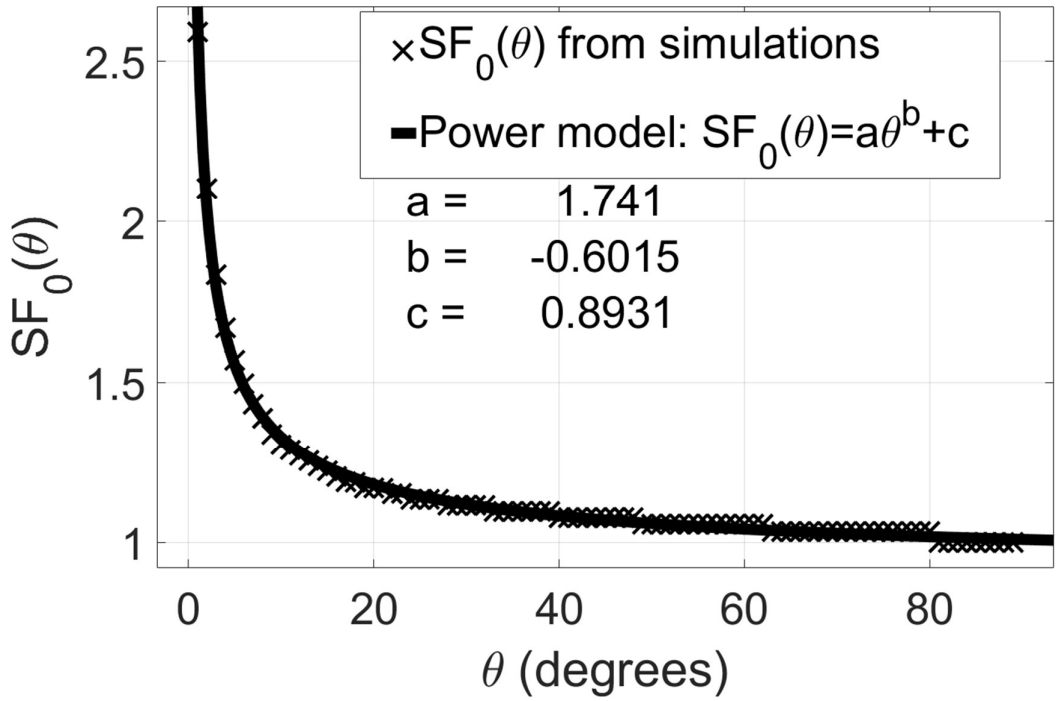

Figure 5.1: *Scaling factor for the probability to have rain attenuation along the link.*

For all the other points of the CCDFs the scaling factor should be also probability dependent, $SF(P, \theta)$, which is defined as the ratio between the attenuation exceeded at elevation θ and the one predicted by the simple cosecant law from the zenith path. It was calculated by evaluating (5.3) at the following probability levels: [1, 0.5, 0.4, 0.3, 0.2, 0.1, 0.05, 0.04, 0.03, 0.02, 0.01] % for each elevation θ.

$$SF(p, \theta) = \frac{A_{dB}(p, \theta)}{csc(\theta) A_{dB}(p, 90^\circ)} \tag{5.3}$$

$SF(P, \theta)$ was then modelled by using the polynomial relationships in (5.4).

$$SF(p, \theta) = \alpha_1(\theta)p^3 + \alpha_2(\theta)p^2 + \alpha_3(\theta)p + \alpha_4 \tag{5.4}$$

The coefficients α_i are dependent on the elevation angle and are calculated using equantions (5.5a) and (5.5b) and Table 5.1.

$$\alpha_i(\theta) = a_i e^{b_i \theta} + c_i e^{d_i \theta} \qquad \text{if } i < 4 \tag{5.5a}$$

$$\alpha_i(\theta) = \frac{0.9551\theta^2 - 0.9108\theta + 3.213}{\theta^2 - 1.998 + 5.921} \qquad \text{if } i = 4 \tag{5.5b}$$

Table 5.1: *Coefficients for the expression in*

i	a	c	d	e
1	0.09608	-0.2675	-0.07699	-0.0319
2	-0.4054	-0.03019	0.5544	-0.1964
3	-0.4024	-0.02615	0.9201	-0.1177

5.2 Results

To evaluate scaling model accuracy, we used the figure of merit proposed in ITU-R Recommendation P.311-15 [53] given in (5.6) and its RMS value in (5.7).

$$\epsilon(p) = ln\left(\frac{A_{sc}(p)}{A_{si}(p)}\right)\left(\frac{A_{si}(p)}{10}\right)^{0.2} \qquad \text{for } A_{si} \leq 10dB \tag{5.6a}$$

$$\epsilon(p) = ln\left(\frac{A_{sc}(p)}{A_{si}(p)}\right) \qquad \text{for } A_{si} > 10dB \tag{5.6b}$$

$$RMS(\epsilon) = (\mu_\epsilon^2 + \sigma_\epsilon^2)^0.5 \tag{5.7}$$

A_{sc} is the scaled value and A_{si} is the value of the reference simulated curves; p is the probability level; μ_ϵ and σ_ϵ are respectively the mean and the standard deviation of ϵ. The result obtained from the model is also compared with the one obtained from the customary cosecant scaling.

Figure 5.2 shows the results of the scaling applied to a low elevation (5°) at Spino d'Adda, Italy at a 39.6 GHz frequency. The CCDF obtained with the model is compared with the one obtained by MultiEXCELL. As it is possible to see, as expected, the model shows a significant improvement in comparison with the cosecant law, especially for the lower probabilities. Figure 5.3 shows the results (mean and RMS) of the figure of merit for a large range of elevation angles (from 5° to 80° with 1° step). It is worth noticing that the cosecant law is satisfactorily applicable down to 20-25 degrees; after the discrepancy becomes definitely significant.

The method was also applied to another frequency. Figure 5.4 shows the result at 18.7 GHz for the same location (Spino d'Adda) and elevation equal to 5° and Figure 5.5 presents as above the mean (a) and RMS (b) of the figure of merit from 5° to 80°. Again, the model shows an improvement in relation to customary cosecant scaling at all probability range (RMS (ϵ)=0.1 against RMS (ϵ)=0.38 for the cosecant scaling).

We also applied the model to another site i.e. Miami-USA simulated through the MultiEXCELL maps generated according to the input P(R) of the site. Miami was selected because of the very different climate (tropical) with respect to Spino d'Adda (temperate, continental). The results are shown in Figure 5.6 and Figure 5.7 . As in Miami the rain tends to be very convective, it leads to very high levels of attenuation. Because of that, the simulations for this site were carried out only until 10° elevation. In this case, indeed, the attenuation level for a probability of $10^{-1}\%$ exceeds 150 dB. Due to this fact we show the simulations done and evaluate the figure of merit only until the $10^{-1}\%$ level. As it is possible to notice, the improvement with respect to the cosecant scaling is lower but, nonetheless, significant. This can be explained by the

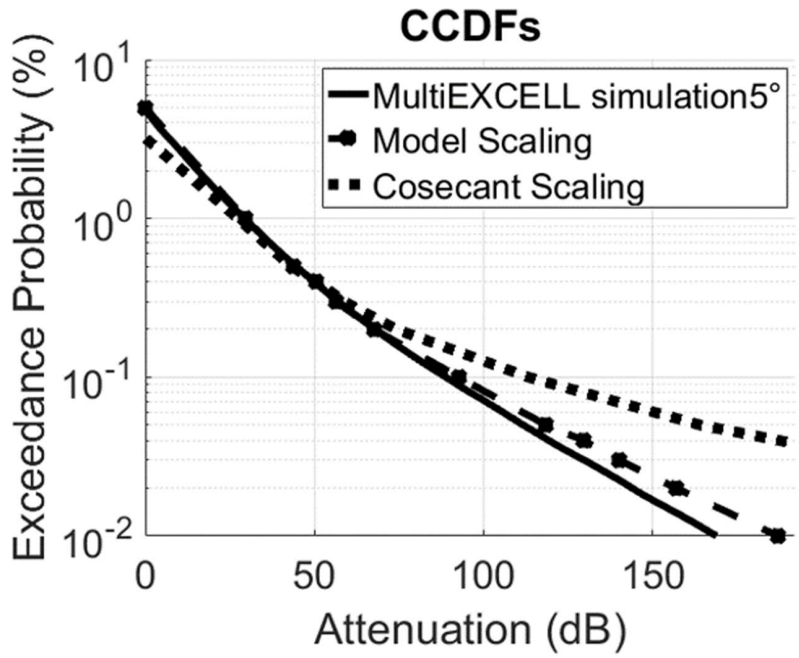

(a) *CCDFs*

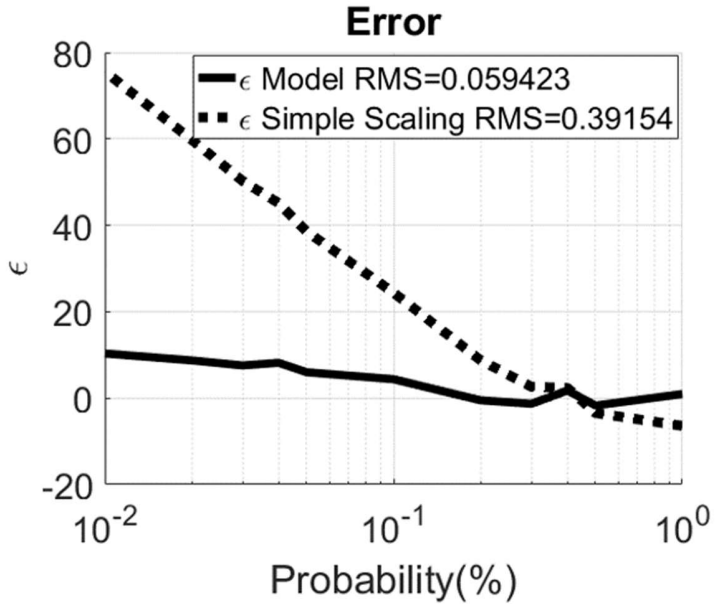

(b) *figure of merit*

Figure 5.2: *Scaling factor applied to 5° (Spino d'Adda, 39.6 GHz, circular polarization).*

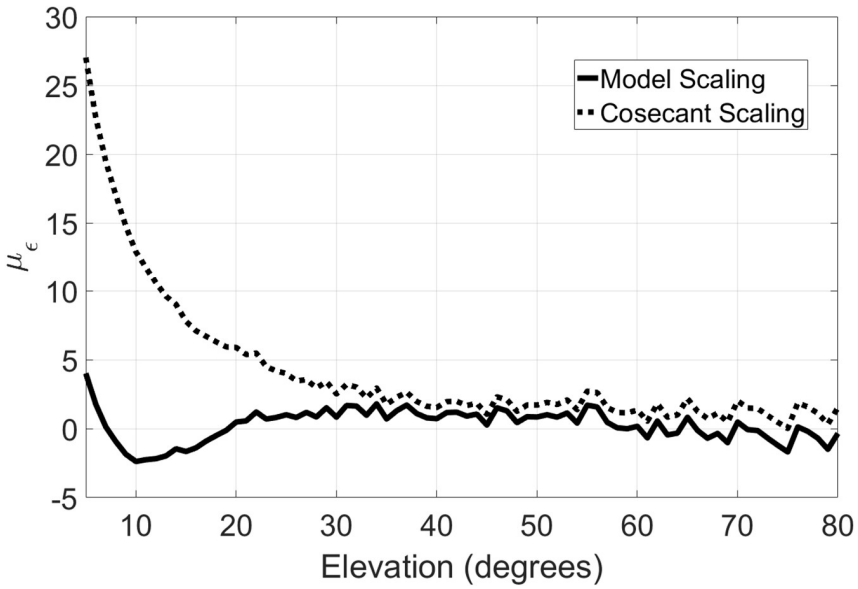

(a) *Mean of* ϵ

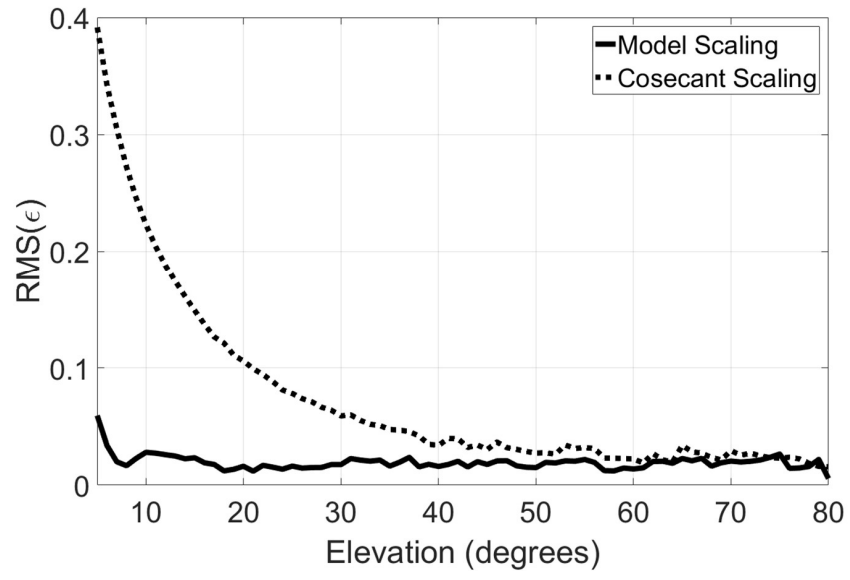

(b) *RMS of* ϵ

Figure 5.3: *Figure of merit for a large range of elevations (Spino d'Adda, 39.6 GHz, circular polarization).*

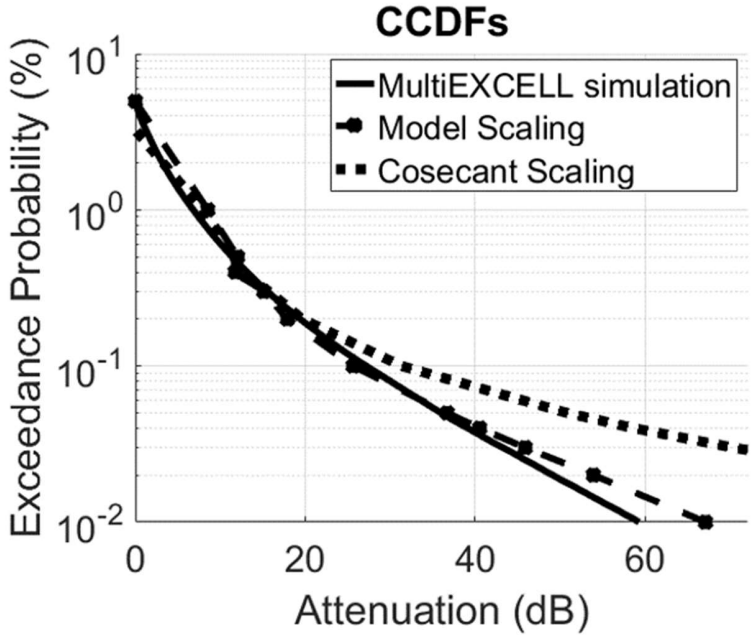

(a) *CCDFs*

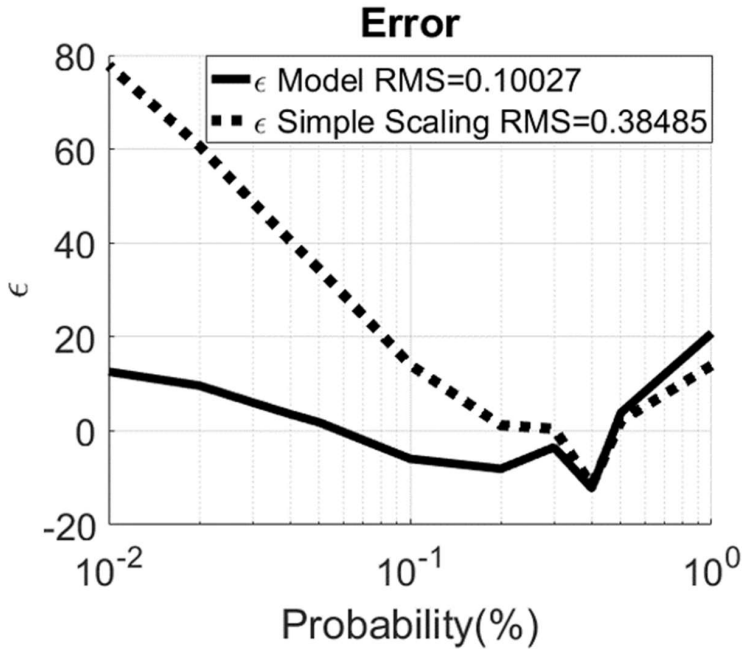

(b) *Figure of merit*

Figure 5.4: *Scaling factor applied to 5° (Spino d'Adda, 18.7 GHz, circular polarization).*

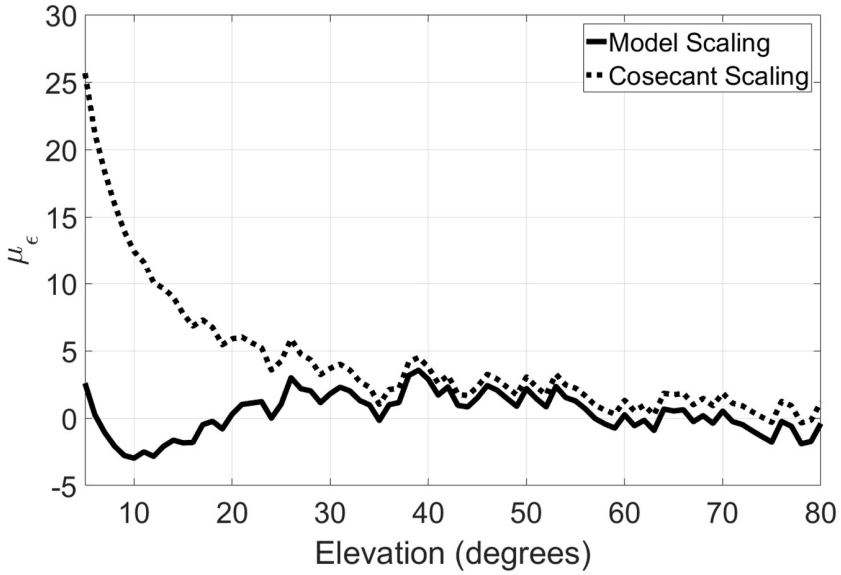

(a) *Mean of* ϵ

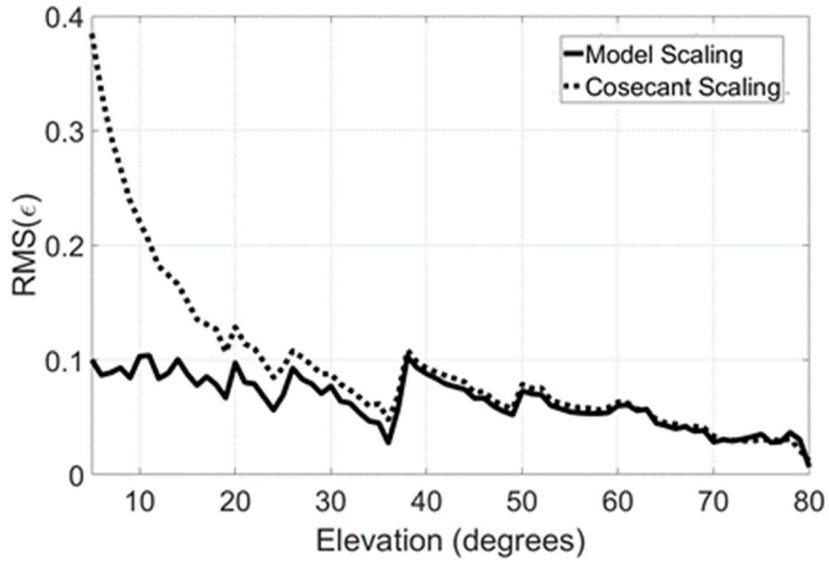

(b) *RMS of* ϵ

Figure 5.5: *Figure of merit for a large range of elevations (Spino d'Adda, 18.7 GHz, circular polarization).*

fact that the rain profile of Miami (very convective) is diametrically opposed to that of Spino d'Adda (more stratiform).

It has to be stressed that the performance results in Spino d'Adda and in Miami cannot be directly compared because of the different probability range considered, after around $10^{-1}\%$ all the predicted curves tend to definitely overestimate the MultiEXCELL ones.

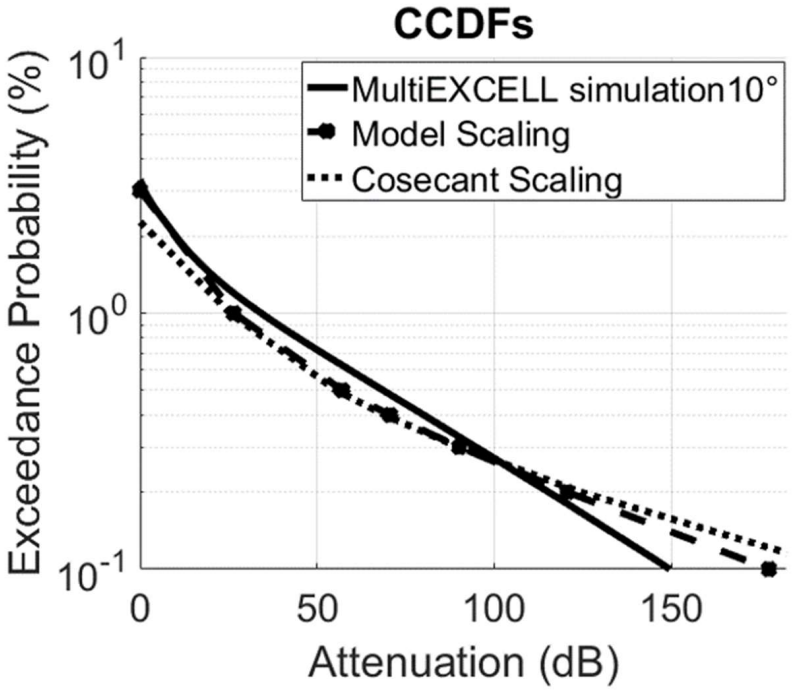

(a) *CCDFs*

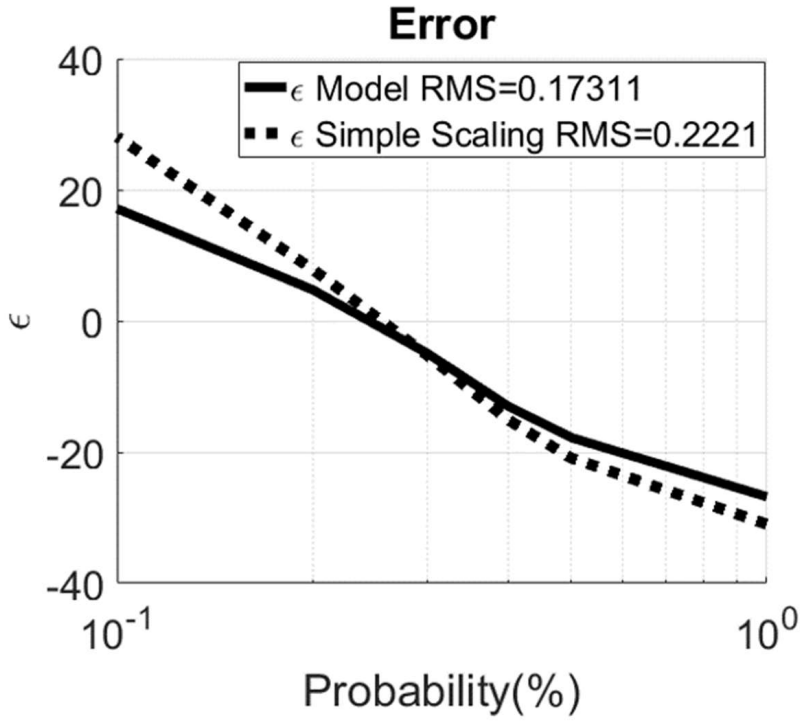

(b) *Figure of merit*

Figure 5.6: *Scaling factor applied to 10° (Miami, 39.6 GHz, circular polarization).*

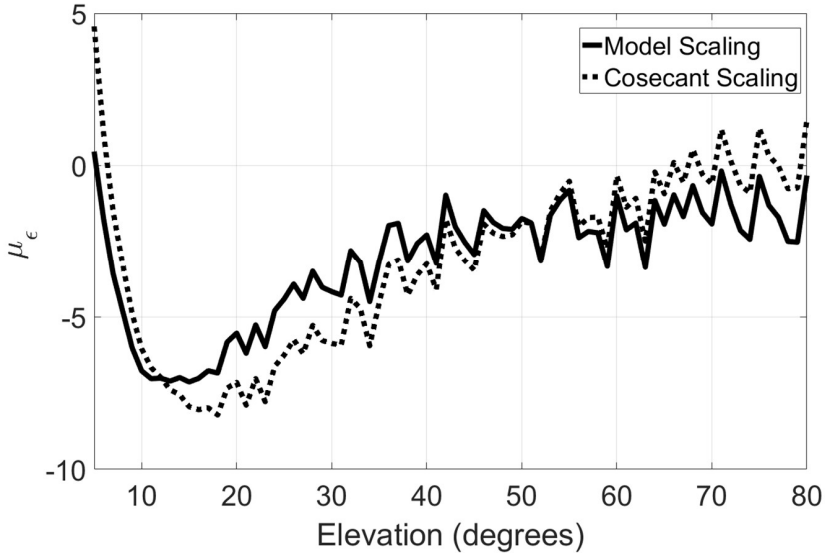

(a) *Mean of* ϵ

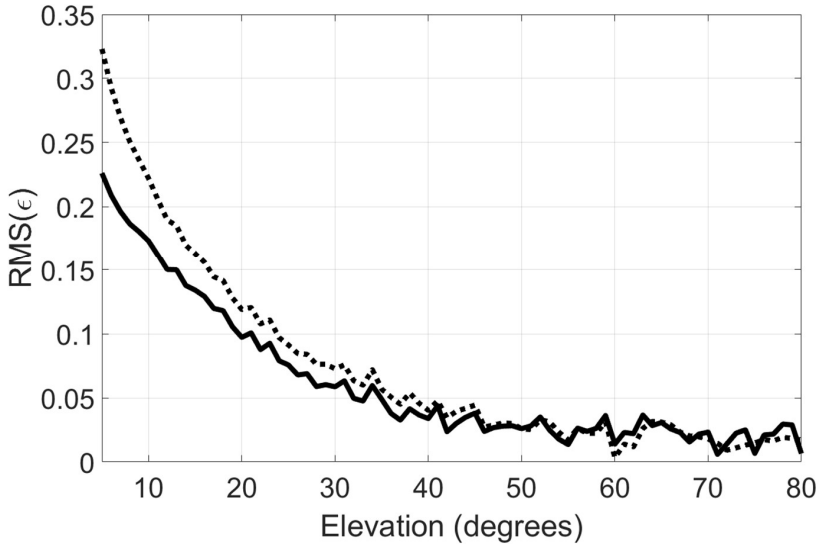

(b) *RMS of* ϵ

Figure 5.7: *Figure of merit for a large range of elevations (Miami, 39.6 GHz, circular polarization).*

5.3 Final Remarks

In this chapter we have presented a model to scale the CCDF of the rain attenuation according to the link elevation θ covering the full range of values ($5^\circ \leq \theta \leq 90^\circ$). The proposed scaling methodology, shows a definite improvement in the prediction accuracy for elevation angles lower than 20 degrees when compared to the simple customary cosecant scaling law. We have also showed some positive preliminary tests on the applicability of the model to different frequencies and sites that allows to believe to its applicability worldwide.

CHAPTER 6

Extension of The ITALSAT Rain Attenuation Database

In Chapter 3 we have anticipated our plan to use directly measured time series of rain attenuation (ITALSAT database) as input to the TSS. In this respect, we do have to consider that decreasing the angles the length of the radio link subjected to rain rapidly increases and, as a consequence, also the path attenuation increases severely and, as evidenced before, the simple geometric scaling can no longer be applicable. In fact, for long path length, it is likely that the radiowave crosses more than one rain structure at a time.

This chapter presents a model able to generate time series of rain attenuation appropriate also for low elevation angles. The procedure starts from the rain attenuation episodes obtained from the ITALSAT database and generates time series that are able to reproduce also the CCDFs of rain attenuation down to 5°. With this procedure we have detailed the inner structure of the blocks "Episode selection" and "ITALSAT database modified" in Figure 3.1.

6.1 ITALSAT database description

The database we are referring to, which forms the input of the time series synthesizers presented in [35], [11], and [34], is populated by post processed results from the ITALSAT propagation experiment and includes measurements of rain attenuation collected at Spino d'Adda, Italy (45.4° N, 9.5° E). The satellite ITALSAT F1 was launched on January 1991 and its mission ended on January 2001. The experiment, carried out over a seven years period (1994-2000), collected measurements at three beacons at 18.7 (vertical polarization), 39.6 (circular polarization) and 49.5 GHz (vertical/horizontal polarization) at an elevation of 37.7° with an offset antenna of 3.5 m diameter [54].

The sampling rate of the beacon signal was 1 second.

The main objective of the experiment was to asses and model the radio channel and produce statistical results for the design of satellite communication systems up to 50 GHz [23].

ITALSAT was a three axes stabilized geostationary satellite in orbit at 13° E latitude.

The raw data base is constituted by several rain attenuation episodes. Each episode is defined as a sequence of consecutive samples with rain attenuation greater than zero. The original episodes contain not only rain attenuation but also the other attenuation components (clouds, water vapor, scintillations and oxygen) that were removed with an appropriate processing. More details about this procedure can be found in [35] and [23]. The ITALSAT database is a property of the *Agenzia Spaziale Italiana* (ASI).

Figure 6.1 shows the histograms of the peak attenuation and duration for the rain attenuation episodes of the database obtained from the 39.6 GHz beacon.

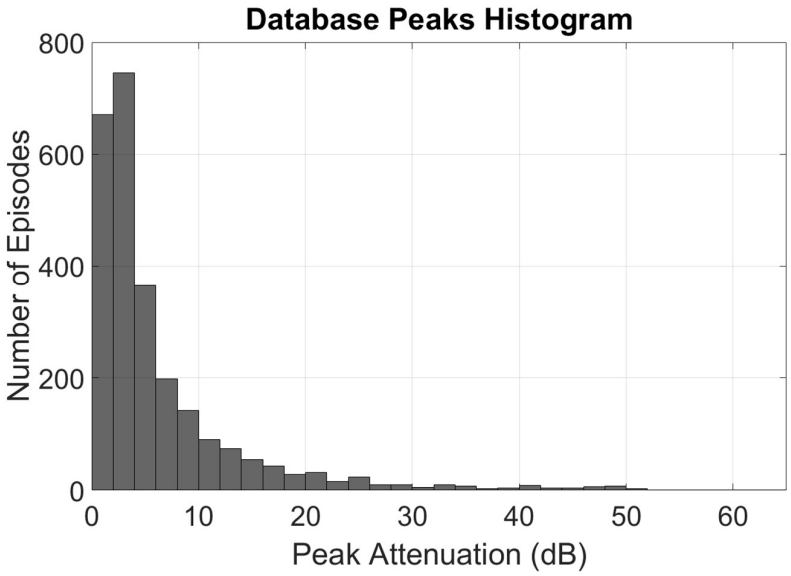

(a) *Peak attenuation*

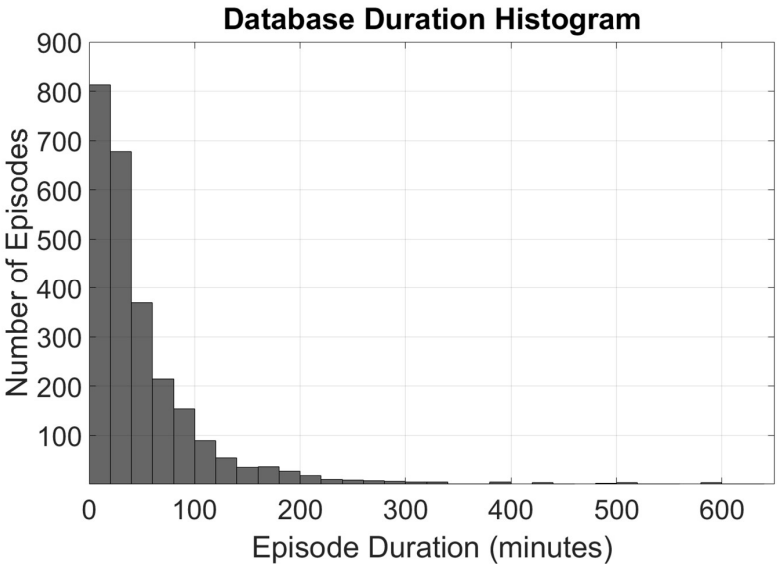

(b) *Episode duration*

Figure 6.1: *Histograms related to the database episodes obtained from the 39.6 GHz.*

6.2 Procedure Description — Cosecant Scaling plus events summation

The presentation of this procedure follows the one exposed in the paper [55]. The generation of the time series follows the formulation of the Rainy Time Series Generator (RTSG) presented in [11], and [23], that consists in subdividing the episodes into different classes according their peak value. The assumption is that by selecting a set of episodes from the ITALSAT database and, if necessary, scaling it with the factor shown in (6.1) it is possible to reproduce the rain attenuation statistics for any other site at a different frequency, rain height and elevation [11]].

$$F = \frac{H_r - h}{H_{r,ref} - h_{ref}} \frac{sin(\theta_{ref})}{sin(\theta)} \left(\frac{f}{f_{ref}} \right)^{1.72} \tag{6.1}$$

H_r and h are respectively the rain height (in km) and the height a.m.s.l (also in km), θ is the elevation angle and f is the frequency in GHz, all referred to the link that is going to be simulated. The parameters identified by the subscript ref stands for the height, elevation and frequency of the collected database.

For our purposes, the episodes are scaled, according to the difference in the elevation angle, by using the factor $[sin(\theta_{ref})/sin(\theta)]$ but this factor should be applied statistically only in situations where the link crosses one rain structure, as depicted in Figure 6.2 In such cases, in fact, the rainy path length increases according to the elevation-scaling factor.

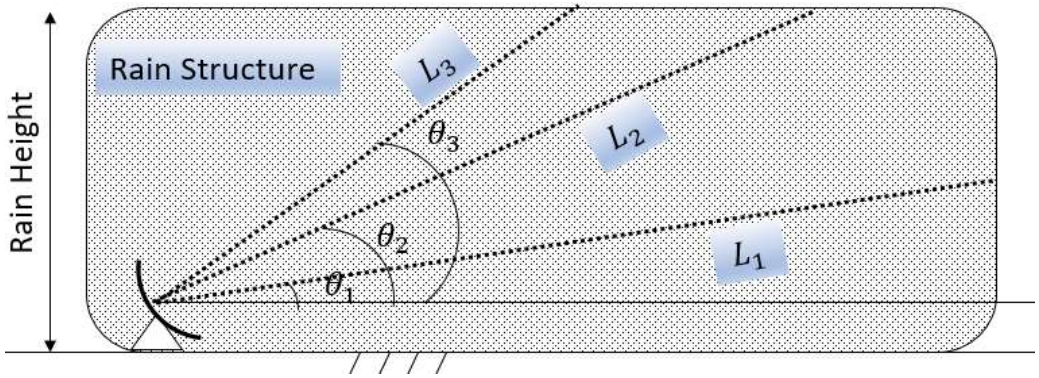

Figure 6.2: *Situation in which the elevation scaling factor is strictly valid.*

However, we observed — from simulations using the rain maps provided by the MultiEXCELL — that for the lowest elevation angles, with the increasing of the path length, the probability of having situations where the link crosses more than one rain structure (that are not crossed at the higher elevations) also increases. This situation is shown in Figure 6.3.

As an example, Figure 6.4 and Fig. 6.5 show rain attenuation "events" composed by contiguous attenuation samples along a MultiEXCELL map for different elevation angles. It is possible to see that for 5° there is a "superposed" event that is not present in the other elevations. An extended analysis of the attenuation events derived from simulations (contiguous samples at different elevation angles) have clearly shown that there are also situations where the value of the attenuation is the same for 5° and 10°

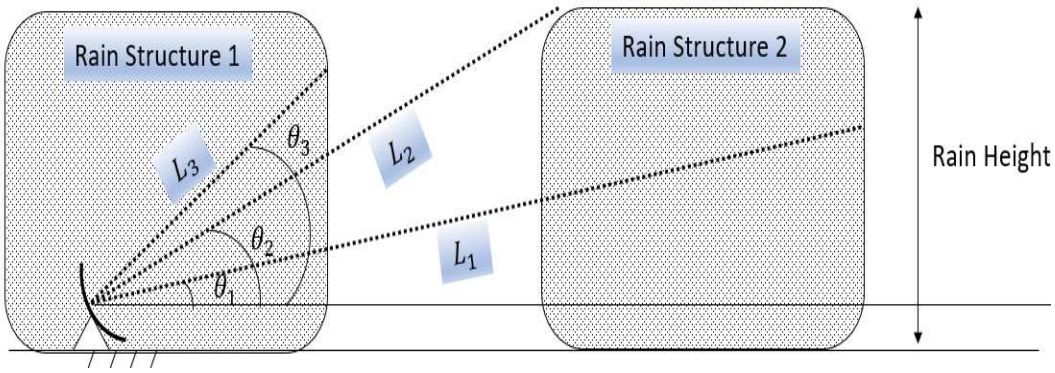

Figure 6.3: *Situation where the elevation scaling factor is not valid.*

and also cases (as the very last peak in the right side of the Fig. 6.4) in which the attenuation at 20° is almost equal to the one in 15°, 10° and 5°. These variety of cases obviously increases the complexity of the models for scaling the time series of rain attenuation from one elevation to another.

Based on the considerations above we propose a procedure to generate the time series for elevation angles below 10° which appears to be a cross angle value. This procedure consists in the following five steps:

1. First, the rain attenuation database is scaled with the factor $[sin(\theta_{ref})/sin(\theta)]$ from its original elevation (37.7°) to 10°.

2. The resulting database is afterwards enlarged by 20 times by means of a summation of two episodes with the aim of reproducing the situation depicted in Figure 6.3. This sum is done according to the following algorithm:

   (a) Episodes selection: two episodes are picked-up randomly;

   (b) Length normalization: the shortest of the two episodes is then filled with zeros in order to equalize both lengths. The number of zeros to be inserted is distributed symmetrically at both sides of the episode;

   (c) Random shift: then a random percentage and also a random direction (left or right) is chosen. For instance, if in step 'b' 10 zeros were inserted and the random percentage is 30% and the direction 'right', the episode will be shifted 3 samples to right. This step provides the possibility of a large number of different combinations between the episodes.

   (d) Event summation: the longer episode is then summed up with the shorter one (after steps b and c) and the result is a new synthetic episode to be stored in the new database.

   This new database is composed by the original one together with the combined episodes. The assumption is that the scaling presented in the step 1 covers the effect of enlargement in the path-length across the single structure, while the summation presented in the step 2 covers the situations where more than one rain structure is crossed. Figure 6.6 illustrates the procedure used to generate the synthetic episodes. The final database contains the original ITALSAT database and

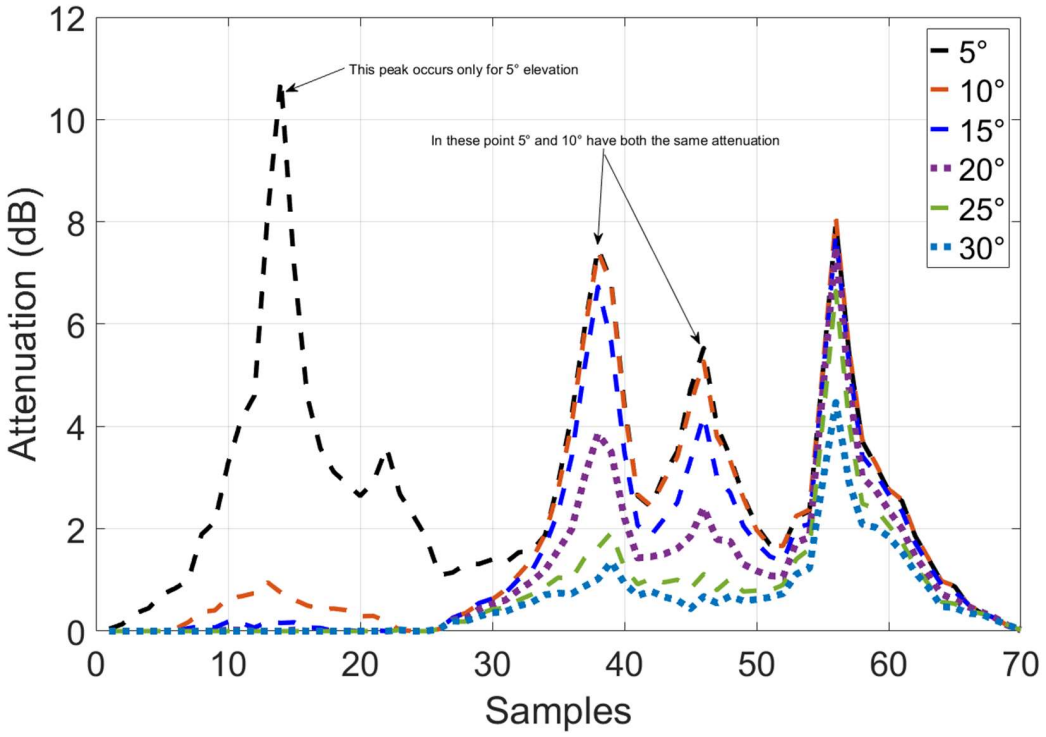

Figure 6.4: *Rain attenuation "event" composed by contiguous samples attenuation samples along a MultiEXCELL map for different elevation angles — sample 1, Spino d'Adda, 39.6 GHz.*

48792 synthetic episodes generated as described above. The histograms of peak attenuation and duration of the enlarged database are shown in Figure 6.7.

3. The new enlarged database is divided in 14 classes according to the peak attenuation of the episodes. Table 6.1 shows the classes with the respective ranges, the number of episodes and also the total duration of the events in each class. The choice of the range of each class was done according to the following criteria:

   (a) All the peak attenuations of the episodes (both real and synthetic) present in the database should be mapped;

   (b) The number of episodes in each class should be significant.

4. The next step is to evaluate the CCDF (base functions) for each class. Figure 6.8 shows some of them of the enlarged database.

5. The generation of the rain attenuation time series consists now in the selection of a subset of episodes pertaining to the enlarged database which summed together will reproduce the yearly CCDF of rain attenuation for a specific site. Each class is assigned with a weight that drives the selection of episodes. The weights come from an optimization procedure where the annual CCDF is fitted by the summation of the base functions by minimizing the error function expressed in (6.2)

$$d(W_{R,i}) = P(A_R)_{OBF} - P(A_R)_{REF} \tag{6.2}$$

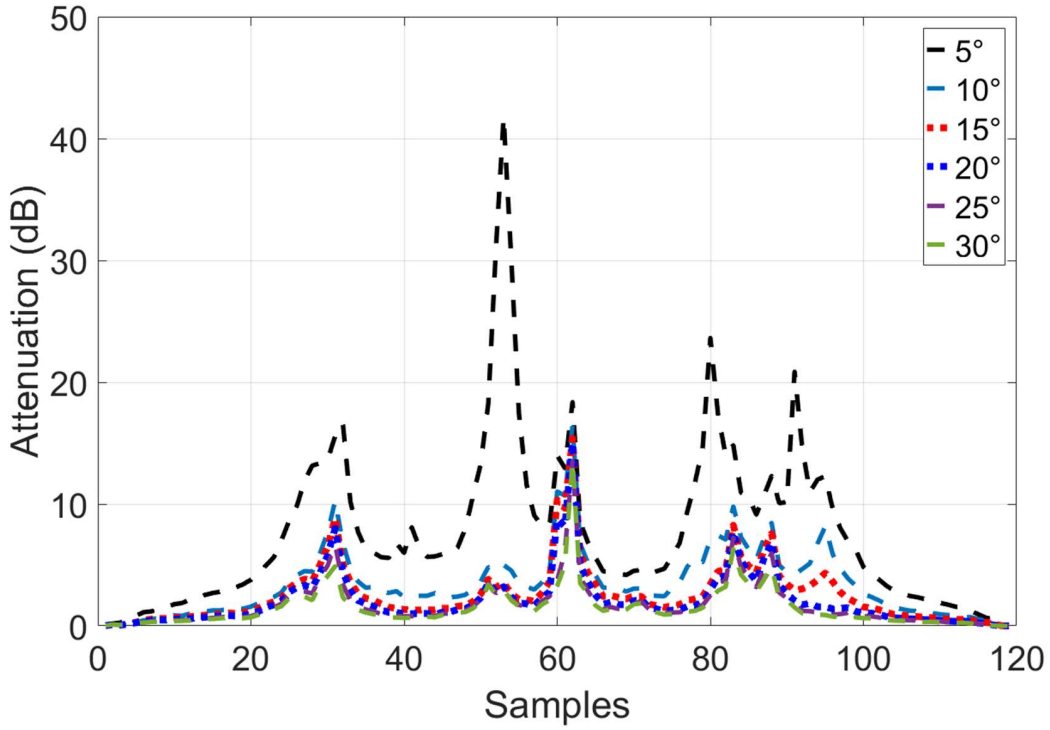

Figure 6.5: *Rain attenuation "event" composed by contiguous samples attenuation samples along a MultiEXCELL map for different elevation angles — sample 2, Spino d'Adda, 39.6 GHz.*

Where $W_{R,i}$ is the vector of weights; $P(A_R)_{OBF}$ is the objective function that — for these preliminary results — is obtained by simulation on the MultiEXCELL maps; $P(A_R)_{REF}$ is the reconstructed CCDF that is a combination of the weights and the base functions expressed by (6.3) [11]. The optimization procedure is constrained because the sum of the weights must be equal to the probability of having rain attenuation greater than zero. This value is also obtained from the simulations based on the MultiEXCELL maps.

$$P(A_R)_{REF} = \sum_{i=1}^{M} W_{R,i} P(A_R)_i \tag{6.3}$$

Where $P(A_R)_i$ are the base functions (the CCDFs for each of the classes in which the database is subdivided) and M is the number of classes.

6. The weights obtained give the number of events that must be selected from each class in order to match the objective CCDF. The events are chosen randomly among each class according to the weights. After this procedure we add to the time series obtained a vector of zeros in such a way the non-rainy time is considered and the CCDF can be evaluated.

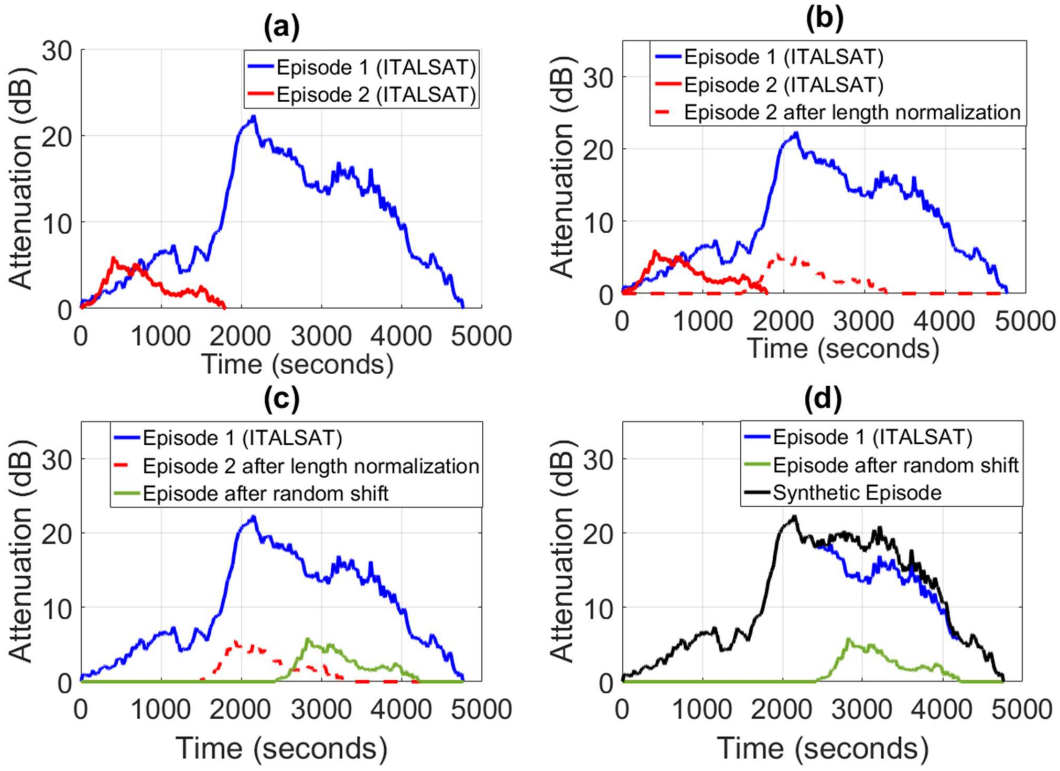

Figure 6.6: *Database enlargement procedure: (a) randomly episodes selection; (b) length normalization; (c) random shift; and (d) synthetic episode generated by summation.*

Table 6.1: *Classes division: range, number of episodes per class and total duration of each class.*

Class	Peak Attenuation	Number of Episodes	Total Duration (hours)
1	$A_p \leq 5dB$	448	273.5
2	$5dB < A_p \leq 7dB$	1189	999.8
3	$7dB < A_p \leq 10dB$	3761	3521.3
4	$10dB < A_p \leq 15dB$	7589	7279.7
5	$15dB < A_p \leq 20dB$	6676	7579.1
6	$20dB < A_p \leq 30dB$	9376	1235.5
7	$30dB < A_p \leq 40dB$	5913	9226.2
8	$40dB < A_p \leq 60dB$	7240	1304
9	$60dB < A_p \leq 90dB$	4858	9027.1
10	$90dB < A_p \leq 120dB$	2018	4096.7
11	$120dB < A_p \leq 150dB$	970	1619.3
12	$150dB < A_p \leq 190dB$	1075	2271.9
13	$190dB < A_p \leq 240dB$	231	541.6
14	$A_p \geq 240dB$	16	30.8

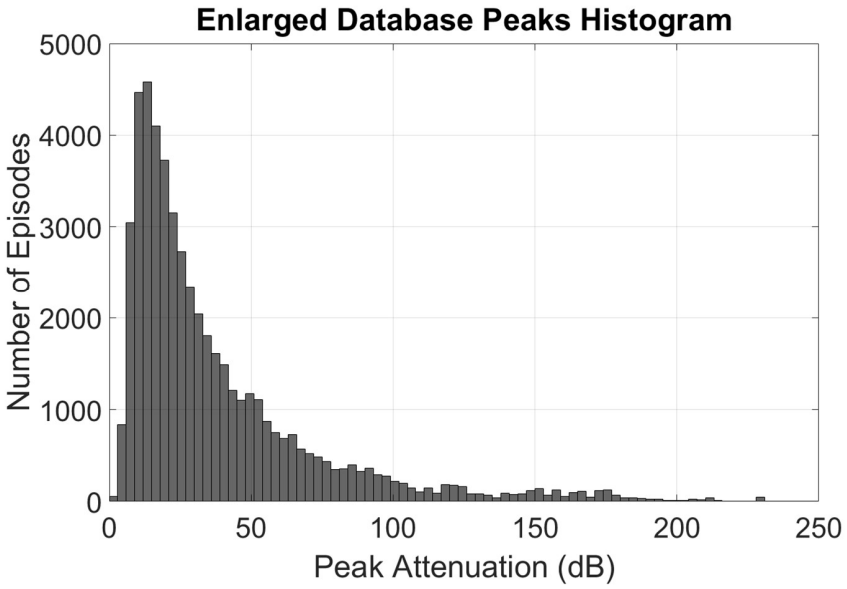

(a) *Peak attenuation*

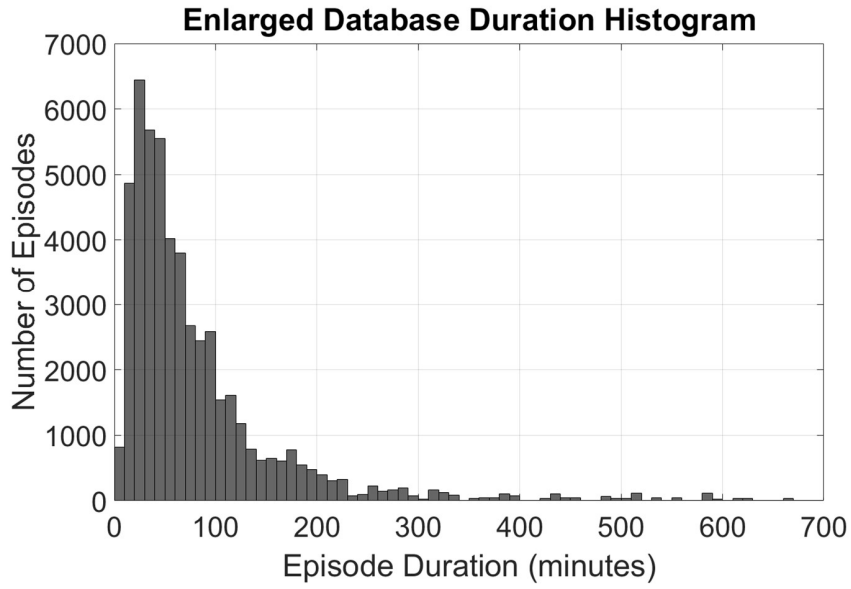

(b) *Episode duration*

Figure 6.7: *Histograms relative to the enlarged database episodes.*

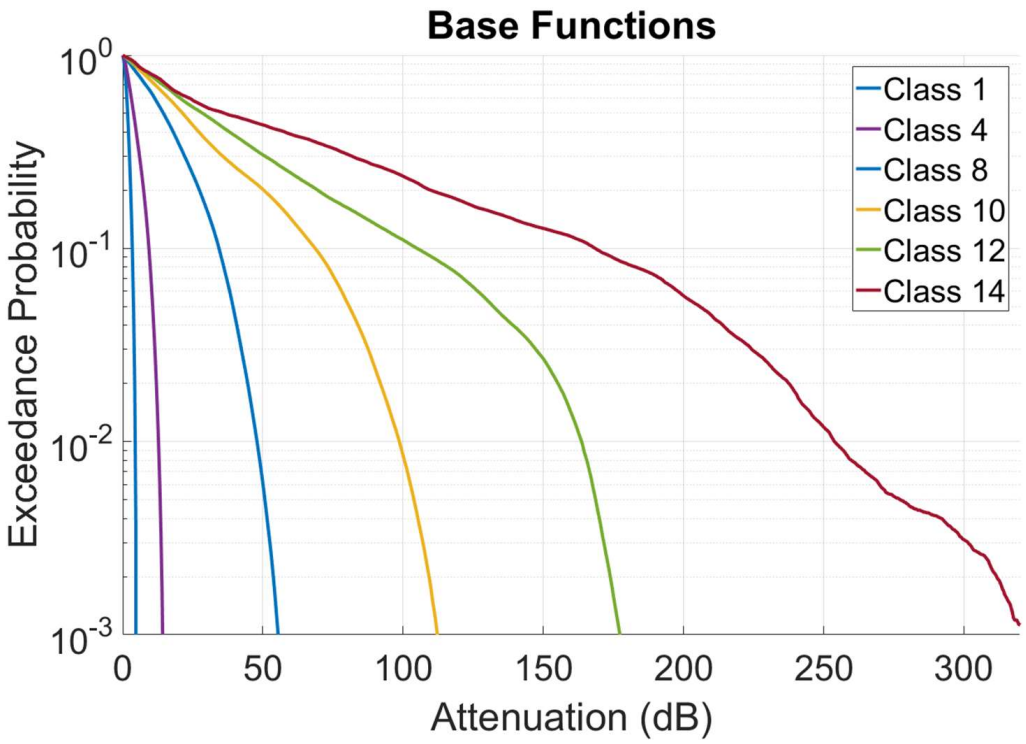

Figure 6.8: *Base functions for some of the enlarged database classes.*

6.3 Results

As input objective function $P(A_R)_{OBF}$, we used the CCDF obtained from simulations for the site Spino d'Adda (reference CCDF). The frequency is 39.6 GHz with circular polarization (for sake of simplicity we used the same frequency and polarization of the raw database). Figure 6.9 shows the CCDFs obtained by three different time series generated with the described procedure and as it is possible to see, all of them match the reference CCDF. Table 6.2 lists the optimized weights for each class, in other words, the percentage of rain events that are going to be picked-up from each of the classes.

The same procedure was also applied to the 18.7 GHz database and the results are presented in Fig. 6.10: CCDFs based on three different replicas of the generate time series (10 years) of rain attenuation at 5° elevation and frequency 18.7 GHz with vertical polarization compared with the simulation using MultiEXCELL maps for Spino d'Adda, Italy. Figure 6.10 we show the CCDFs of 3 replicas of time series generated for Spino d'Adda at 5°, 18.7 GHz with vertical polarization, compared with the result obtained with the simulations using the MultiEXCELL maps.

Figure 6.9: *CCDFs based on three different replicas of the generate time series (10 years) of rain attenuation at 5° elevation and frequency 39.6 GHz with circular polarization compared with the simulation using MultiEXCELL maps.*

Figure 6.11 shows the CCDFs of 3 replicas of a 1-year time series generate for Miami, USA, at 27 GHz compared with the CCDF obtained with MultiEXCELL simulations. In order to adequate the range of the events to the new location, we scaled all the events in the modified database according to the differences in frequency and rain height by using the relation (6.1).

Table 6.2: *Optimized weights for each class.*

Weights	Value	Weights	Value
1	0.0050	8	0.0129
2	0	9	0.0095
3	0	10	0.0047
4	0	11	0.0027
5	0.0047	12	0.0027
6	0.0071	13	0.0002
7	0	14	0.0007

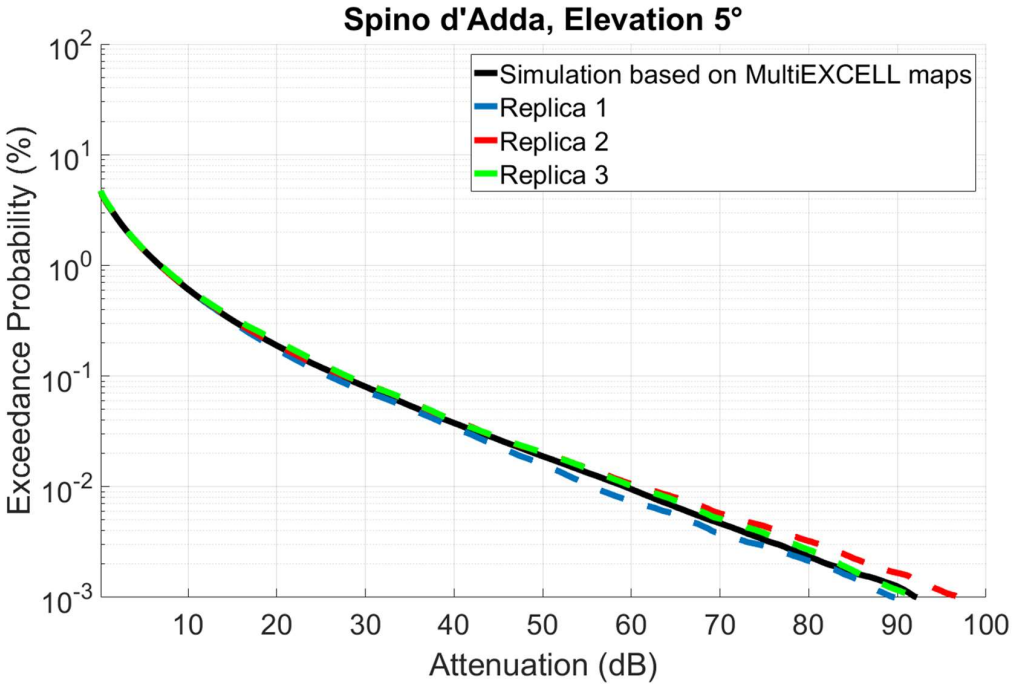

Figure 6.10: *CCDFs based on three different replicas of the generate time series (10 years) of rain attenuation at 5° elevation and frequency 18.7 GHz with vertical polarization d'Adda, Italy.*

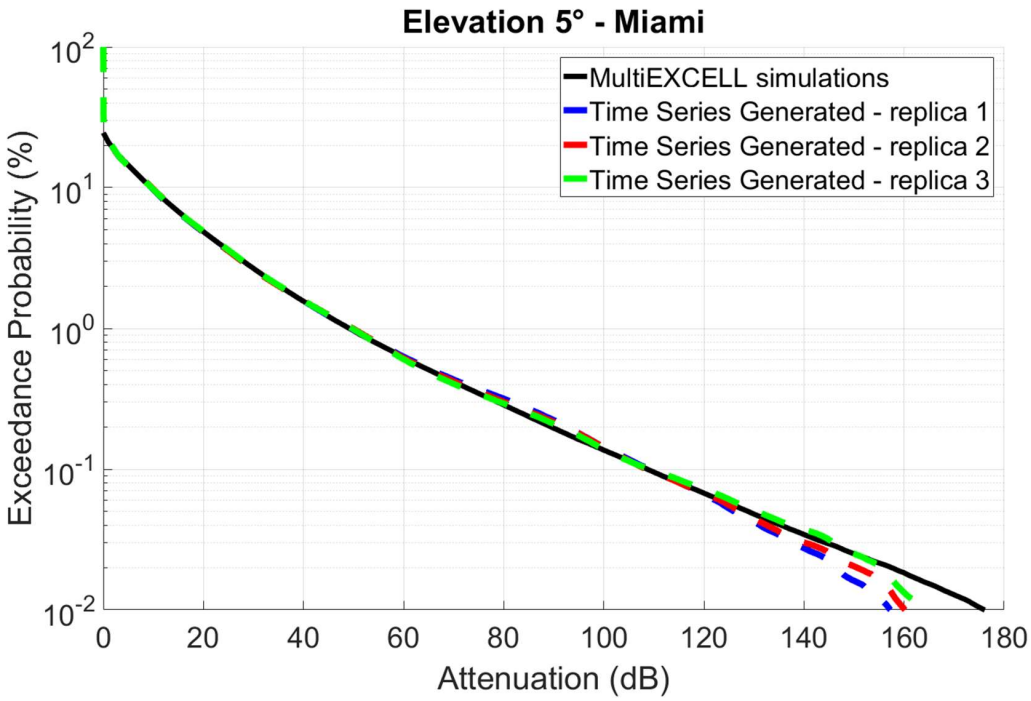

Figure 6.11: *CCDFs based on three different replicas of the generate time series (10 year) of rain attenuation at 5° elevation and frequency 27 GHz with circular polarization compared with the simulation using MultiEXCELL maps for Miami, USA.*

6.4 Final Remarks

We presented in this chapter a procedure to modify the ITALSAT attenuation database in order to make it more suitable for the generation of time series of rain attenuation for low elevation angles using the method proposed in [11]. This procedure is based on the summation of two rain attenuation episodes that tries to reproduce the situation in which the path length becomes long and the link crosses more than one rain structure. The results show that with this procedure is possible to generate time series that reproduce the long-term statistics of rain attenuation. Due to the lack of measurements at low elevation angles, the comparison was done by taking as reference the simulations based on MultiEXCELL maps.

The procedure presented is an important step towards the development of a time series generator of rain attenuation for NGEO satellites systems given that is possible to use the low elevation time series generator for the lower elevation point in the orbit for which there is a line of sight and then to develop a scaling procedure for the increasing of the elevation.

Further analysis can be done in order to optimize the way in which the ITALSAT database is modified. For instance, to investigate the feasibility of the aggregation of the events collected in the three beacons in a single larger database and then apply the procedure described in this chapter to it. Also, the division in classes can be optimized and the possibility of having dynamic class thresholds that depends on the frequency and on the rain height at which the time series will be generated should be considered.

CHAPTER 7

Elevation Scaling of Rain Attenuation Time Series

One of the main problems in the development of a time series generator for NGEO applications is related to the need to produce for each "rain event" a set of time series, one for each elevation, that maintain the spatial correlation among them. This chapter presents the model for the scaling of elevation correlated rain attenuation time series. Starting from the one at the lowest elevation angle of interest (5° in our case) the model is able to scale it to any higher elevation in such a way that all the long-term statistics of $A(\theta)$ are matched and, at the same time, the one at the higher elevation directly derives from the one at the lower elevation. The main idea is to produce for each single non-zero sample of a time series at the minimum elevation, the corresponding one at any other elevation of interest. As shown in the previous chapter, the input time series we refer to, constitute an appropriate ensemble of rain events that summed up together mimics the long-term normalized attenuation CCDF. Because of the very strict relation between statistics and time series, we started from the assumption that the scaling factor derived at statistical level should be appropriate also at sample level and we validated this statement in this chapter. This procedure maintains the correlation between the time series of the different elevation angles.

7.1 Modelling

From the reference database of rain attenuation (Chapter 4), we derived the CCDFs from 5° to 90° with 1° step. Some of them are shown in Figure 7.1. Let's call $P_0(\theta)$ the probability of having rain attenuation greater than zero (i.e., the point in which the CCDF touches the vertical line of attenuation equal to 0 dB) for each elevation. All the CCDFs are then normalized [$\underline{P_0}(\theta)$] in such a way that $\underline{P_0}(5°) = 1$ as shown in Figure 7.2. This normalization is done in order to avoid any dependence of the model on the

probability of rain occurrence that, as known, changes from site to site (and also from year to year at the same site). The assumption under this normalization procedure is that any rain event that affects a link pointed to a given elevation is likely to affect also the link pointed to a lower one — but not vice versa. The scaling factor φ, that is the core of the model, was computed with reference to the normalized CCDFs.

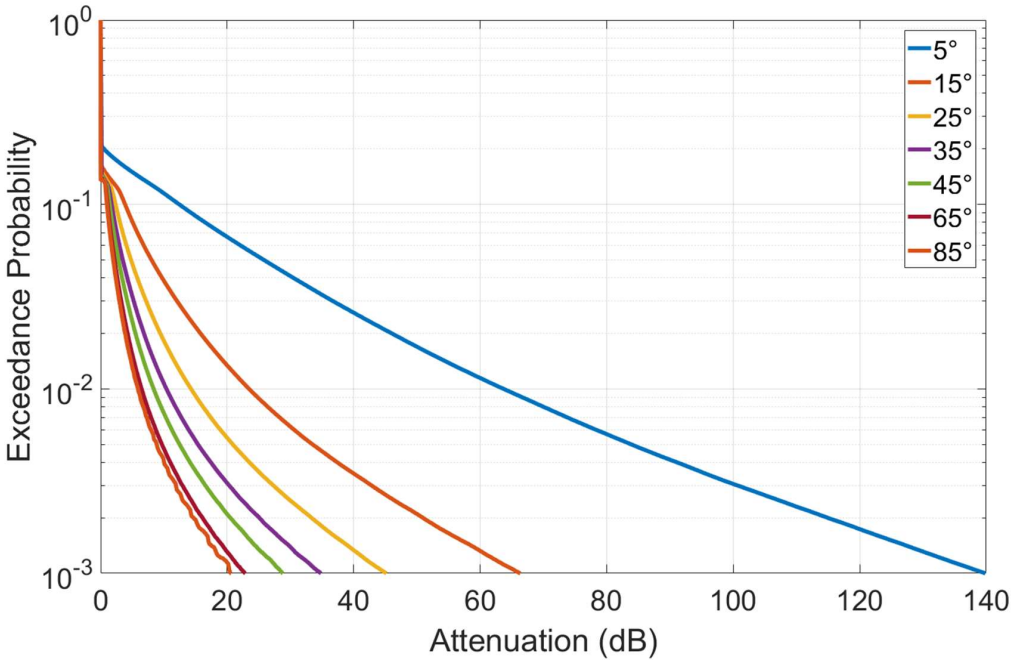

Figure 7.1: *Sample of the database of rain attenuation CCDFs obtained, 39.6 GHz circular polarization.*

First, we modelled $\underline{P_0}(\theta)$. Note from Figure 7.2 that, as expected, the probability $\underline{P_0}(\theta)$ decreases as the elevation increases, and the variation depends also on the rain height (not shown in the figure), i.e. from the two parameters influencing the rainy/attenuation path length. The analysis of the MultiEXCELL simulations have shown that $\underline{P_0}(\theta)$ can be modelled as in (7.1) , where θ varies from 6° to 90° and a,b, and c are coefficients dependent on the rain height h_r [km] and are given in (7.2).

$$\hat{\underline{P_0}}(\theta) = a[sin(\theta)cosec(\theta)]^b + c \tag{7.1}$$

$$a = 0.0714h_r + 0.2159 \tag{7.2a}$$
$$b = 0.01455h_r + 0.6499 \tag{7.2b}$$
$$c = -0.0711h_r + 0.7686 \tag{7.2c}$$

All the other points (attenuation exceeded at selected probability levels) of the normalized CCDFs are related to each other through the scaling factor $\varphi(\theta, p)$ (7.3).

$$\varphi(\theta, p) = \frac{A_{dB}(\theta, p)}{A_{dB}(5°, p)sin(5°)cosec(\theta)} \tag{7.3}$$

Where p is the probability level in the CCDF.

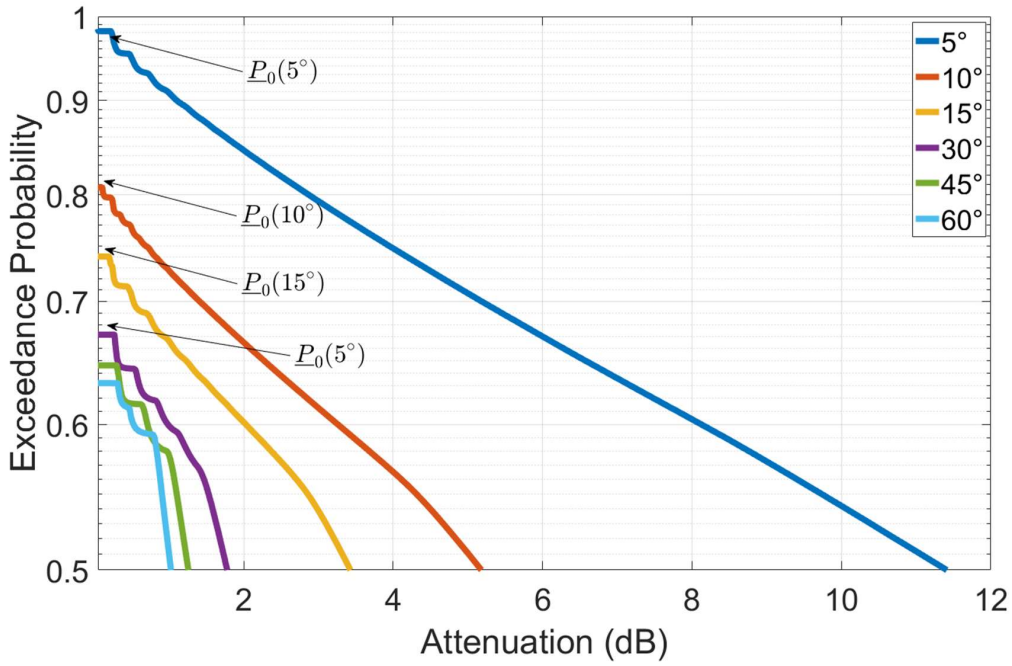

Figure 7.2: *CCDFs normalized to the 5° elevation (detail) 39.6 GHz circular polarization.*

Figure 7.3 shows the scaling factor φ evaluated for some elevations and for probabilities from 0.001 to 1. It is evident the need to subdivide the probability scale at least in two ranges for an appropriate modelling. In turn, for probabilities greater than 0.1, it is also necessary to use another type of function for modelling. Based on these considerations, we modelled a generic function $\varphi(\theta, p)$ for the two different probability, separately, ranges as follows:

(a) $0.1 \leq p < \underline{P_0}(\theta)$

For the higher probability range, the simulations shows that we can model the scaling factor by means of the polynomial of degree 2 expressed in (7.4). Because the probability level $\underline{P_0}(\theta)$ changes with the elevation angle, the modelling is not trivial and, even using the same polynomial model, its coefficients (α_1,α_2, and α_3) cannot be obtained from a single function, but we identified two different ranges as shown in (7.5) — namely, a linear range ($p \geq 0.5$) and an exponential one ($p < 0.5$).

$$hat\varphi(p, \theta) = \alpha_1 p^2 + \alpha_2 p + \alpha_3 \tag{7.4}$$

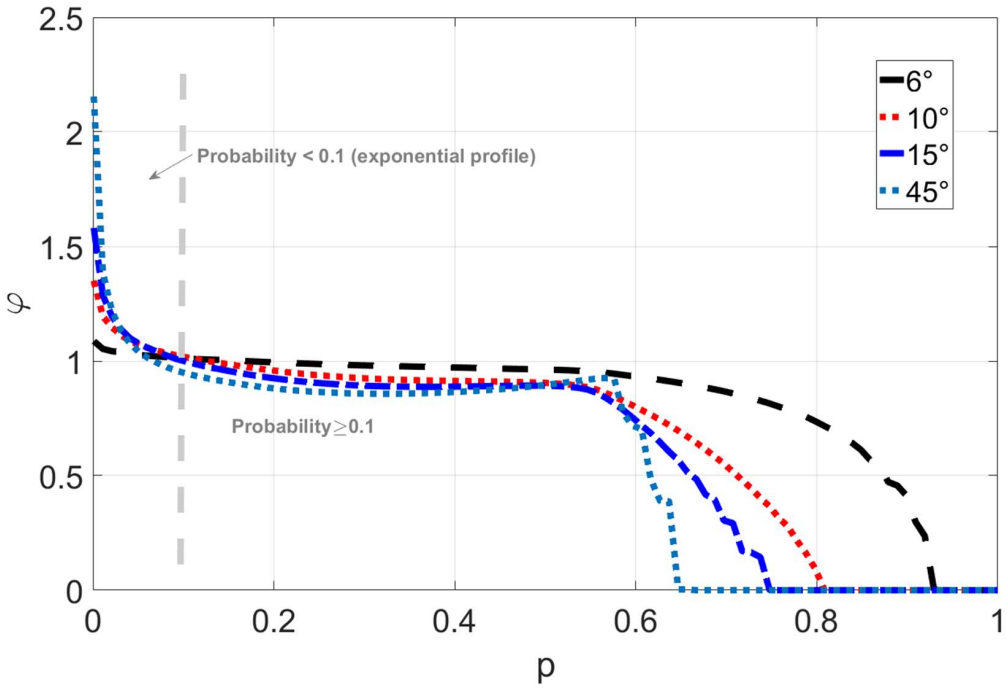

Figure 7.3: *CCDFs normalized to the 5° elevation (detail) 39.6 GHz circular polarization.*

$$
\begin{aligned}
&\text{For} \quad p \geq 5 \\
&\qquad \alpha_1 = -1.361\theta + 5.797 \\
&\qquad \alpha_2 = 1.483\theta - 7.394 \\
&\qquad \alpha_3 = -0.4032\theta + 3.204 \\
&\text{For} \quad p < 5 \\
&\qquad \alpha_1 = a_1 e^{b_1\theta} + c_1 e^{d_1\theta} \\
&\qquad \alpha_2 = a_2 e^{b_2\theta} + c_2 e^{d_2\theta} \\
&\qquad \alpha_3 = a_3 e^{b_3\theta} + c_3 e^{d_3\theta}
\end{aligned}
\tag{7.5}
$$

Table 7.1: *Coefficients of the equation (7.5).*

	a_j	b_j	c_j	d_j
$j = 1$	1.656	0.0002381	-6.32	-0.235
$j = 2$	-1.156	- 0.0007235	6.82	-0.3262
$j = 3$ and $\theta \leq 12°$	1.259	-0.008586	-0.6954	-0.2412
$j = 3$ and $\theta > 12°$	0.1539	-0.05058	1.018	$5.767\text{x}10^{-5}$

(b) $p < 0.1$ In the lower range of probabilities ($p < 0.1$), φ follows an exponential behavior for any elevations. Taking into account this exponential profile, the modelled scaling factor $\varphi(p, \theta)$ can be expressed by the relation presented in (7.6), where the parameters β_1 and β_2 are defined by the relations (7.7) and (7.8).

$$\varphi(p,\theta) = \beta_1 e^{\beta_2 log(p)} \tag{7.6}$$

$$\beta_1 = 0.5428e^{-0.08142\theta} + 0.6473e^{-0.00108\theta} \tag{7.7}$$

$$\beta_2 = -0.3817e^{0.002311\theta} + 0.5507e^{-0.07894\theta} \tag{7.8}$$

7.2 Application of the scaling factor

The model input consists in the non-zero attenuation samples of the $5°$ time series. Because of this we have done the normalization of the CCDFs with the assumption that $P_0(5°) = 1$. In order to obtain this input, one possible way is:

- Retrieve the $5°$ elevation CCDF of rain attenuation for the site of interest. This can be done by scaling to $5°$ the local CCDF (measured or predicted by models at a given elevation angle) with the procedure described in Chapter 5.
- Use the obtained CCDF as input to the method proposed in Chapter 6 that generates a set of time series for low elevation angles by a proper selection of rain attenuation events present in the modified ITALSAT database.

Figure 7.4 shows a simple block diagram that illustrates the procedure. The block "$\hat{\varphi}$ Generator" produces for each sample of the input time series the corresponding value $\hat{\varphi}$ to be multiplied with. It consists in the implementation of (7.4) and (7.4) according to the probability level of the sample in the input coming from the block "CCDF evaluation". Once the scaling factor $\hat{\varphi}(\theta, p)$ is evaluated, the model consists in multiply it by the input sample scaled with the cosecant relation as shown in (7.9).

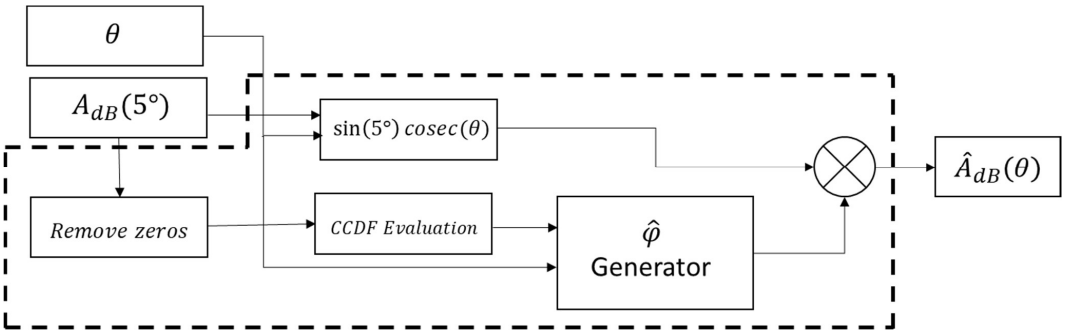

Figure 7.4: *Scaling factor application diagram.*

$$\hat{A}_d B(\theta, n) = A_d B(5°, n)[sin(5°)cosec(\theta)]\hat{\varphi}(\theta, p) \tag{7.9}$$

Where n is the number of the sample in the time series.

7.3 Results

In this subsection we present some results obtained with the scaling procedure. The evaluation of the scaling accuracy is done according to the figure of merit (ϵ) proposed in the ITU-R Recommendation P. 311-15 [53] and shown in (5.6) multiplied by 100 in percentage. We also used its root-mean-square (RMS) (5.7) value. The evaluation of ϵ is carried out at the following probability levels: [0.5 0.4 0.3 0.2 0.1 0.05 0.03 0.02 0.01 0.005 0.003 0.002 0.001].

Figure 7.5 shows the CCDFs of the synthetic time series (obtained with MultiEXCELL) scaled from 5° to 90° for Spino d'Adda. We can notice that the proposed scaling matches well the MultiEXCELL reference (target) even for this large difference between the two elevations.

Figure 7.6 shows an example of rain attenuation event generated with the procedure presented in Chapter 6 and scaled with the model proposed in this chapter. We can observe that the scaled event is not only smaller in terms of amplitude, but it is also shorter than the event at 5Â° degrees. However, it is possible to note that the peaks of the event are more preserved in respect to the customary cosecant scaling.

Since the data used for modelling were obtained from the maps generated for Spino d'Adda site, it was expected that the model would work well for them. Hence, in order to verify the feasibility of the application of the scaling for different sites, we used also the CCDFs obtained for another site, namely Miami - USA. The results are shown in Figure 7.7, and, though the agreement is so good as for the Spino d'Adda data, it is yet a good result when compared with the cosecant scaling. It is interesting to mention that the rain profile of Miami is completely different from the Spino d'Adda one, being the first more convective while the former is more stratiform.

In order to quantify, in some way, the goodness of the scaling Figure 4.2 shows the figure of merit RMS and mean values obtained at different elevation angles for Miami by which we can observe the improvement in respect to the cosecant scaling.

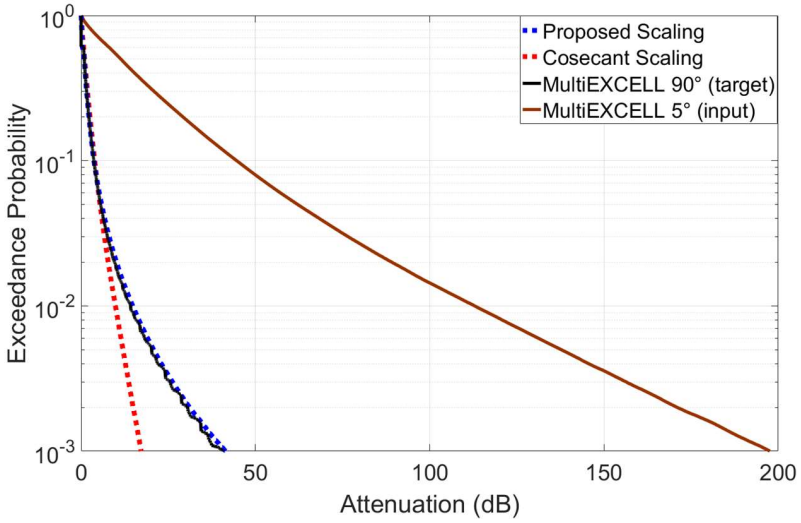

(a) *full picture*

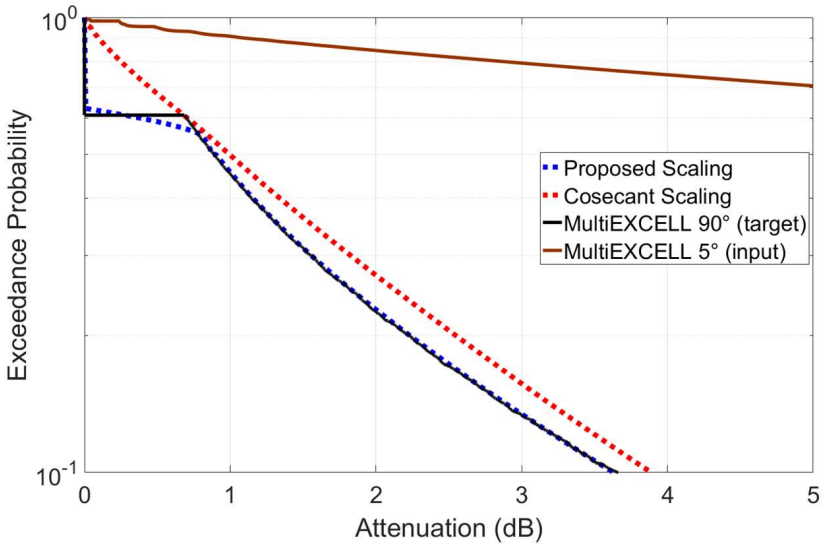

(b) *high probability range detail*

Figure 7.5: *CCDF of the time series scaled from 5° to 90° for Spino d'Adda, 39.6 GHz, circular polarization.*

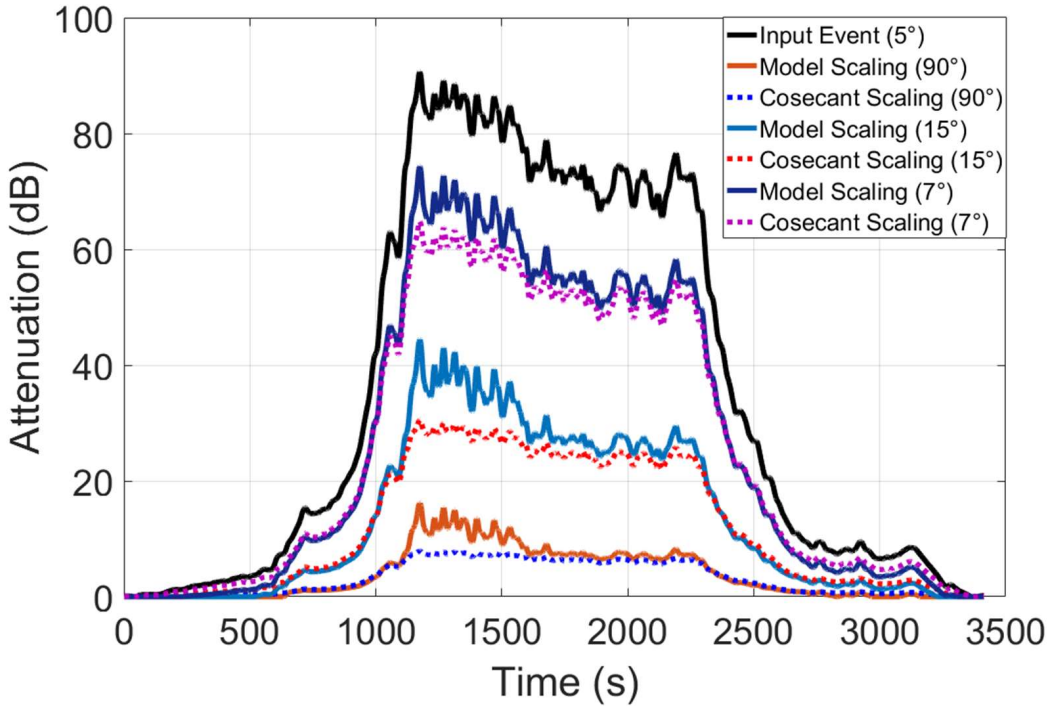

Figure 7.6: *Example of rain event generated by the method proposed in Chapter 6 and scaled from 5° to 7°, 15°, and 90° for Spino d'Adda, 39.6 GHZ.*

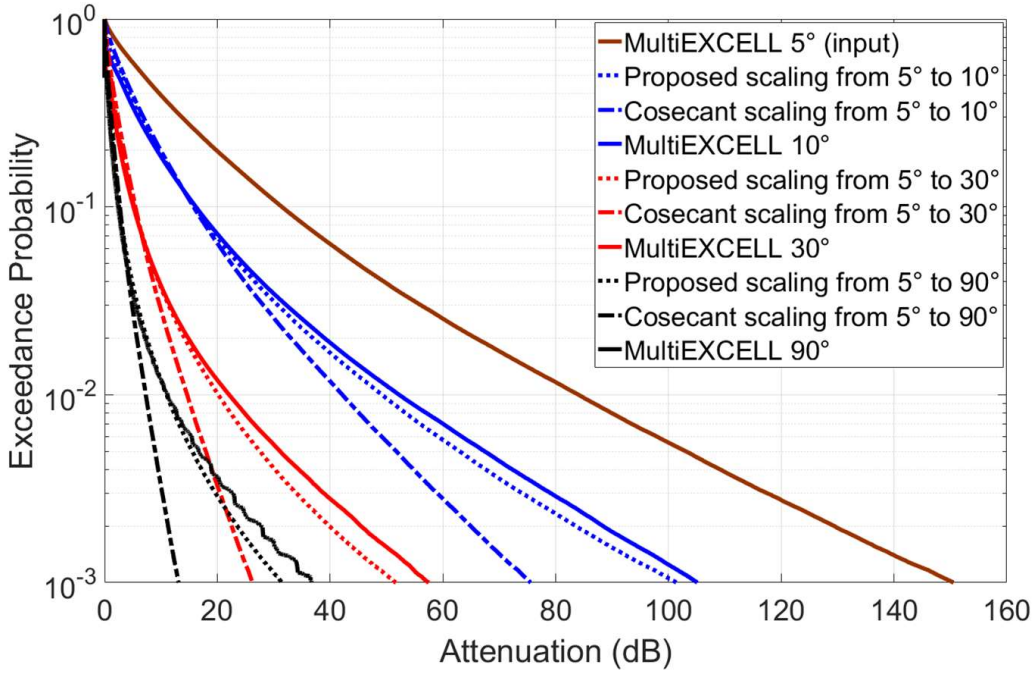

Figure 7.7: *Scaling procedure applied to the data obtained for Miami 27 GHz, circular polarization, for some elevation angles.*

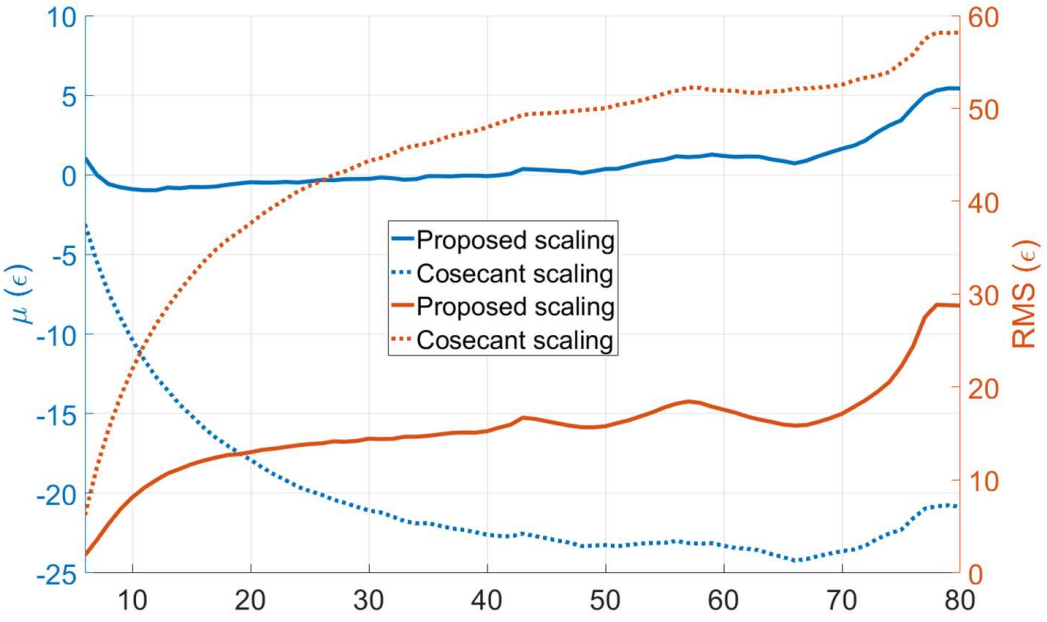

Figure 7.8: *Mean and RMS of the figure of merit evaluated from 6° to 80° elevation for Miami.*

7.4 Final Remarks

In this chapter, we presented a model to scale the time series of rain attenuation as a function of the satellite link elevation for satellite. It was shown, through simulations for two different sites (Spino d'Adda and Miami), that the proposed model exhibits a very good agreement when we compared in terms of the CCDFs.

CHAPTER 8

Azimuthal Variation of Rain Attenuation

This chapter presents the analysis of the azimuthal variation of the rain attenuation and suggests a model to evaluate the amplitude of the azimuthal interval where rain is present as from the simulations on the MultiEXCELL maps. This chapter is the basis of the publication [56] and describes what is inside the block "Azimuth window generator" in Fig. 3.1.

8.1 Simulations settings

Using the procedure described in Section 4.2, we performed specific simulations to estimate rain attenuation at any azimuth angle (0° to 179° in 1° step) and at seven different elevations (5°, 10°, 20°, 37°, 45°, 60°, 80° and 90°). The frequency used was 39.6 GHz with circular polarization as explained before. Fig. 8.1 illustrates the technique applied.

The radius (L) of each circle – equivalent to the horizontal projection of the path length – is dependent on the elevation angle and the rain height. For Spino D'Adda, we considered a rain height of 2.9 km, which gives an effective path length ranging from about 0.51 km at 80° elevation to around 33.15 km at 5° elevation.

We defined the azimuth window Az_w as the angular interval with attenuation continuously greater than zero. The window size depends on the path length (in other words, on the elevation and the rain height), on the distance between the Earth station and the rain structure and also on the rain structure's dimension. Figure 8.2 shows a sketch of Az_w. From Figure 8.1 it is easy to identify three possible situations of the link position with respect to the rain structure classified as follows:

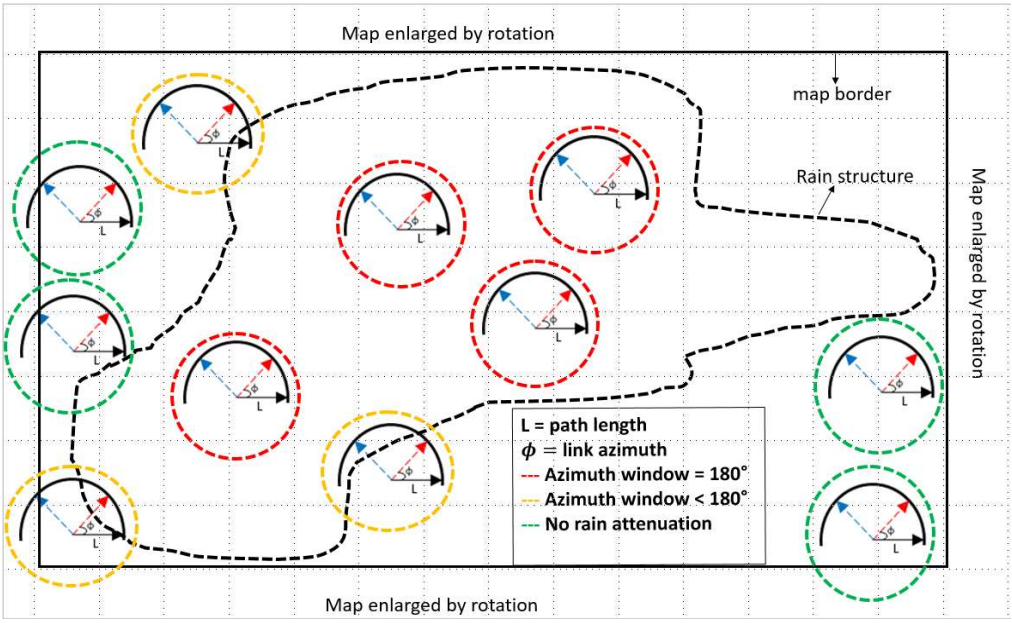

Figure 8.1: *Illustration of the procedure used to collect the rain attenuation samples.*

8.1.1 Rainy azimuth window = 180°

It is clear that when the ground station is inside the rain structure, the rain attenuation is extending over an azimuth window of 180Â°. These cases are equal to the number of rainy pixels within the maps.

8.1.2 Rainy azimuth window < 180°

Conversely, if the circles identified by the horizontal projection of the link cross the rain structure but the ground station is outside, the Az_w assumes values between 1° and 180°.

8.1.3 No rain attenuation

Finally, if the circle is completely outside the rain structure, there will be no rain attenuation.

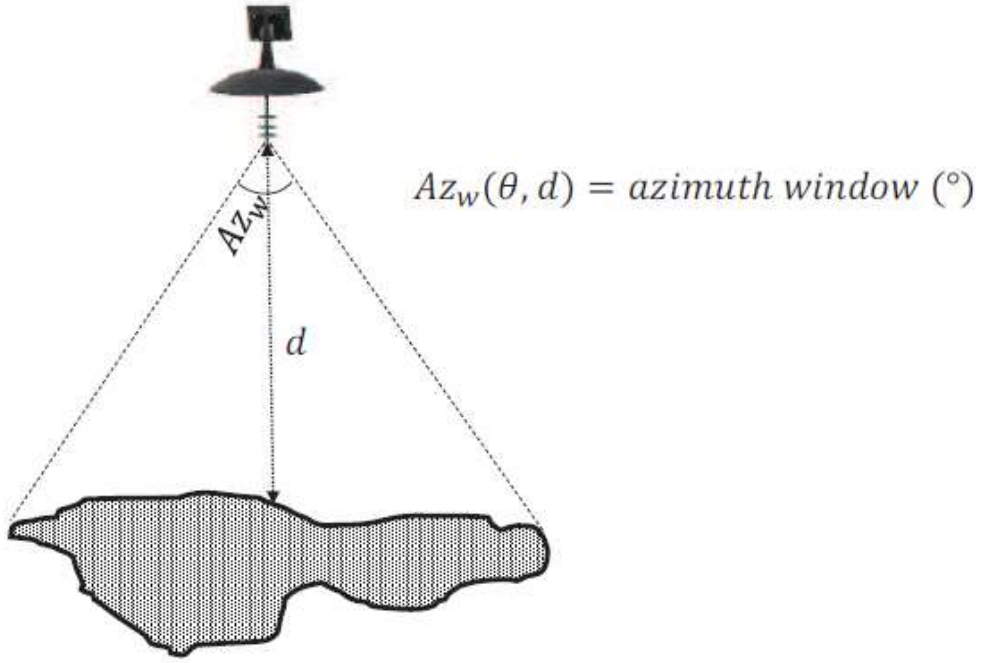

Figure 8.2: *Azimuth variation defining the azimuth window.*

8.2 Results from data analysis

According to [5], assuming a plain terrain over the area around ground station the fade levels at different azimuth directions will not show appreciable variations in terms of long-term statistics. Figure 8.3 shows the simulated yearly CCDF of rain attenuation for Spino D'Adda for three different azimuth angles (0°, 30° and 60°) at 37° elevation.

From simulations it was possible to identify the occurrence probabilities of each case described in section 8.1. The Az_w (in degrees) was evaluated over a total of 30576200 (230x230x578) samples per azimuth following this procedure:

i. For each pixel of the map a vector with 180 positions is stored containing the attenuation samples at all azimuth angles (from 0° to 179°);

ii. Then we counted the number of non-zeros contiguous samples in each vector from which to derive the size of the Az_w as shown in Figure 8.4 where an example is presented. In this case rain extends only from 0° to 87°.

Table 8.1 summarizes the results obtained in terms of probability of having Az_w between 0° and 180° for different elevation angles. As the probability of having an azimuth window equal to 180° is directly related to the rain coverage (see below), the values in Table 8.1 must be used after denormalization.

The histograms for the cases where Az_w is greater than 0° and smaller than 180° is shown in Figure 8.5 for four different elevations. We can see that the range of Az_w is relatively spread between 0° and 180°, even if it is possible to note some peaks in

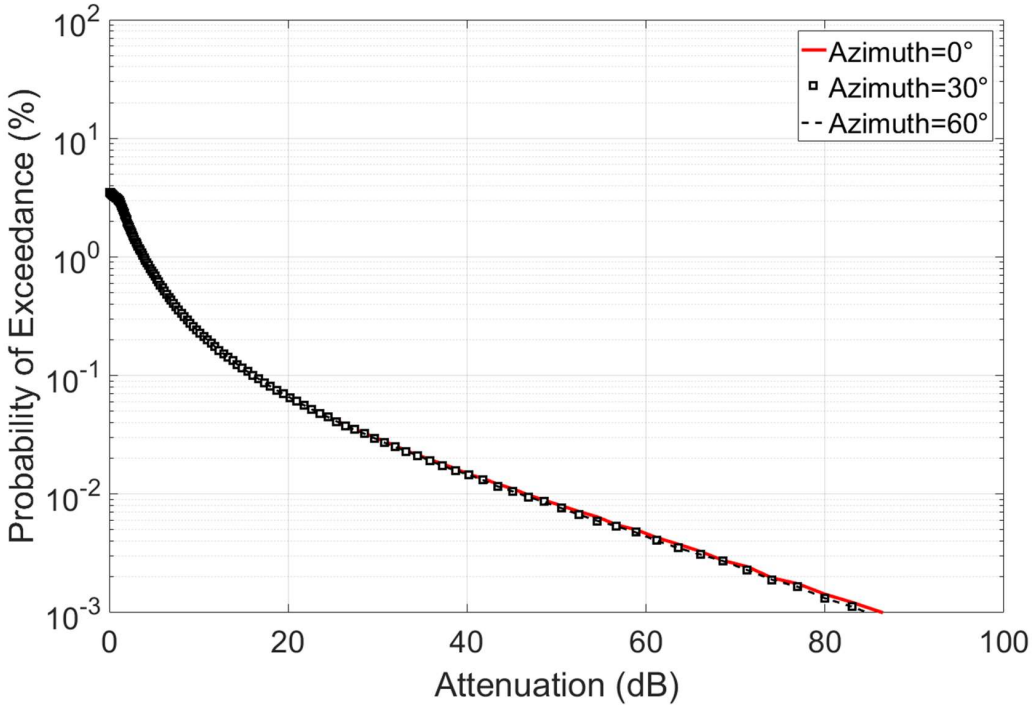

Figure 8.3: *Annual CCDF for different azimuth angles (39.6 GHz, circular polarization, 37° elevation).*

the histograms. As the modelling of all these peaks would result unfeasible, the best compromise should be to use a uniform distribution for this range of Az_w.

The ratio between probabilities shown in Table 8.1 depends on the rain height and on the cotangent of the elevation and can be modelled as in (8.1) . Figure 8.6 shows the relation (8.1) compared with the simulated results for two different heights (RH=2.9km and RH=5km) for several different link elevations.

$$\frac{P_{(0°<Az_w<180°)}}{P_{(Az_w=180°)}} = 0.06227 RH cotg(\theta) \tag{8.1}$$

Where RH is the rain height in km and θ is the elevation in degrees.

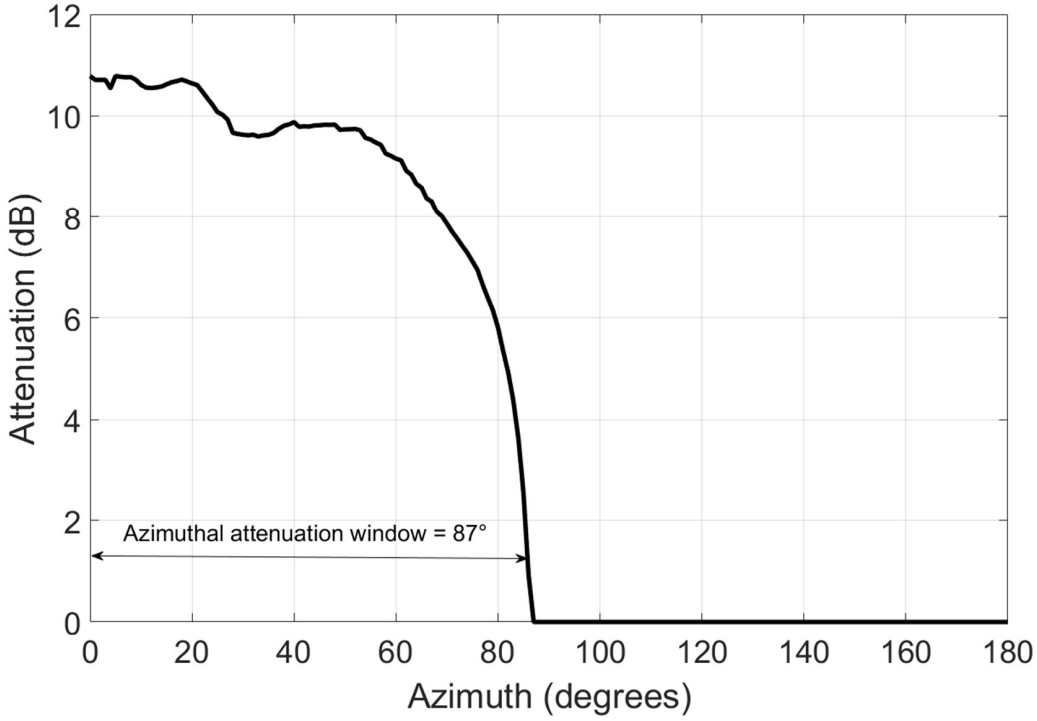

Figure 8.4: *Example of azimuthal attenuation window at 20° elevation.*

Table 8.1: *Ratio between the probability of having an azimuth window between 0° and 180° and the probability of having it equal to 180° as a function of link elevation.*

Elevations	$\frac{P_{(0° < Az_w < 180°)}}{P_{(Az_w = 180°)}}$
$\theta = 5°$	2.0167
$\theta = 10°$	1.1023
$\theta = 15°$	0.6934
$\theta = 20°$	0.4782
$\theta = 37°$	0.2659
$\theta = 45°$	0.1927
$\theta = 60°$	0.1373
$\theta = 80°$	0.0861
$\theta = 90°$	0

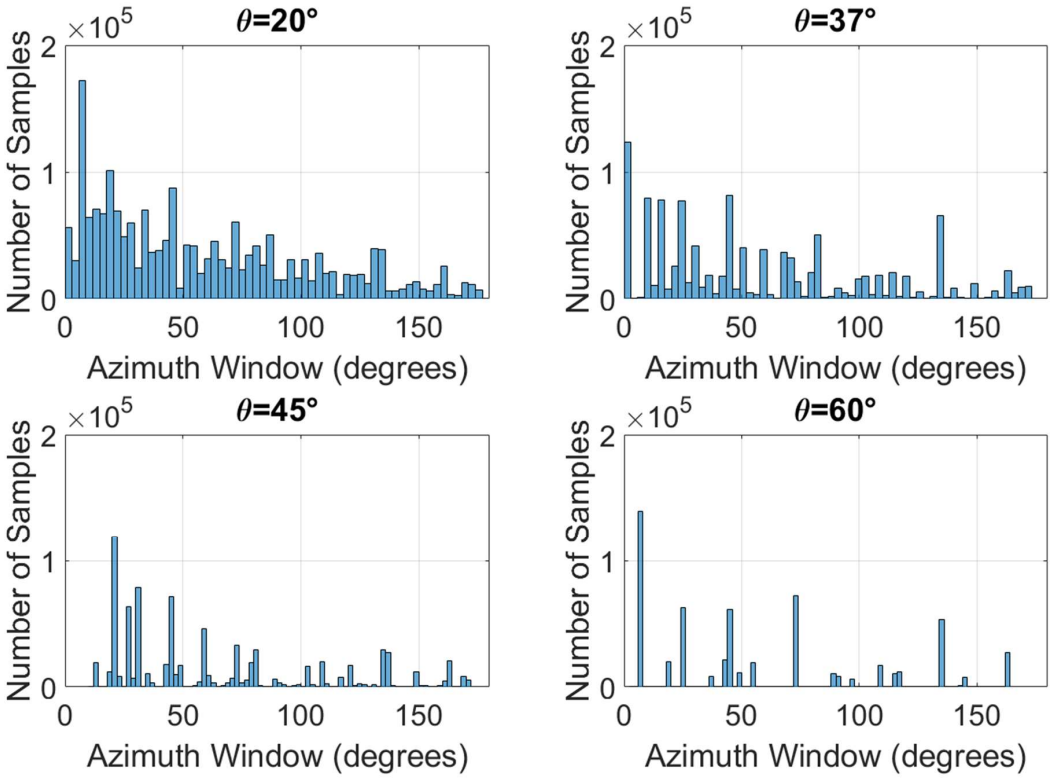

Figure 8.5: *Histograms of the situations in which the azimuth window is between 0° and 180° for different elevations.*

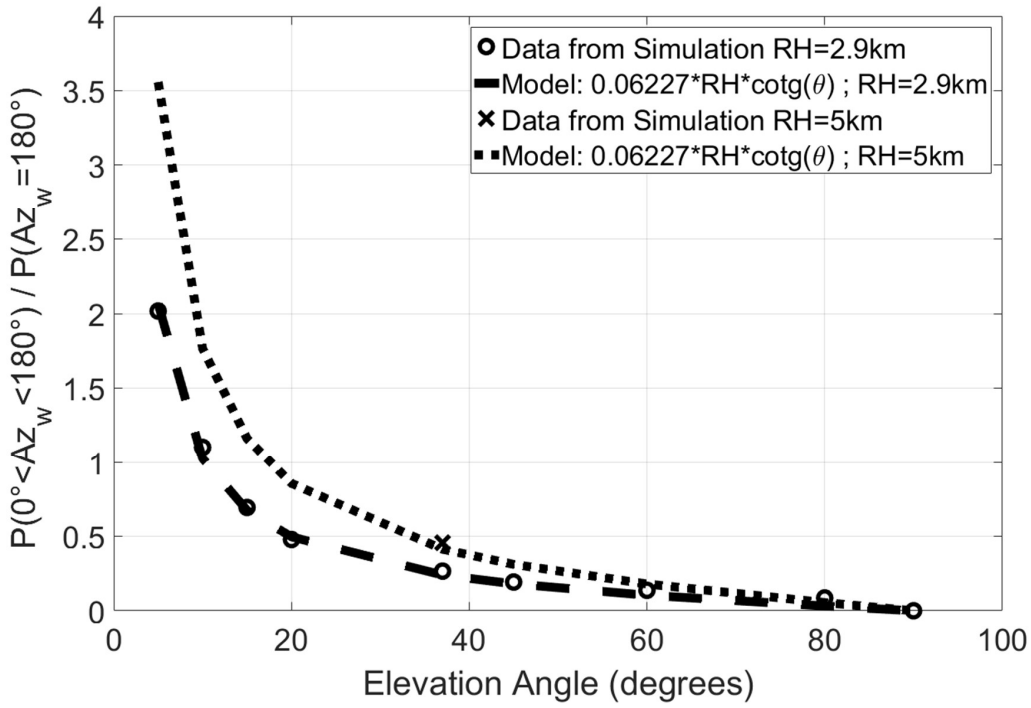

Figure 8.6: *Histograms of the situations in which the azimuth window is between 0° and 180° for different elevations.*

8.3 General procedure for NGEO satellites

Based on the considerations above and knowing that $P(Az_w = 180°)$ is the ratio between the rainy and total number of pixels in the set of maps (i. e. it does not dependents on the elevation), which is related to the rain probability of the selected site (P_0), we can to rewrite (8.1) as (8.2), defining a $\bar{P}_{(0°<Az_w<180°)}(\theta)$, where $P(Az_w = 180°)$ has been substituted by P_0.

$$\bar{P}_{(0°<Az_w<180°)}(\theta) = [0.06227RHcotg(\theta)]P_0 \tag{8.2}$$

However, as the azimuth window must be generated for each passage of the NGEO satellite which is seen by the ground station in a range of different elevations, it is necessary to define $\bar{P}_{(0°<Az_w<180°)}(pass)$ as a weighted arithmetic mean by considering the time percentage spent at each angle with respect to the total duration of the passage.

$$\bar{P}_{(0°<Az_w<180°)}(pass) = \frac{1}{t_p}\sum_{\theta=\theta_{min}}^{\theta max}[0.06227RHcotg(\theta)t_\theta]P_0 \tag{8.3}$$

Where t_p is the total time of the passage and t_θ is the time during which the satellite is pointed towards θ. Table 8.2 shows the values that the azimuth window should assume for the different probabilities.

Table 8.2: *Generation of the azimuth window in terms of time percentage.*

Time Percentage	Azimuth Window
$\boldsymbol{P_0}$ [probability of having rain in the site, related to $\boldsymbol{P(Az_w = 180°)}$] converted into time percentage	180°
$\boldsymbol{P(0° < Az_w < 180°)}$ converted into time percentage	The azimuth window is a random number generated from a uniform distribution between 1 and 179°
$\mathrm{P}(\boldsymbol{Az_w = 0°})$=1- [$\boldsymbol{P(Az_w = 180°)}$- $\boldsymbol{P(0° < Az_w < 180°)}$] converted into time percentage	0°

8.4 Application of the azimuth window to the NGEO rain attenuation time series generator

As in this work we assumed to have in input to the generator a rain attenuation time series generated at the lowest elevation of interest, the procedure to generate Az_w described before must be slightly adapted. First of all, as the presence or absence of rain attenuation is already contained in the input time series (all samples have $A > 0$), the probability of having Az_w equal to zero does not occur, Thus, there are two possible situations, namely: Az_w equals to 180° and as such the event is only scaled in elevation and the azimuthal variation is disregarded; or, the event is varying in elevation and also cut according to Az_w .

The first step of the procedure consists in the evaluation of the relation between the probability of having an azimuth window between 0° and 180° and the probability of having an azimuth window equals to 180°, as in (8.1), but weighted with the time that the satellite spends in elevation and divided by the total time of the passage (8.4). As the possibilities were reduce to two, that is to say, 180° or a number between 0° and 180°, we generate a random number with these two probabilities which sum must be equal to 1 as in (8.5).

$$\frac{P_{(0°<Az_w<180°)}(NGEO)}{P_{(Az_w=180°)}(NGEO)} = \frac{1}{t_p}\sum_{\theta=\theta_{min}}^{\theta max}[0.06227RHcotg(\theta)t_\theta] \tag{8.4}$$

$$P_{(0°<Az_w<180°)}(NGEO) + P_{(Az_w=180°)}(NGEO) = 1 \tag{8.5}$$

Once evaluated the relation between $P_{(0°<Az_w<180°)}(NGEO)$ and $P_{(Az_w=180°)}(NGEO)$, we can express $P_{(Az_w=180°)}(NGEO)$ as in (8.6).

$$P_{(Az_w=180°)}(NGEO) = \frac{1}{1 + P_{(0°<Az_w<180°)}(NGEO)} \tag{8.6}$$

The next step is two generate a random binary number according to the probabilities $P_{(0^\circ<Az_w<180^\circ)}(NGEO)$ and $P_{(Az_w=180^\circ)}(NGEO)$ respectively and evaluate the azimuth window as follows:

- If "0": the azimuth window is a random number from a uniform distribution between 1° and 179°;
- If "1": the azimuth window is equal to 180°.

8.5 Final Remarks

This chapter presented the analysis of the variability of rain attenuation with the azimuth of the NGEO satellite link. This aspect has been faced by introducing and quantifying the size of the azimuthal window with attenuation greater than zero. We have found that the percentage of azimuthal windows less than 180° degrees increases exponentially with the decreasing of elevation, as shown in (8.2). This analysis is basic in case of the NGEO satellite links where the elevation and azimuth positions are constantly changing in time. We presented two methods for the derivation of the azimuth windows: a general one, that takes into account only P_0, the rain height and the orbital positions of the satellite; and a specific one that is based on the specific input of our proposed model, namely, input time series of attenuation A>0 at the minimum elevation angle of the orbit (5° in our case).

CHAPTER 9

Clouds and Water Vapor Attenuation Scaling

This chapter presents the results for the scaling of the water vapor attenuation based on simulations that relies on the use of 3-D water vapor profiles generated for Spino d'Adda, Italy. The water vapour analysis has its main reference in [57]. This chapter is related with the block "Geometric scaling" in Fig. 3.2 since here we show that the use of the geometric scaling is feasible. In addition to water vapour, we also propose a methodology for scaling the attenuation contributions due to clouds that was derived from simulations using 3-D cloud maps generated for Spino d'Adda.

9.1 Water vapor fields database

The Stochastic MOdel of water Vapor (SMOV), first presented in [58], is a comprehensive methodology able to synthesize sets of three-dimensional (3-D) water vapor fields that realistically reproduce the spatial distribution of the water vapor content taking advantage of the generation of spatially correlated Gaussian fields. SMOV was developed on the basis of an extensive database of water vapor measurements collected by the MODIS sensor onboard the Aqua satellite: specifically, those data were employed to investigate the statistical distribution of the integrated water vapor content V (Weibull [58]), as well as its horizontal spatial distribution. In addition, the vertical profile of the water vapor content V was studied and modelled by investigating a large set of radiosonde observation (RAOBS) atmospheric profiles collected in several sites worldwide. The only input to SMOV is the Complementary Cumulative Distribution Function (CCDF) of V (integrated along the zenith path), which, in this work, was obtained from ten years of RAOBS data coming from the Milano Linate Airport. The application of SMOV led to assembling 1857 3-D water vapor fields, which are fully representative of a typical average year in the site of interest. The 3-D fields of water

vapor content have the following dimensions and resolutions:

- Horizontally: 200 km x 200 km (with 1 km x 1 km resolution);
- Vertically: 20 km (with 100 m resolution).

Fig.9.1 and Fig.9.2 show the horizontal distribution of V and its vertical profile, respectively, for one of the 3-D water vapor fields generated by SMOV and used in this work.

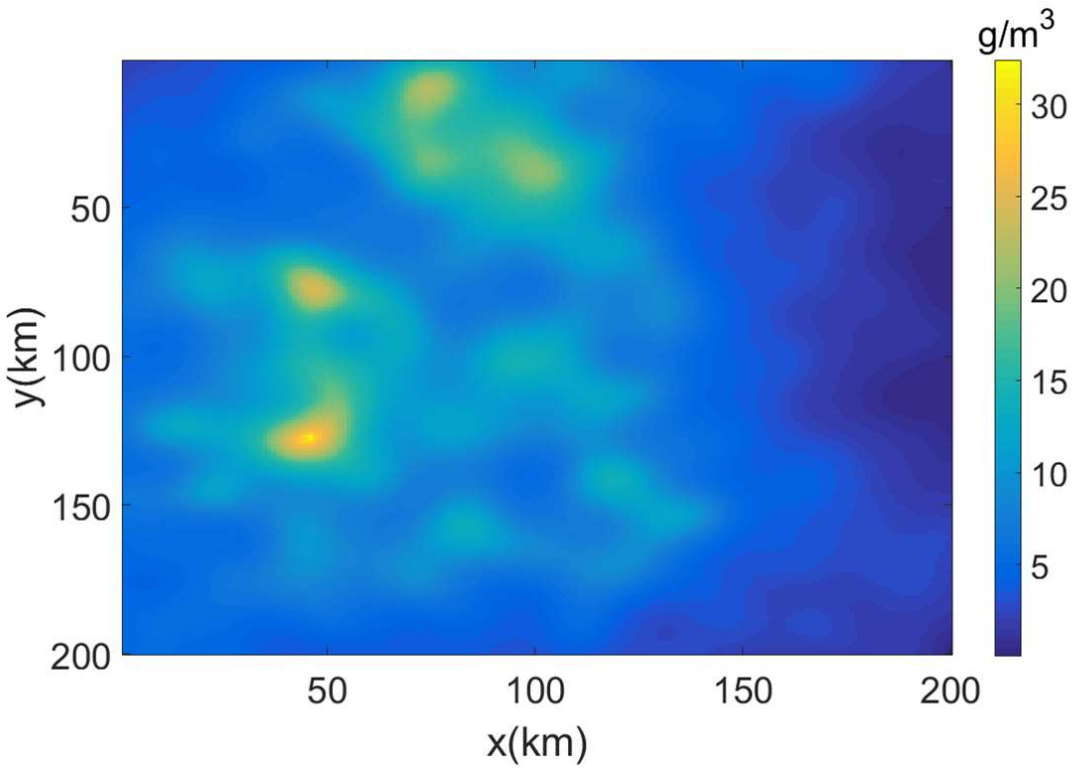

Figure 9.1: *Sample 3-D water vapor field generated with SMOV (water vapor content) — horizontal view (sea level).*

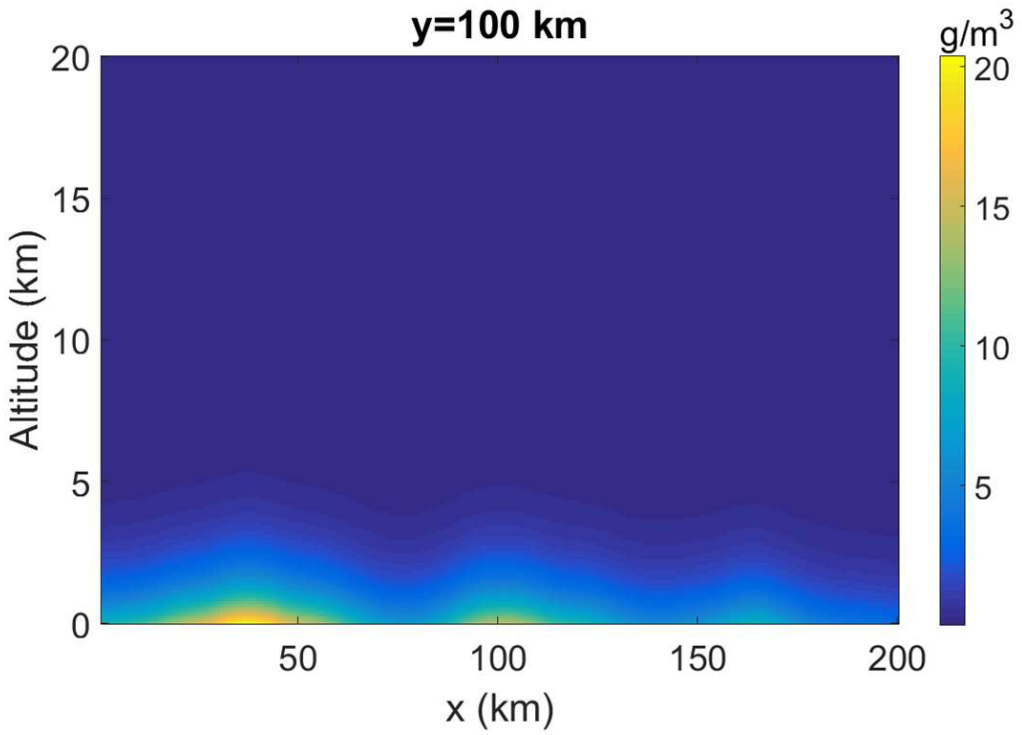

Figure 9.2: *Sample 3-D water vapor field generated with SMOV (water vapor content) — vertical view (y=100 km).*

9.2 Evaluation of the integrated water vapor content and water vapor attenuation

The water vapor density data used in this contribution are derived from the water vapor fields described in Section II, as SMOV fields correctly preserves the horizontal and vertical distribution of V. The simulations were performed by placing the ground-station in the centre of the map (x = 100 km and y = 100 km) and by evaluating the integral in (9.1) for all the 1857 water vapor fields present in the database.

$$V = \int_0^L v(x, y, h) dL \tag{9.1}$$

In (9.1), V is integrated water vapor content in millimetres, v is the water vapor density obtained from the fields (g/m^3) and L is the pathlength across the water vapor field that depends on the elevation angle as well as on the site altitude.

All the simulations were performed for the site of Spino d'Adda, Italy (45.4° N, 9.5° E, altitude 81m a.m.s.l.), which is approximately 25 km from Milano Linate Airport. The water vapor attenuation along the slant path AV (in dB) is then calculated with (9.2).

$$A_V(f) = \widetilde{a}_V(f, V, h_0)V \tag{9.2}$$

where $\widetilde{a}_V$ is the water vapor mass absorption coefficient given in dB/mm, which, in turn, is calculated according to the model presented in [59]; f is the frequency, and h_0 is the altitude of the site.

Based on the data obtained from the simulations we want to evaluate how reliable the cosecant scaling approach is for water vapor attenuation.

9.3 Water vapor scaling

In order to assess the values of V and of A_V for a large range of different elevation angles θ, we performed the simulation described in section 9.2 for θ between 3° and 90° (zenith) with 1Â° step. The simulation for very low elevations (i.e. below 5°), e.g. representative of very high latitude sites such as Svalbard where GEO ground stations are operative, were performed, in these preliminary results, without including the effect of ray bending, which will be implemented in a later stage following the procedure described in [41].

Figure 9.3 shows the CCDF of V for different elevations, as derived using the direct slant path integration in (9.1). As expected, the value of V is highly dependent on the elevation and increases dramatically as θ decreases. This is even clearer in Fig. 9.4, which depicts the same results, but in terms of attenuation for a frequency equal to 19.5 GHz.

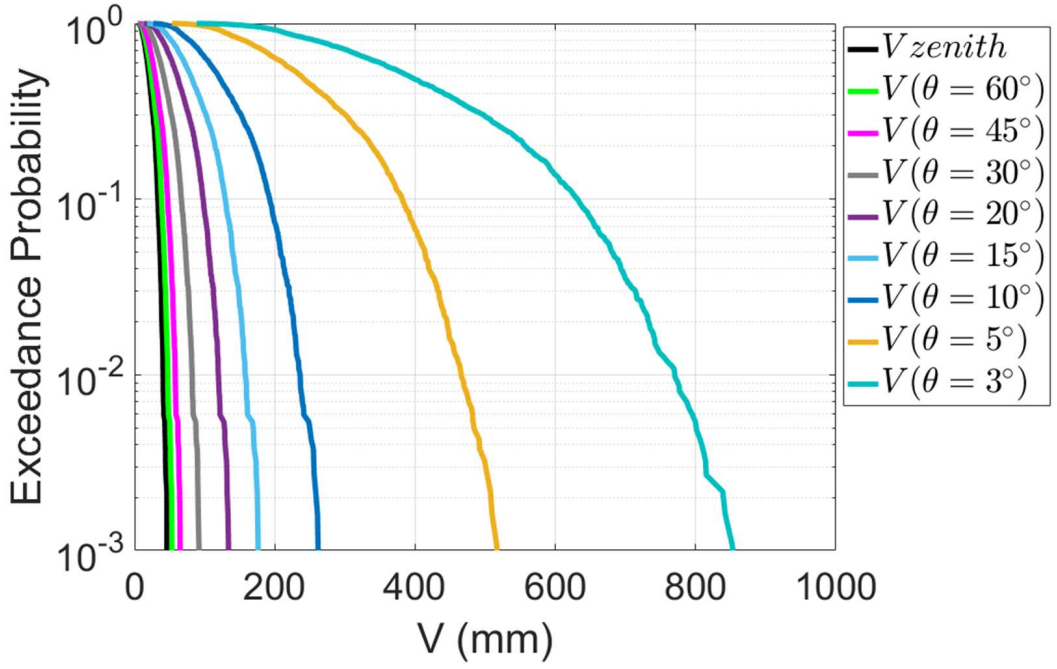

Figure 9.3: *CCDFs of integrated water vapor content for different elevation angles (Spino d'Adda, Italy).*

One of the main objectives of these simulations is to evaluate the accuracy of the simple cosecant scaling approach, which allows to scale the values of V and A_V from the zenith to any elevation angle. The scaling accuracy is again evaluated by using the figure of merit (ϵ) proposed in the ITU-R Recommendation P. 311-15 and expressed in (5.6) and (5.7). The probability levels to which the figure of merit was calculated are the following: [0.5 0.4 0.3 0.2 0.1 0.05 0.03 0.02 0.01 0.005 0.003 0.002 0.001].

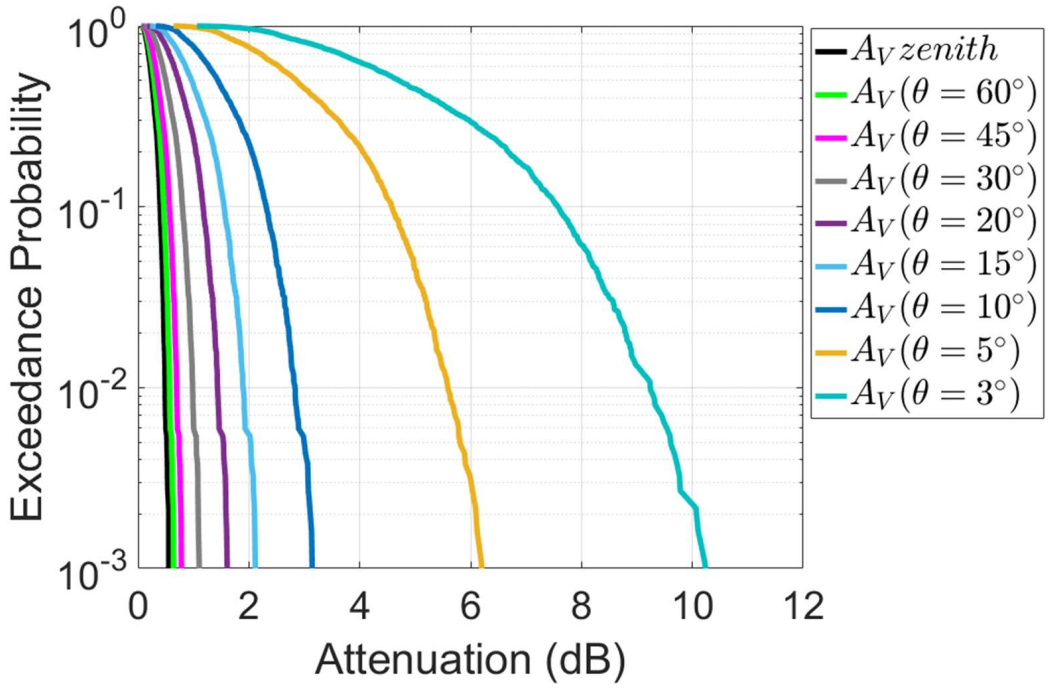

Figure 9.4: *CCDFs of water vapor attenuation for different elevation angles (Spino d'Adda, Italy — frequency 19.5 GHz).*

Figure 9.5 shows the CCDFs of the integrated water vapor content along the slant path obtained for four different elevations and the CCDFs scaled from the Zenith path to the same elevations. It is possible to see that the cosecant scaling shows a good agreement with the simulated results. Figure 9.6 shows the same result in terms of attenuation. In Figure 9.7 we see the plot of the average and the RMS values for the figure of merit ϵ for different elevation angles at the frequency 19.5 GHz.

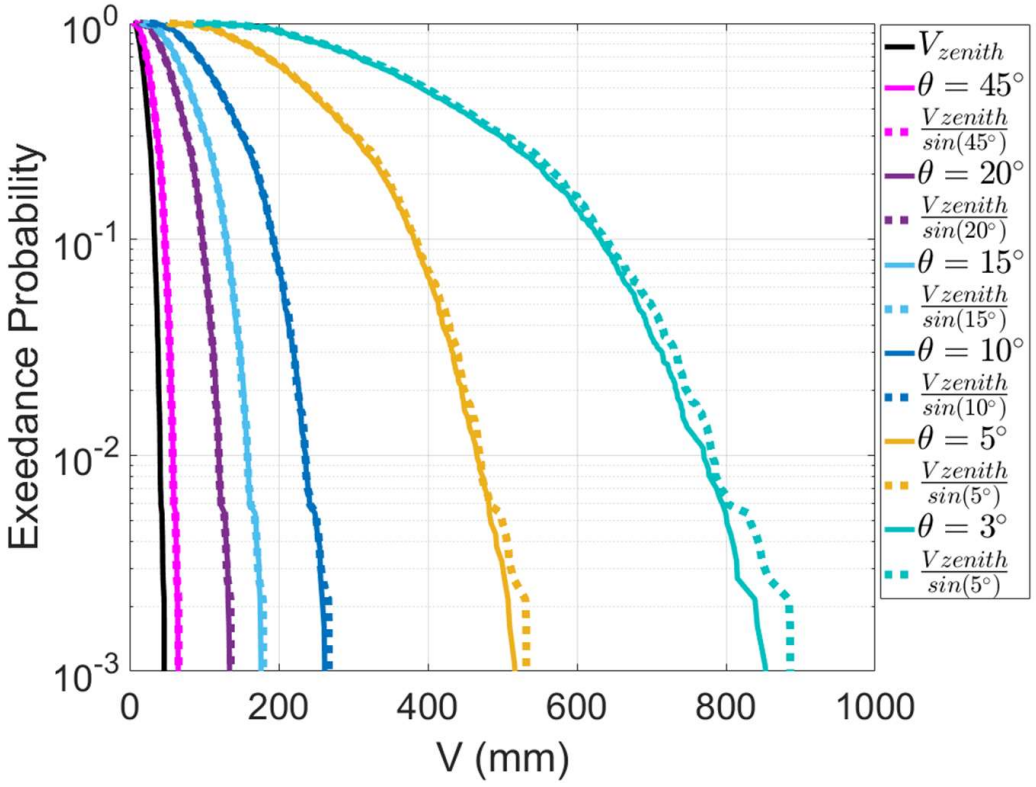

Figure 9.5: *CCDFs of integrated water vapor content scaled by the cosecant of θ (Spino d'Adda, Italy).*

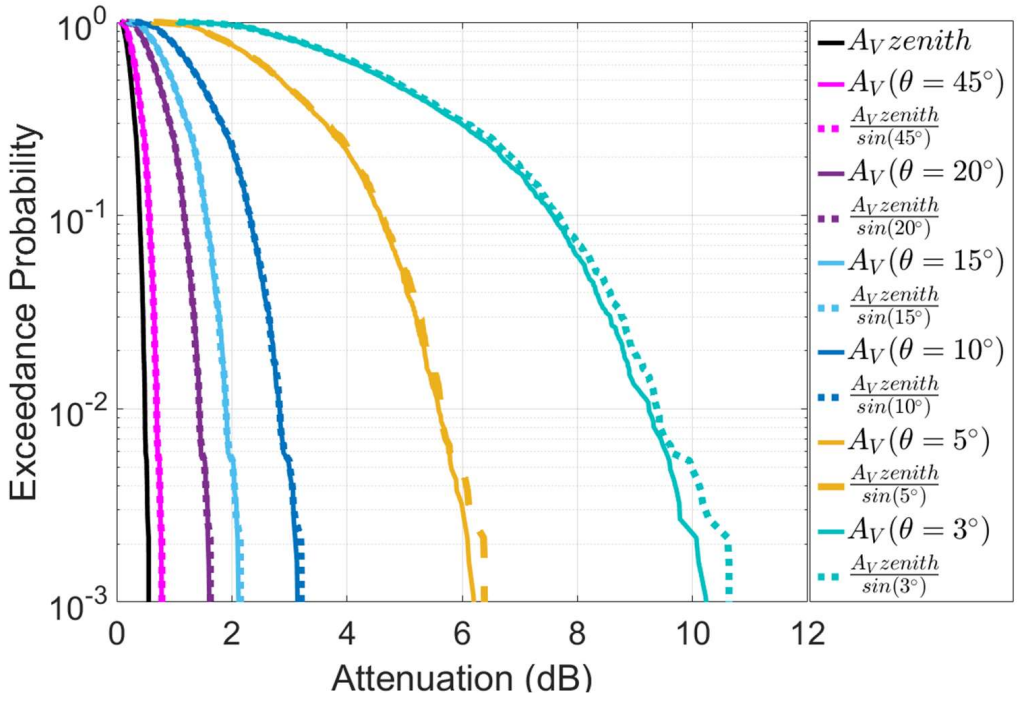

Figure 9.6: *CCDFs of water vapor attenuation scaled by the cosecant of θ (Spino d'Adda, Italy — frequency 19.5 GHz).*

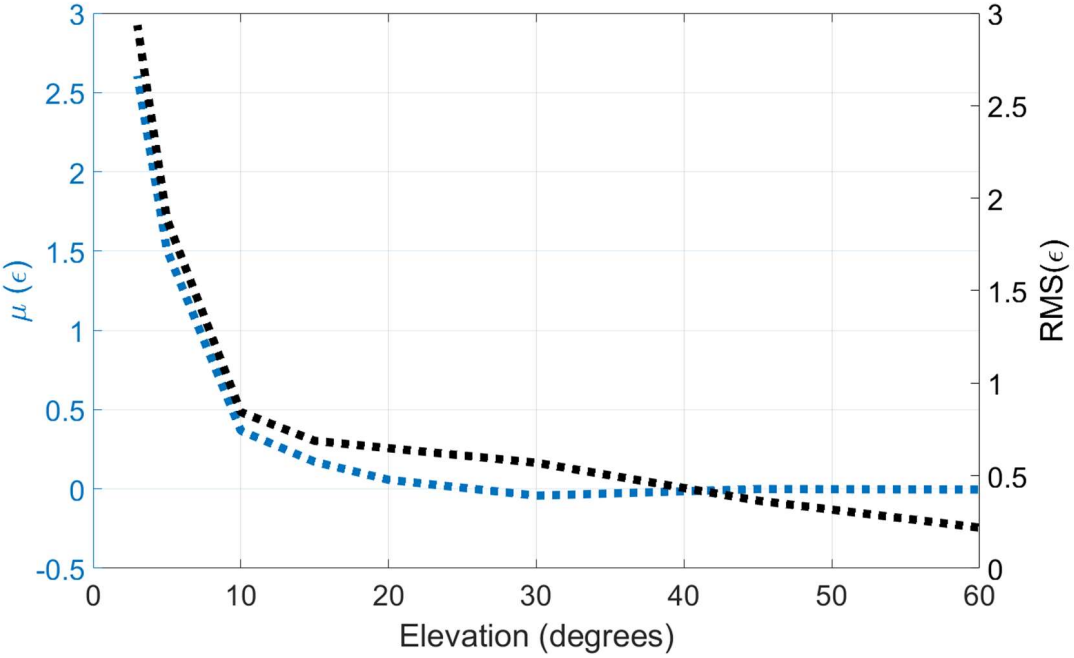

Figure 9.7: *Average and RMS values of the ITU-R figure of merit for the cosecant scaling to different elevations.*

9.4 Cloud fields database

The effect of suspended liquid water in the atmosphere becomes significant above 20 GHz and definitely increases at low elevation angles. Moreover, its contribution is remarkable because of the high occurrence probability of clouds that varies from 40% to 80% of the yearly time in Europe, depending on the site (and latitude). To evaluate the effect of changes of elevation in the clouds attenuation, the solution adopted was to process a database of cloud fields.

The Stochastic Model of Clouds (SMOC) is a methodology able to generate high-resolution 3-D cloud fields. The model extracts its main parameters from fields delivered by the imaging spectroradiometer (MODIS), onboard the LEO Aqua Satellite [60]. The database used in this work consists in 1824 3-D cloud maps of 200 km x 200 km (with 1 km x 1 km of horizontal and 100 m vertical resolution) extension generated for Spino d'Adda. We assumed that the model presented in the subsection 2.1.2.2 is able to generate cloud attenuation time series for the lowest elevation angle considered ($\geq$5°) and then the following model should be used to scale it up according to the elevation angle.

9.5 Clouds attenuation elevation scaling

The modelling procedure was analogous to the one done for rain attenuation and presented in Chapter 7. In the case of cloud maps, the simulations were not performed at all the elevations from between 5° and 90° with 1° step, but only at the following angles: 5°, 10°, 15°, 20°, 30°, 45° and 60°. Again we have define a normalized probability $\underline{P_{0_c}}(\theta)$ that is defined exactly in the same way as in subsection 7.1, i.e., by the normalization of all the CCDFs of cloud attenuation to the one of 5° in such a way $\underline{P_{0_c}}(5°) = 1$ We modelled this probability through the relation expressed in (9.3). Figure 9.8 shows the probabilities obtained by the simulations (dots) and from the equation (9.3) for angles from 5° to 60°.

$$\underline{P_{0_c}}(\theta) = 0.03377[sin(\theta)cosec(\theta)]^{0.7295} + 0.6622 \tag{9.3}$$

Correspondingly, we defined a scaling factor $\varphi_c(\theta, p)$ that depends on the elevation and on the probability. Figure 9.8 shows the values φ_c for different probabilities and elevations. In order to model the scaling factor, we proceeded with a division in two ranges of probabilities, namely, $p < 0.3$ and $0.3 \leq p \leq \underline{P_{0_c}}$. The modelled scaling factor $\hat{\varphi}_c(\theta, p)$ is expressed by the power law relation in (9.4).

$$\hat{\varphi}_c(\theta, p) = a\theta^b + c \tag{9.4}$$

Where the parameters a,b, and c for the two different probability ranges are given in Table 9.1.

For values of p greater than $\underline{P_{0_c}}$, the value of $\hat{\varphi}_c$ is zero.

The procedure that generates the scaled time series is analogous to the one presented for rain in Figure 7.4 and is expressed in (9.5).

$$\hat{A}_{dBclouds}(\theta, n) = A_{dBclouds}(5°, n)[sin(5°)cosec(\theta)]\hat{\varphi}_c(\theta, p) \tag{9.5}$$

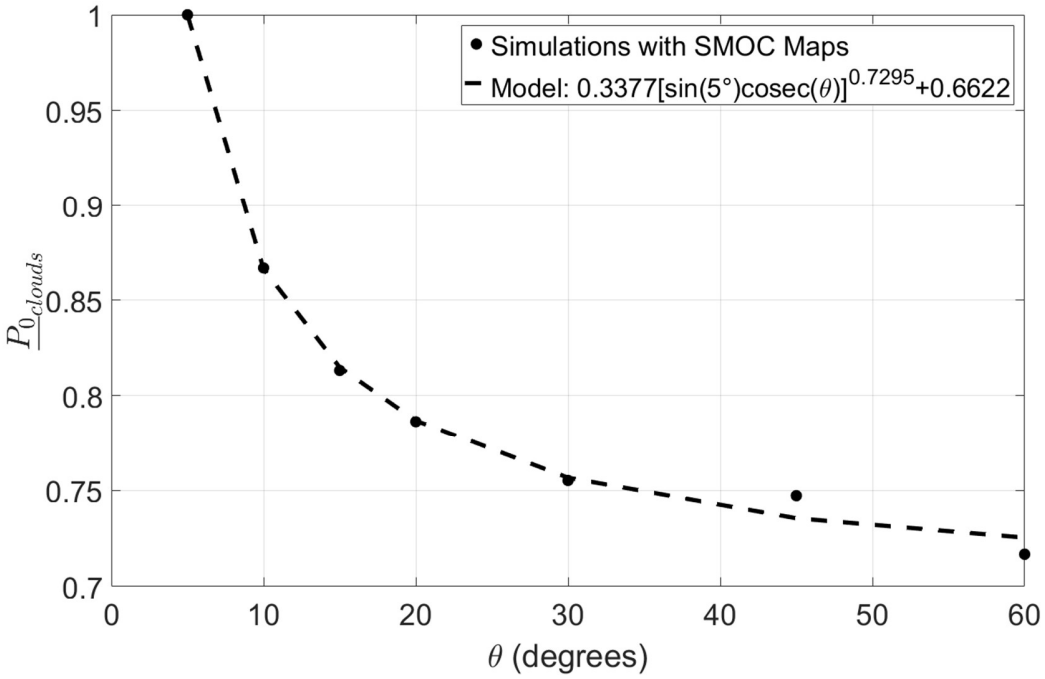

Figure 9.8: *Model of the $\underline{P_0}$ for attenuation due to clouds.*

Table 9.1: *Coefficients for the equation (9.4).*

	$p \leq 0.3$	$0.3 < p < \underline{P_0}_c$
a	$3.129\theta^{-0.4082} - 1.577$	$-0.676\theta^{-0.2348} - 0.3615$
b	$-1.159\theta^{0.1019} + 2.002$	$7532\theta^{-3.889} + 1.701$
c	$0.01415\theta^{0.9228} + 0.9649$	$-2495\theta^{-4.492} + 1.067$

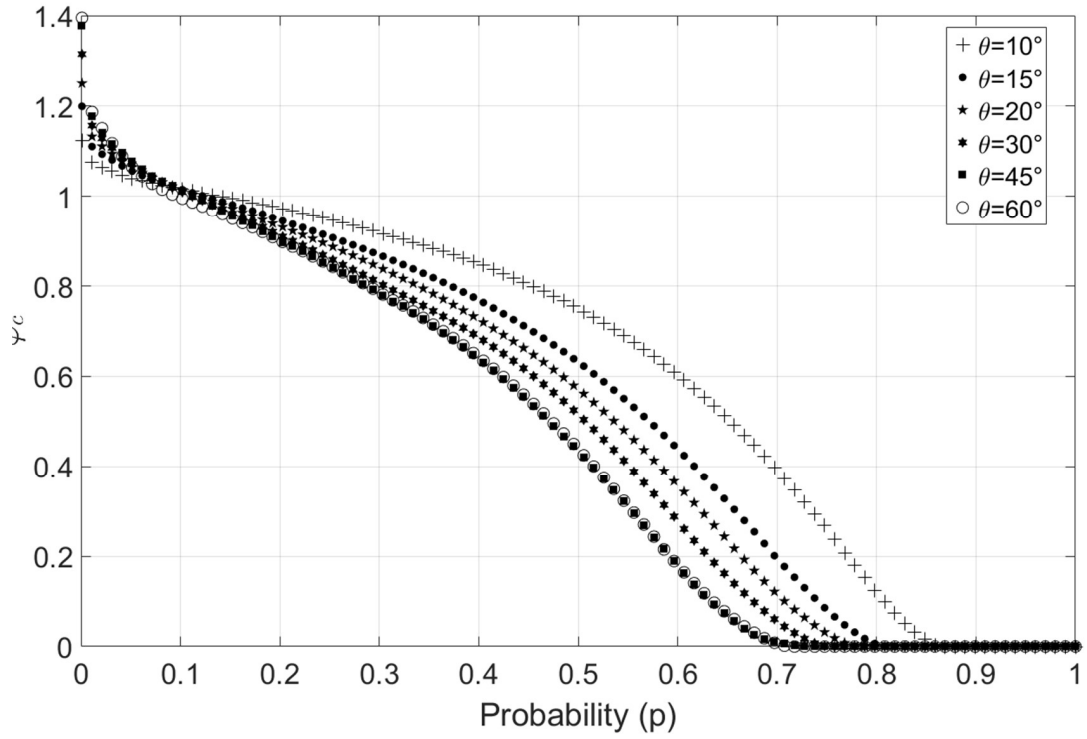

Figure 9.9: *Scaling factor $\varphi_c(\theta, p)$ obtained for different probabilities and elevations.*

9.6 Final Remarks

In this chapter, we presented an analysis of the variations in the water vapor attenuation contribution from very low elevation angles (3°) up to higher ones. In our model, however we start from 5° that is assumed as the minimum elevation considered. The use of the SMOV water vapor fields allowed verifying the feasibility of the cosecant scaling for the long-term water vapor attenuation statistics, and the approach shows a good agreement with the simulations. The results provided a clear insight about the behaviour of the water vapor attenuation when elevation changes. Based on these results we can say that the simple scaling with the cosecant is a fully acceptable solution for a NGEO time series generator of water vapor attenuation.

The accurate knowledge of the gaseous attenuation is of paramount importance in electromagnetic wave propagation experiments (such as the ongoing Aldo Paraboni scientific experiment [61]) to derive total tropospheric attenuation from the beacon signals received by ground stations [62], [63].

The variations in cloud attenuation due to changes in the elevation, in turn, were analysed by using simulations with 3-D cloud fields obtained with the model SMOC. We presented a procedure to scale a time series of cloud attenuation according to the elevation following the same method used for rain in Chapter 7. The analysis on the variations of cloud attenuation with azimuth was not yet attempted, nonetheless, as the probability of clouds occurrence is quite high, we believe that the application of the 180° azimuth window at any passage can be applied to as a first approximation and surely valid at least in terms of long-term statistics.

CHAPTER 10

Application of Model

In this chapter we present some results of the application of the rain ATSS for Miami and Spino d'Adda and describe the procedure for the generation of the total attenuation time series.

10.1 Test scenario specification for the rain ATSS

Since there are no direct and statistically meaningful measurements for NGEO satellite links and aiming to test our model, we performed simulations of a LEO satellite by using MultiEXCELL maps and compared them with the results obtained with the whole procedure described in the previous chapters. These MultiEXCELL LEO satellite simulations used in this chapter work were obtained from [64]. . However, the CCDFs derived by [64] are limited to 90 dB. We have chosen one geosynchronous orbit of the satellite MetOp-A, which orbital parameters are given in Table 10.1 and are derived from the a Two Line Element set (TLE). The sites to which the simulations were performed are Spino d'Adda and Miami, for the reasons we have already mentioned, assuming as minimum elevation 5°. In order to reduce the enormous amount of time required for a complete simulation we used the data of one passage of the satellite and we applied the integration method described in section 4.2. Figure 10.1 and Figure 10.2 shows the elevation ranges during 1-day passage of the selected satellite over Spino d'Adda and over Miami, respectively. The simulations were performed at the carrier frequency of 26.5 GHz that is indicated to be the one for Earth Observation Data Down Link (EODDL).

Table 10.1: *Key parameters of the selected orbit.*

Orbital Parameters	
Semi-major Axis	7195.55
Altitude	817.46
Inclination	98.70
Eccentricity	0.001165
Argument of Perigee	90
Mean Anomaly	90
L Tan	21:30
Orbital repeat Cycle	29

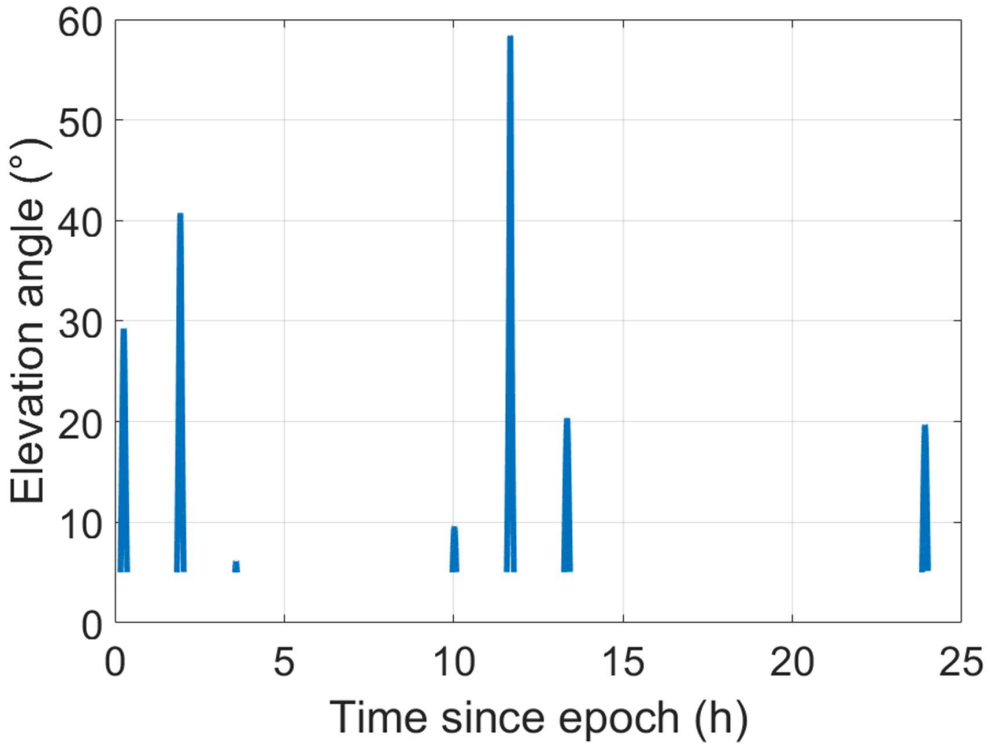

Figure 10.1: *day passage of the chosen satellite over Spino d'Adda.*

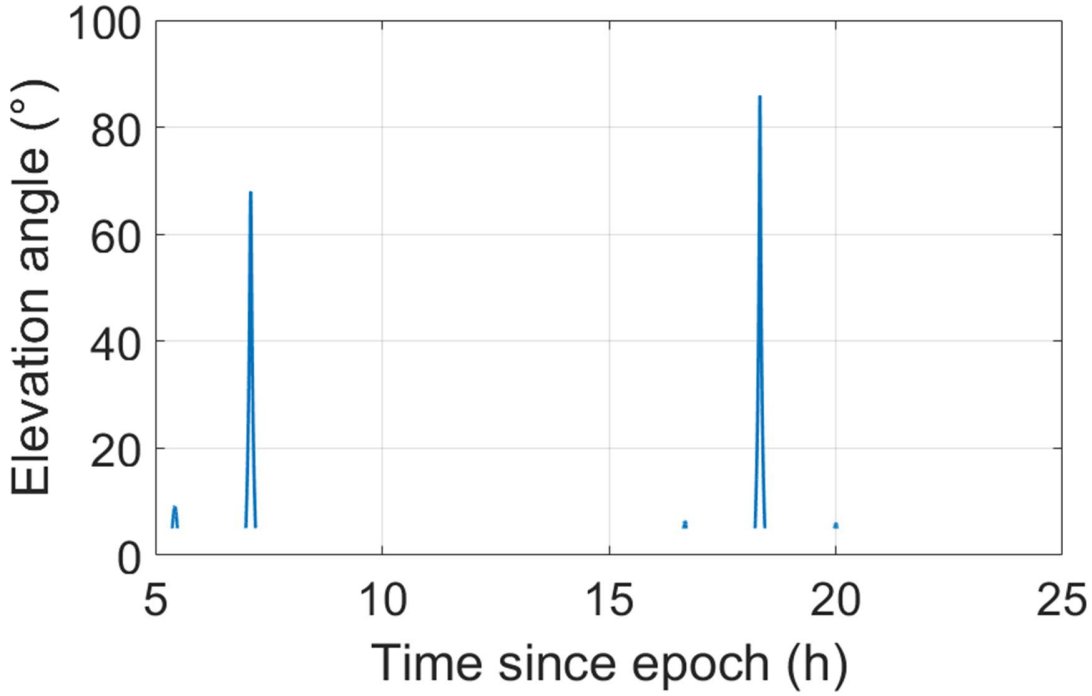

Figure 10.2: *1-day passage of the chosen satellite over Miami.*

10.2 Rain contribution synthesis

10.2.1 Step 1

Generation of the input rain attenuation CCDF for the minimum elevation (5○) — scaled with the procedure described in CHAPTER 5 or obtained from MultiEXCELL.

10.2.2 Step 2

Generation of $A(\theta_{min})$ — the rain attenuation time series for the minimum elevation considered — by means of a proper selection of events inside the ITALSAT database modified (as described in Chapter 6). As explained in the chapter, the procedure consists in the sum of two randomly shifted events from the ITALSAT database obtained at 39.6 GHz and 37.7° elevation. In principle there is no strict need to scale original rain attenuation events to the operational elevation (10° – the angle until which we scale the events using relation between the sines) , but, because of the high elevation (37.7°) the original data refer to, they are unable to cover all the range of attenuations experienced by the NGEO. Furthermore, since in order to have a model that mimics at best what happens in the real situations, the summation of the two events takes into account the cases where the link is crossing more than one rain aggregate at the same time (frequent situation at low elevation angles).

10.2.3 Step 3

The third step consists in scaling up the θ_{min} time series at according to the input orbit parameters of the NGEO satellite using the procedures described in Chapter 7 (Elevation scaling) and Chapter 8 (azimuth window). In order to apply the scaling factor $\hat{\varphi}(p, \theta)$ presented in Chapter 7 to another location like Miami, we multiply all the values of $\hat{\varphi}(p, ,)$ by the relation between the rain height in Miami and the one in Spino d'Adda (reference). The resultant time series must reproduce the statistics of rain attenuation of the NGEO link.

NOTE: Following the detailed analysis carried out on the simulated data, in case there is the need to generate synthetic time series with an even greater similarity to the one of the physical process which take into account also the variations of the rain profile occurring from time to time along the path, we suggest the possibility to add a random variation of the scaling factor within ± 10 % at the rain events provided by the model (which gives only a statistical description). The plus/minus variation must be distributed uniformly among all the event selected in each class of peak attenuation in order to maintain the accuracy of the long-term statistics prediction.

10.3 Results

In this section we present the results obtained by our model and its comparison with the MultiEXCELL simulations. Figure 10.3 shows the CCDF obtained with the proposed ATSS for the selected satellite at Spino d'Adda. The CCDF is normalized to 1, so the zero samples present in the time series were discarded. The result shows a good agreement with MultiEXCELL simulations. The small differences are due to accumulation of the errors present in each step of the model.

In Figure 10.4 is presented the result for Miami. We can notice a larger difference at the lower probabilities (i.e. higher attenuation values). This behaviour could be partly due to the larger range of elevations in Miami (Figure 10.2) and much smaller contact time (i.e. reduced amount of data). Moreover, as mentioned before, the limitation in peak attenuation to 90 dB does not allow to analyse in more detail the full attenuation range. Nonetheless, until the 10^{-1} probability the two CCDFs match very well.

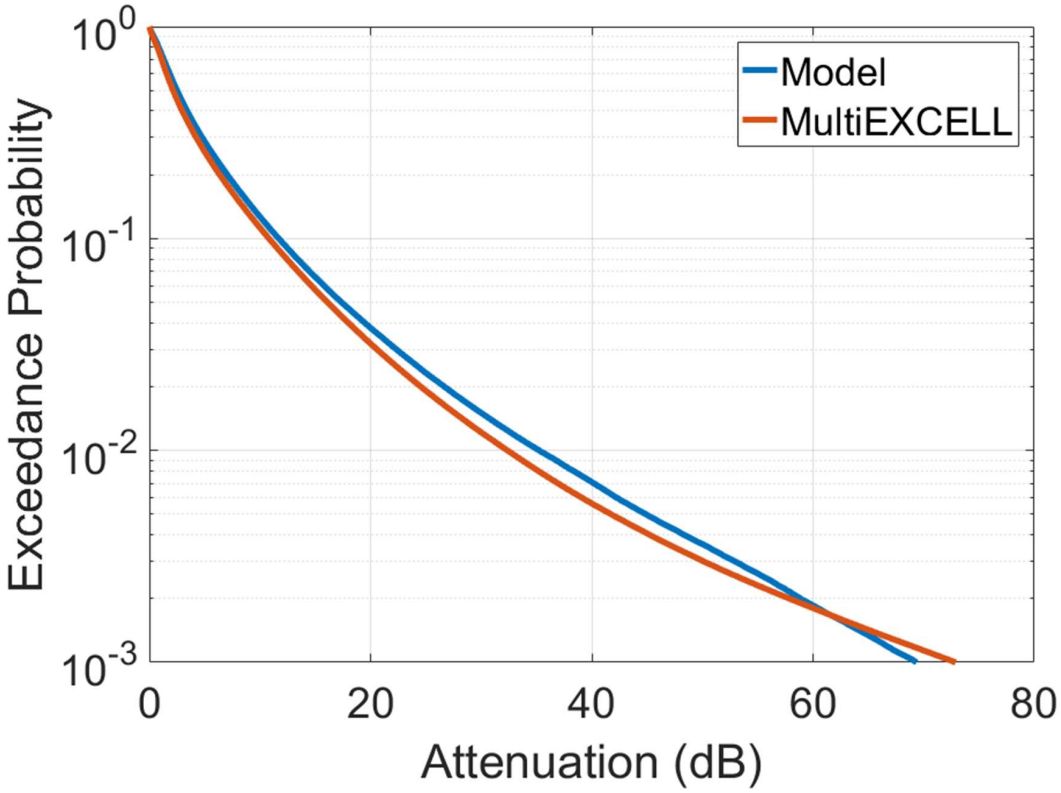

Figure 10.3: *Comparison between the CCDF of rain attenuation obtained with the NGEO ATTS and the one obtained with MultiEXCELL simulations (Spino d'Adda).*

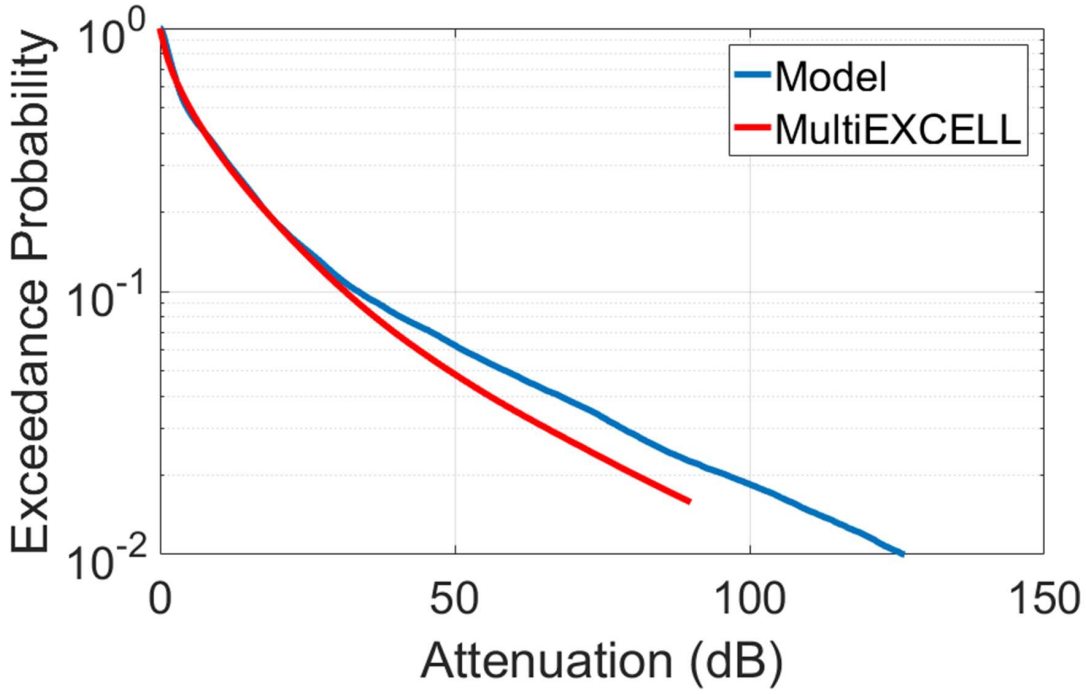

Figure 10.4: *Comparison between the CCDF of rain attenuation obtained with the NGEO ATTS and the one obtained with MultiEXCELL simulations (Miami).*

10.4 Fade slope and fade duration analysis

The quality of an Attenuation Time Series Synthesizer (ATSS) can be evaluated also by considering its performance in reproducing adequately the second order statistics of the rain process, i.e. fade slope and fade duration.

Fade duration (FD) is defined as the time interval between two crossings above the same attenuation threshold. The evaluation of the fade duration is a fundamental aspect since it gives the number and the duration of system unavailability [65]. We evaluated the fade duration statistics of the time series using (10.1).

$$F(A/D) = \frac{N_S(D)}{N_{TOT}} \tag{10.1}$$

Where $N_S(D)$ stands for the total time composed by intervals longer than $D[s]$ in which the Attenuation A [dB] is exceeded and N_{TOT} stands for the total time in which the attenuation exceeds the threshold A. Aiming to quantify in some way the difference between the original ITALSAT database and the modified one, as well as the fade dynamics of the time series generated and scaled in terms of elevation with the procedures previously mentioned, we decide to use the figure of merit presented in [53] that is expressed in (10.2).

$$\epsilon_{FD}(D, A_{th}) = ln\left(\frac{(100 - F_{model}(d > D|a > A_{th})}{100 - F_{original}(d > D|a > A_{th})}\right) \tag{10.2}$$

Where F_{model} is the cumulative exceedance of fade duration obtained with the modified database and the elevation scaling procedure and $F_{original}$ is the cumulative exceedance of fade duration of the original ITALSAT database collect at 37.7° elevation. Figure 10.5 shows the statistics of fade duration for the three beacons (18.7, 39.6, and 49.5 GHz) present in the ITALSAT database for six different attenuation thresholds.

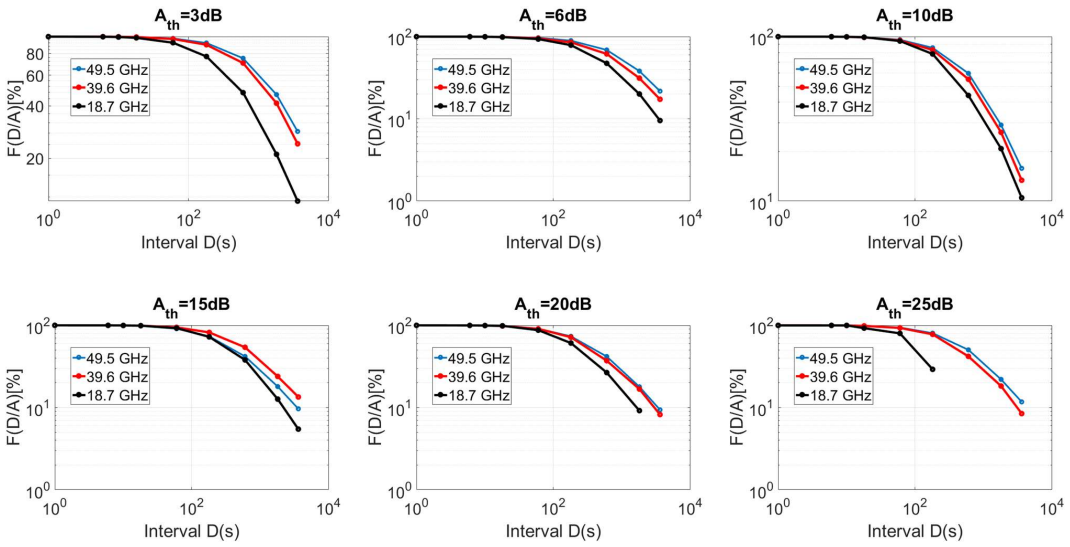

Figure 10.5: *Fade duration CCDF for Spino d'Adda at frequency 18.7 GHz, 39.6 GHz, and 49.5 GHz for 6 attenuation thresholds (3, 6, 10, 15, 20 and 25 dB).*

In order to evaluate the variations in the FD introduced by our procedure we compared the original database obtained at 39.6 GHz (our benchmark, being measured time series) with the FD obtained from a time series generated at 5° and scaled up to 37.7°. The result is shown in Figure 10.6 and the figure of merit (10.2) for the different values of D and A_th is presented in Table 10.2. The results show a good agreement between the two databases, the small differences can be viewed as an effect of the summation procedure.

Fade Slope (FS) in turn is defined as the rate in which the attenuation changes in time. In the design of PIMTs it is important to know the maximum FS of the signal in the receiver in order to define the minimum required tracking speed and also to predict the short-term propagation conditions [65]. For a fixed link, FS depends on the type of rain (stratiform or convective), wind speed, and attenuation level. However, FS is not dependent on the carrier frequency [66].

Mathematically, the FS statistics are defined as the probability P($|\zeta|/A_{th}$) of the absolute value of a fade slope ζ exceeds a given attenuation threshold. In Figure 10.7 are reported the statistics of FS for the ITALSAT database for the different beacon frequencies and four attenuation thresholds (1, 3, 5, 15, and 20 dB). The comparison between the statistics of FS of our model and the original ITALSAT database was done according to the figure of merit in (10.3). The results are reported in Figure 10.8 and Table 10.3. It is possible to notice that the variation in the FS slope introduced by the procedure of sum of two events is not entirely eliminated by the procedure of scaling up the time series, especially at the low probability levels. This happens due to the

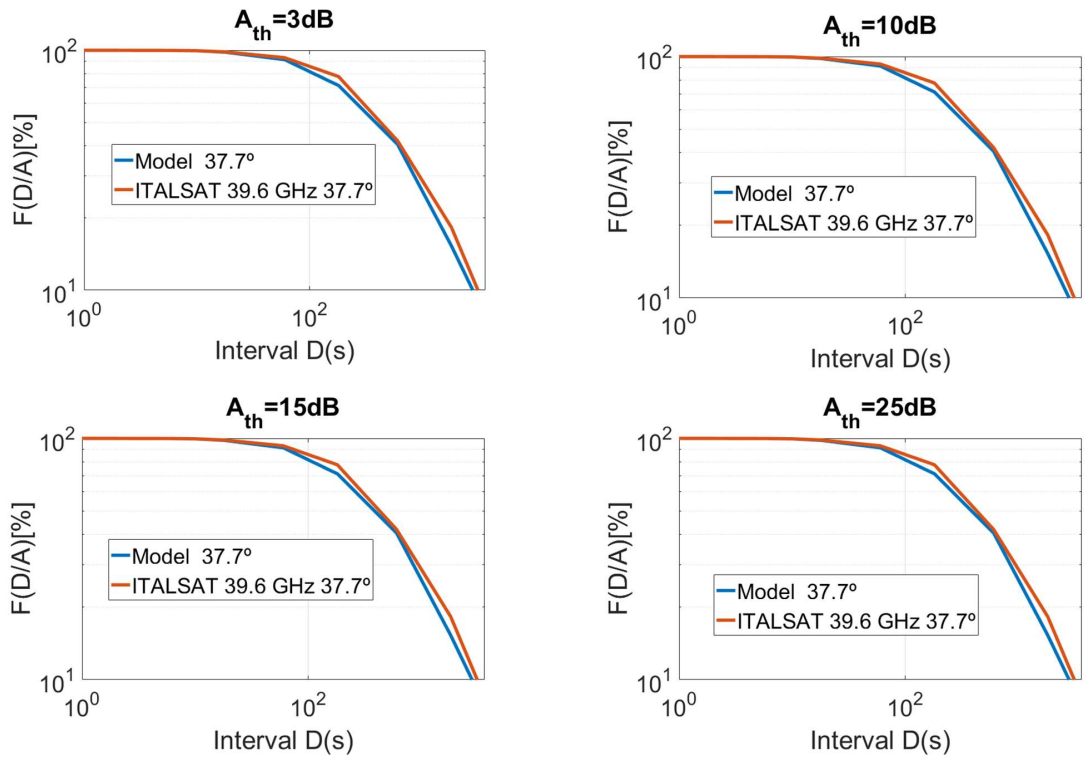

Figure 10.6: *Comparison between the fade duration of the ITALSAT original and the one of the time series obtained from our model (both at 37.7° and 39.6 GHz) for different attenuation thresholds.*

increasing of the slope when two points of the time series with a significant slope are summed up together. Then, above this threshold there are no events in the database.

$$\epsilon_{FS}(\zeta, A_{th}) = 2\left(\frac{P_{model}(|\zeta|/A_{th}) - P_{original}(|\zeta|/A_{th})}{P_{model}(|\zeta|/A_{th}) + P_{original}(|\zeta|/A_{th})}\right) \tag{10.3}$$

Table 10.2: $\epsilon_{FD}(D, A_{th})$ *for the comparison between the ITALSAT database at 39.6 GHz collected at 37.7° and the time series generated for 5° and scaled up to 37.7° with the procedures described previously.*

	$A_{th} = 3dB$	$A_{th} = 5dB$	$A_{th} = 10dB$	$A_{th} = 15dB$	$A_{th} = 20dB$	$A_{th} = 25dB$
$D = 6s$	-0.0880	0.2567	-0.3649	-0.4103	-0.8271	0.0195
$D = 10s$	0.0347	0.3737	-0.4234	-0.4022	-0.8216	-0.0562
$D = 18s$	0.0450	0.2906	-0.2787	-0.2023	-0.5094	0.1626
$D = 60s$	-0.0040	0.1911	-0.1876	-0.3672	-0.5163	0.2227
$D = 180s$	-0.0404	0.2223	-0.1186	-0.1705	-0.2789	0.2530
$D = 600s$	-0.0146	0.2112	-0.0598	-0.0449	-0.1510	0.0240
$D = 1800s$	0.0105	0.1101	-0.0033	-0.0271	-0.0364	-0.0022
$D = 3600s$	0.0257	0.0451	-0.0111	0.0042	-0.0222	-0.0014
μ_ϵ	**-0.0039**	**0.2126**	**-0.1809**	**-0.2025**	**-0.3954**	**0.0836**
$\sigma_\in$	**0.0019**	**0.0104**	**0.0259**	**0.0299**	**0.1053**	**0.0128**
$r.m.s = (\mu_\epsilon^2 + \sigma_\epsilon^2)$	**0.0043**	**0.2129**	**0.1828**	**0.2047**	**0.4092**	**0.0845**

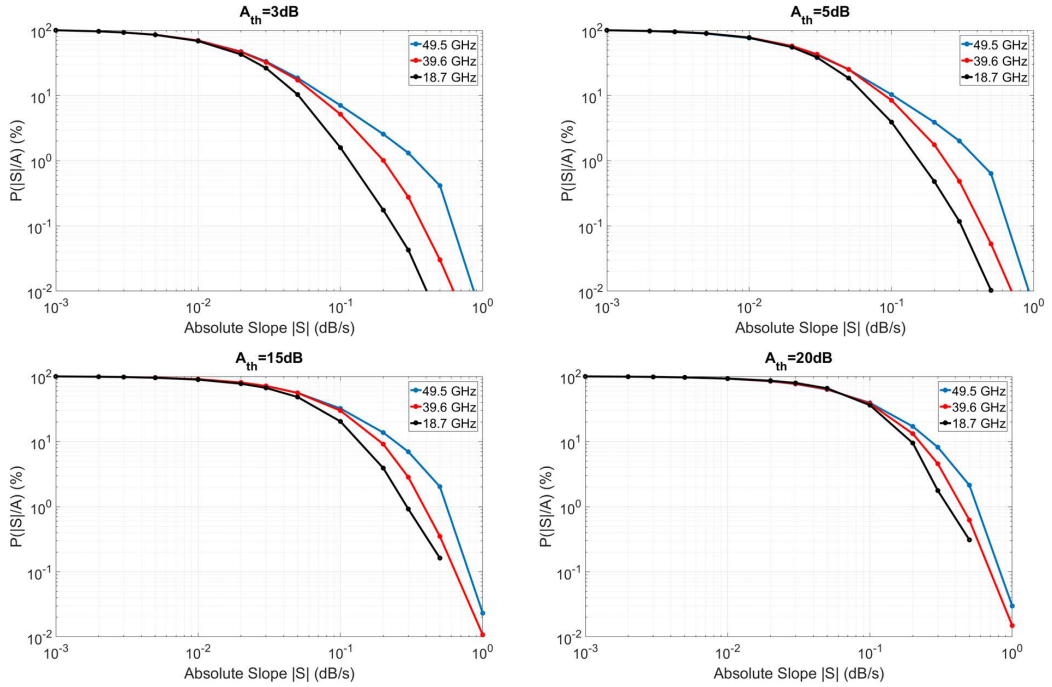

Figure 10.7: *Fade slope CCDF for Spino d'Adda at 18.7, 39.6 and 49.5 GHz and elevation 37.7° for 4 attenuation thresholds (3, 5, and 15 dB).*

10.5 Clouds, water vapor, and oxygen contribution synthesis

As mentioned in previous chapters, the models for both water vapor and clouds attenuations that we considered, for our total attenuation time series synthetizer are derived from a previous PhD study at Politecnico di Milano [11]. We have developed the techniques to scale in elevation both the CCDF and the time series generated with the method proposed in [11] according to the cosecant law for water vapour (section 9.3) and according to the procedure in section in 9.5 for clouds. In this section we are going to detail the rationality behinds the clouds and water vapor ATSS in [11].

The procedure takes as input the long-term statistics of ILWC and IWVC of the selected site (which can be obtained from derived from models, like SMOC and SMOV, and also from the ITU-R Recommendations) and if necessary at 5°. Afterwards, It consists basically in reproducing the long-term statistics (objective function) with a proper selection of daily time series present in the radiometer measurements database described in section 2.1.2.2 and then converted in water vapour and liquid water attenuation.

As explained before, the database of water vapour and cloud attenuation is divided in fixed frames of daily time series, thus maintaining the synchronous variation between the two quantities since it was observed an annual trend of the minimum and maximum values of IWVC, as well as of the daily average and of the peak value of ILWC. As it was done for rain, this database is divided in classes (8 for ILWC and 5 for IWVC) according to the peak value of each quantity. The time series necessary to reproduce the 5° CCDFs of ILWC and IWVC of the selected site are then obtained by a scaling of these daily frames in terms of elevation (using the inverse of the scaling factor presented in section 9.5 for clouds and the cosecant scaling for water vapor) and a selection of frames by means of a joint optimization (in order to maintain the water vapour and cloud correlation) that reproduces the long-term statistics. The optimization selects the time series of the same days that satisfy simultaneously the request to match both the ILWC and IWVC long-term statistics. The values of IWVC and ILWC are then converted to attenuation using the mass absorption coefficients given in [41] and [40].

Since oxygen attenuation has small temporal variations it is assumed to be constant as a background effect and scaled only geometrically with the elevation.

The model in [11]] was already validated for both long and short-term statistics and in different sites; as a consequence, we assumed here that the applications the scaling models developed in this work should deliver good results when applied to these water vapour, clouds and oxygen time series as we have demonstrated for rain.

Figure 10.8 and Figure 10.9 shows, respectively, the CCDFs obtained from the time series of IWVC and ILWC obtained according to the procedure described above applied to the test scenario described in section 10.1. The CCDFs of water vapor and clouds attenuation are given in 10.10

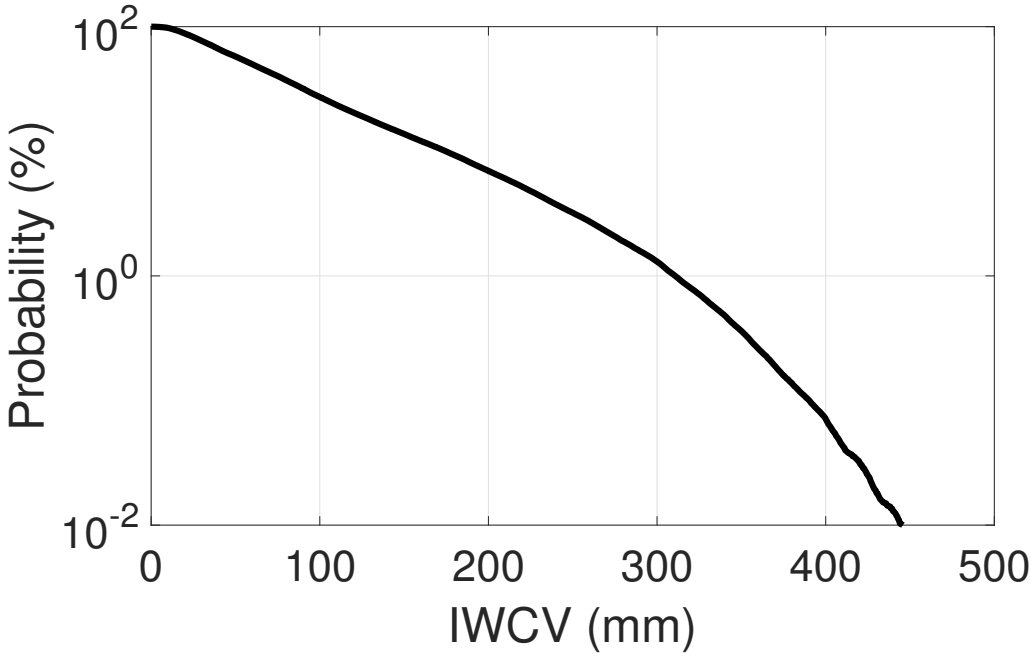

Figure 10.8: *CCDF of IWVC obtained for the test scenario described in section 10.1.*

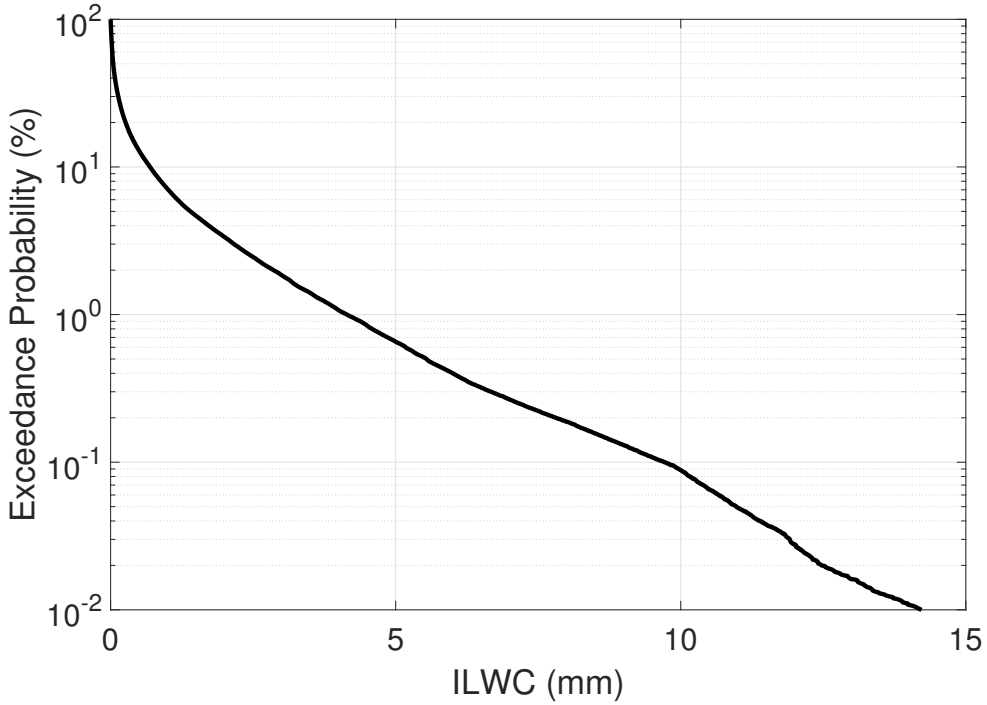

Figure 10.9: *CCDF of ILWC obtained for the test scenario described in section 10.1.*

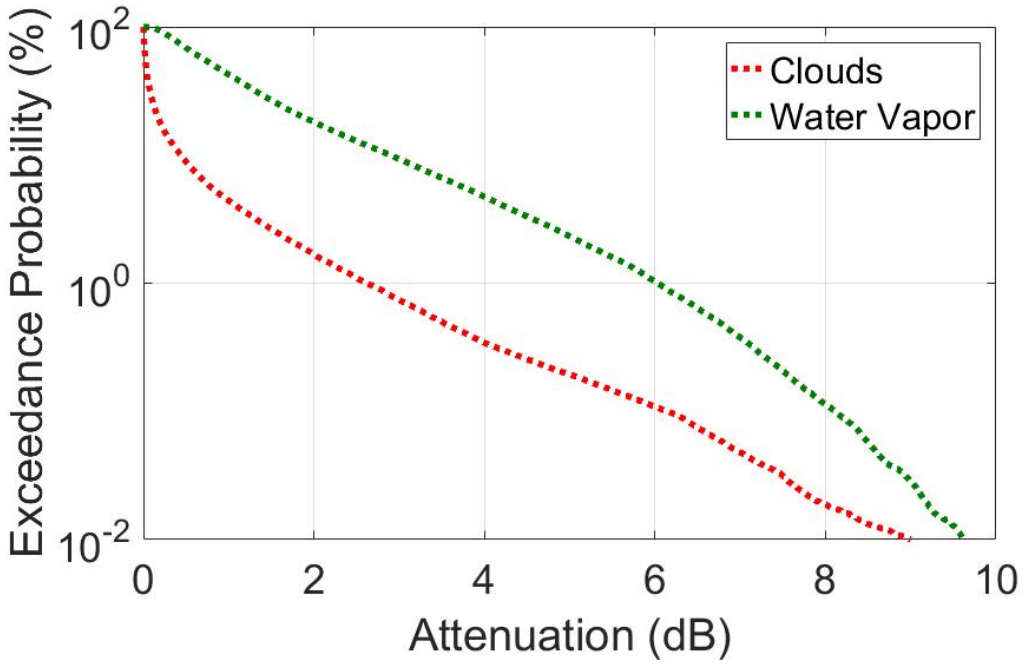

Figure 10.10: *CCDFs of attenuation due to clouds and water vapor obtained for the test scenario described in section 10.1.*

10.6 Total attenuation time series synthesis

The composition of the total attenuation time series is carried out by properly summing up the different contributions described in the previous sections. Oxygen is considered constant and its value retrieved from radiosounding measurements or, in absence of these measurements, from the procedure described in [41] and [42], and then scaled according to the elevation angle with the cosecant law.

It follows the composition of rain and cloud attenuation events. This is done with the assumption that a rain event must occur only in presence of clouds.

The time series of clouds attenuation are then considered as "the master variable in the overlapping of rain attenuation events" [13]. The classification of the rainy and non-rainy clouds is done with the Cloud Type Algorithm (CTA) cited in [13] and when a cloud is classified as rainy, a rain attenuation event is superimposed to the clear sky components.

The CTA was formulated from the analysis of the data available in the two databases mentioned before (radiometers and radiosonde observations). The basic idea behinds CTA is that is possible to apply thresholds to identify and catalogue the intervals present in the ILWC time series of the databases. The CTA classifies the intervals of ILWC in four Cloud Types (CT) [CT1, CT2, CT3, and CT4]. The analysis shows that rain events occurs in general in intervals classified as CT3 or CT4. So, the superimposition of the rain events is more likely to occur in these intervals. For a most detailed explanation on the CTA we refer the reader to the Appendix A of [11]. With this procedure, it is possible to generate a time series of rain attenuation well concatenated with the one of clouds (and corresponding water vapour).

The total attenuation time series is then composed by the superposition, on a 1 sec. sample basis, of clear sky and rain attenuation according to the overlapping procedure described above. In Figure 10.11 we show a result for the satellite link scenario described in section 10.1.The result shows the components of rain, water vapor, and clouds attenuation, separated and summed up together. Due to the lack of measurements or correlated total time series attenuation we are not able at the present moment to validate the complete model as we have done for rain.

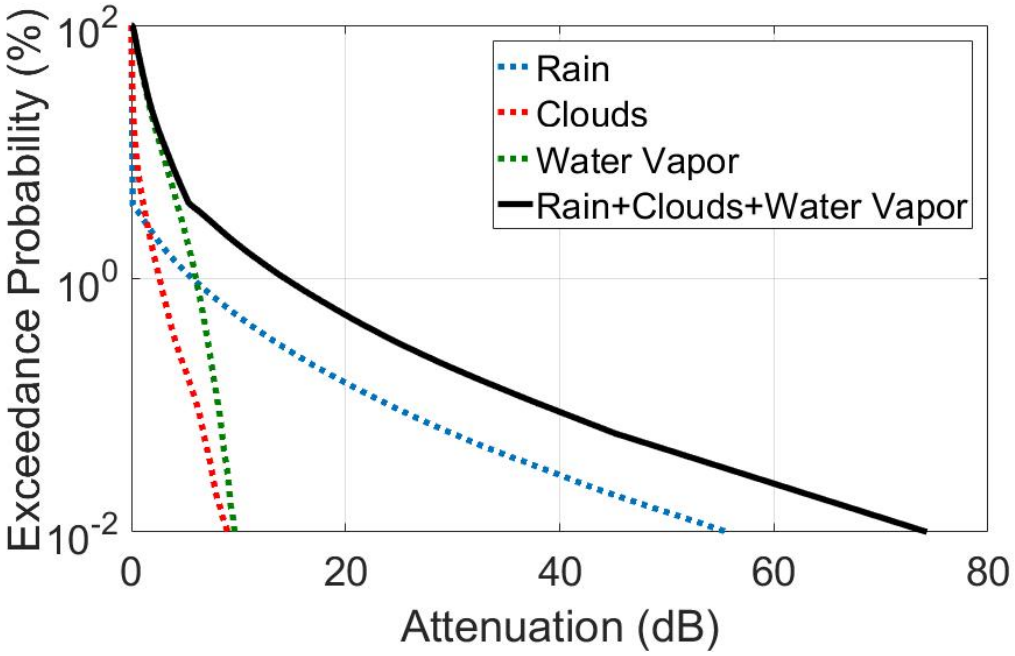

Figure 10.11: *CCDF of the different components and the total attenuation (except oxygen) obtained for the test scenario described in section 10.1.*

CHAPTER 11

Conclusions and Future Works

We presented in this thesis a model of a total attenuation time series synthesizer of tropospheric attenuation for NGEO satellite systems able to reproduce the statistics of the different impairments (rain, clouds, water vapour and oxygen) taking into account the variations of azimuth and elevation that occurs during the NGEO satellite passage.

The modelling procedure relied on data obtained by simulations using field maps generated with MultiEXCELL (rain), SMOV (vapor), and SMOC (clouds) models, as well as on the long-term ITALSAT database. The use of these databases of measurements (even in a modified form) provides a realistic approach to the modelling with a strong physical basis.

First, we presented a procedure for scaling the long-term statistics of rain attenuation down to very low elevation angles. The CCDF scaled to the lowest elevation in the orbit (5° in our case) is the main input to our procedure that generates time series of rain attenuation for a NGEO satellite, consisting in:

- the generation of a rain attenuation time series for a GEO satellite at the minimum elevation — this is done by means of a proper selection among events of the ITALSAT long-term measurements database modified in order to mimic the situations that occur at low elevation angles;

- scaling up these time series to each of the elevation angles present in the orbit.

Since in the NGEO satellite systems, together with the elevation changes, there are also azimuthal changes, we proposed a model to account for the azimuthal variations. The rain attenuation time series synthesizer is then completed with the generation of an azimuth window that considers the effects of these variations during each passage of the satellite.

We presented also a study on the feasibility of the cosecant scaling applied to the water vapor attenuation and, since in comparison to the rain structures, the water vapor results well uniform, we decided to adopt only the geometrical scaling for water vapor. For the cloud's contribution, in turn, we derived a scaling factor for scaling up the elevation with a procedure analogous to the one used to rain. In the last chapter, we showed some simulations using the rain ATSS for two sites (Spino d'Adda and Miami) with very different rain patterns and the results show a good agreement with the simulations based in MultiEXCELL maps for both sites for a LEO satellite.

Further refinements of the ATSS here proposed are:

- More refined analysis to determine the most suitable way to sum up two rain episodes (if any).
- Comparisons of the model with the results of other ATSSs and also (if possible) with measurements in different sites in order to check its worldwide validity. The reference [67] presents some results that can be used for a comparison.
- Study of the azimuthal variations of clouds attenuation, an aspect that we have neglected in this work since the time of simulations for several azimuths along the cloud maps would be almost unmanageable.
- Introduction of a model and procedure for the generation of the scintillation components and their variations with elevation together with the proper way to add them to clouds and rain events (joint occurrence). In this respect, reference could be made to [68],
- Capacity calculations can be implemented for different LEO/MEO scenarios following the method proposed in [69],
- Extension of the model for the the evaluation of site/orbital diversity scenarios [70].

Bibliography

[1] Arthur C. Clarke. Extra-terrestrial relays. *Wireless World*, 51:14–+, 04 1945.

[2] A.K. Maini and V. Agrawal. *Satellite Technology: Principles and Applications*. Wiley, 2010.

[3] M.O. Kolawole. *Satellite Communication Engineering*. CRC Press, 2016.

[4] Sastri L. Kota, Kaveh Pahlavan, and Pentti A. Leppanen. *Broadband Satellite Communications for Internet Access*. Kluwer Academic Publishers, Norwell, MA, USA, 2004.

[5] J.E. Allnutt. *Satellite-to-Ground Radiowave Propagation*. IET electromagnetic waves series. Institution of Engineering and Technology, 2011.

[6] SatBeams. https://www.satbeams.com/satellites?status=active.

[7] Joseph N. Pelton, Scott Madry, and Sergio Camacho-Lara. *Handbook of Satellite Applications*. Springer Publishing Company, Incorporated, 2012.

[8] SES Networks. Engineering freedom: Redefining network services with o3b mpower - insight paper. Technical report, ITU-R, 2012.

[9] S.C. Pascall and D.J. Withers. *Commercial Satellite Communication*. Communication technology. Focal Press, 1997.

[10] L. J. Ippolito. Radio propagation for space communications systems. *Proceedings of the IEEE*, 69(6):697–727, June 1981.

[11] Laura Resteghini. *A time series synthesizer of tropospheric impairments affecting satellite links developed in the framework of the Alphasat experiment*. PhD thesis, Politecnico di Milano, Dipartimento di Elettronica e Informazione, 2014. Supervisor: Carlo Capsoni.

[12] Louis J. Ippolito and United States. *Propagation effects handbook for satellite systems design [microform] : a summary of propagation impairments on 10 to 100 GHz satellite links with techniques for system design / Louis J. Ippolito*. National Aeronautics and Space Administration, Scientific and Technical Information Division [Washington, DC], 4th ed. edition, 1989.

[13] A. D. Panagopoulos, P. M. Arapoglou, and P. G. Cottis. Satellite communications at ku, ka, and v bands: Propagation impairments and mitigation techniques. *IEEE Communications Surveys Tutorials*, 6(3):2–14, Third 2004.

[14] W. Liu and D. G. Michelson. Fade slope analysis of ka-band earth-leo satellite links using a synthetic rain field model. *IEEE Transactions on Vehicular Technology*, 58(8):4013–4022, Oct 2009.

[15] E. E. Altshuler, V. J. Falcone, and K. N. Wulfsberg. Atmospheric effects on propagation at millimeter wavelengths. *IEEE Spectrum*, 5(7):83–90, July 1968.

[16] L. Luini and A. Quadri. Investigation and modeling of ice clouds affecting earth-space communication systems. *IEEE Transactions on Antennas and Propagation*, 66(1):360–367, Jan 2018.

[17] H. G. Booker and W. E. Gordon. A theory of radio scattering in the troposphere. *Proceedings of the IRE*, 38(4):401–412, April 1950.

[18] ITU-R Recommendation P.618-13. Propagation data and prediction methods required for the design of earth-space telecommunication systems. Technical report, ITU-R, 2017.

[19] C. Pereira, D. Vanhoenacker-Janvier, N. Jeannin, L. Castanet, and A. Martellucci. Simulation of tropospheric scintillation on leo satellite link based on space-time channel modeling. In *The 8th European Conference on Antennas and Propagation (EuCAP 2014)*, pages 3516–3519, April 2014.

[20] P. Dvorak and C. Capsoni. Model for synthesis of short-term tropospheric amplitude scintillation. In *2016 10th European Conference on Antennas and Propagation (EuCAP)*, pages 1–4, April 2016.

[21] C Capsoni, Aldo Paraboni, Carlo Riva, Emilio Matricciani, L Luini, Gennaro Gallinaro, Gatti Nicola, and Juan Rivera Castro. Verification of propagation impairment mitigation techniques. In *15th Ka and BroadBand Communications, Navigation and Earth Observation Conference*, 2009.

[22] G. Carrie, L. Castanet, and F. Lacoste. Validation of rain attenuation time series synthesizers for temperate area - on the enhanced maseng-bakken model. In *2008 IEEE International Workshop on Satellite and Space Communications*, pages 40–44, Oct 2008.

[23] Stefano Bertorelli. *Analysis of the tropospheric radio channel behavior for the project of satellite systems based on the principle of shared resource*. PhD thesis, Politecnico di Milano, Dipartimento di Elettronica e Informazione, 2006. Supervisor: Aldo Paraboni.

[24] L. Luini and C. Capsoni. Preliminary results from a physically-based methodology for the evaluation of a time diversity system. In *Proceedings of the 5th European Conference on Antennas and Propagation (EUCAP)*, pages 1600–1604, April 2011.

[25] F. P. Fontan, A. Abele, B. Montenegro, F. Lacoste, V. Fabbro, L. Castanet, B. Sanmartin, and P. Valtr. Modelling of the land mobile satellite channel using a virtual city approach. In *The Second European Conference on Antennas and Propagation, EuCAP 2007*, pages 1–7, Nov 2007.

[26] T. Maseng and P. Bakken. A stochastic dynamic model of rain attenuation. *IEEE Transactions on Communications*, 29(5):660–669, May 1981.

[27] ITU-R Recommendation P.1853-1. Tropospheric attenuation time series synthesis. Technical report, ITU-R, 2012.

[28] B. C. Gremont and M. Filip. Spatio-temporal rain attenuation model for application to fade mitigation techniques. *IEEE Transactions on Antennas and Propagation*, 52(5):1245–1256, May 2004.

[29] Max van de Kamp. Short-term prediction of rain attenuation using two samples. *Electronics Letters*, 38:1476 – 1477, 12 2002.

[30] U. . Fiebig. Modeling rain fading in satellite communications links. In *Gateway to 21st Century Communications Village. VTC 1999-Fall. IEEE VTS 50th Vehicular Technology Conference (Cat. No.99CH36324)*, volume 3, pages 1422–1426 vol.3, Sep. 1999.

[31] Frederic Lacoste, Michel Bousquet, Frederic Cornet, Laurent Castanet, and Joel Lemorton. Classical and on-demand rain attenuation time series synthesis: Principle and applications. In *24th AIAA International Communications Satellite Systems Conference*, 06 2006.

[32] R. J. Watson, A. Page, and P. A. Watson. Time-series of attenuation on ehf and shf fixed satellite links derived from meteorological and forecast data. In *IEE Seminar on Personal Broadband Satellite (Ref. No. 2002/059)*, pages 4/1–4/4, Jan 2002.

[33] D. D. Hodges, R. J. Watson, and G. Wyman. An attenuation time series model for propagation forecasting. *IEEE Transactions on Antennas and Propagation*, 54(6):1726–1733, June 2006.

[34] R. Nebuloni, C. Capsoni, and M. Luccini. Advanced time series synthesizer for simulation of joint rain attenuation conditions. *Radio Science*, 49(9):699–708, Sep. 2014.

[35] S. Bertorelli, C. Riva, and L. Valbonesi. Generation of attenuation time series for simulation purposes starting from italsat measurements. *IEEE Transactions on Antennas and Propagation*, 56(4):1094–1102, April 2008.

[36] E. Matricciani. Physical-mathematical model of the dynamics of rain attenuation based on rain rate time series and a two-layer vertical structure of precipitation. *Radio Science*, 31(02):281–295, March 1996.

[37] L. Xu, X. Shen, D. D. Huang, X. Feng, and W. Wang. Tomographic reconstruction of rainfall fields using satellite communication links. In *2017 23rd Asia-Pacific Conference on Communications (APCC)*, pages 1–5, Dec 2017.

[38] C. Kourogiorgas and A. D. Panagopoulos. A rain-attenuation stochastic dynamic model for leo satellite systems above 10 ghz. *IEEE Transactions on Vehicular Technology*, 64(2):829–834, Feb 2015.

[39] C. I. Kourogiorgas, A. D. Panagopoulos, J. D. Kanellopoulos, and P. M. Arapoglou. Rain attenuation time series synthesizer for leo satellite systems operating at ka band. In *2012 6th Advanced Satellite Multimedia Systems Conference (ASMS) and 12th Signal Processing for Space Communications Workshop (SPSC)*, pages 119–123, Sep. 2012.

[40] ITU-R. Recommendation p.840-8: Attenuation due to clouds and fog. Technical report, ITU-R, 2019.

[41] ITU-R. Recommendation itu-r p.676-11: Attenuation by atmospheric gases. Technical report, ITU-R, 2016.

[42] ITU-R. Recommendation p.1510-1: Mean surface temperature. Technical report, ITU-R, 2017.

[43] L. Luini, C. Capsoni, and R. Nebuloni. Free space optics to enable high data rate download from leo satellites: The impact of clouds. In *2014 3rd International Workshop in Optical Wireless Communications (IWOW)*, pages 35–39, Sep. 2014.

[44] L. Luini and C. Capsoni. Multiexcell: A new rain field model for propagation applications. *IEEE Transactions on Antennas and Propagation*, 59(11):4286–4300, Nov 2011.

[45] L. Luini and C. Capsoni. A rain cell model for the simulation and performance evaluation of site diversity schemes. *IEEE Antennas and Wireless Propagation Letters*, 12:1327–1330, 2013.

[46] L. Luini and C. Capsoni. A physically based methodology for the evaluation of the rain attenuation on terrestrial radio links. In *Proceedings of the Fourth European Conference on Antennas and Propagation*, pages 1–5, April 2010.

[47] C. Capsoni, L. Luini, and M. D'Amico. The multiexcell model for the prediction of the radio interference due to hydrometeor scattering. In *Proceedings of the Fourth European Conference on Antennas and Propagation*, pages 1–5, April 2010.

[48] C. Capsoni, F. Fedi, C. Magistroni, A. Paraboni, and A. Pawlina. Data and theory for a new model of the horizontal structure of rain cells for propagation applications. *Radio Science*, 22(03):395–404, May 1987.

[49] L. Feral, H. Sauvageot, L. Castanet, J. Lemorton, F. Cornet, and K. Leconte. Large-scale modeling of rain fields from a rain cell deterministic model. *Radio Science*, 41(02):1–21, April 2006.

[50] G. Drufuca. Radar-derived statistics on the structure of precipitation patterns. *Journal of Applied Meteorology*, 16(10):1029–1035, 1977.

[51] ITU-R. Recommendation p.838-3: attenuation model for rain for use in prediction methods. Technical report, ITU-R, 2005.

[52] S. Ghirardin, C. Capsoni, and L. Luini. Time evolution of synthetic rain cells for the synthesis of attenuation time series. In *2016 10th European Conference on Antennas and Propagation (EuCAP)*, pages 1–5, April 2016.

[53] ITU-R. Recommendation p.311-15 - acquisition, presentation and analysis of data in studies of radiowave propagation. Technical report, ITU-R, 2015.

[54] Carlo Riva. Seasonal and diurnal variations of total attenuation measured with the italsat satellite at spino d'adda at 18.7, 39.6 and 49.5 ghz. *International Journal of Satellite Communications and Networking*, 22(4):449–476, 2004.

[55] L. M. Tomaz and C. Capsoni. Rain attenuation at low elevation angles: A step towards a leo time series generator. In *12th European Conference on Antennas and Propagation (EuCAP 2018)*, pages 1–5, April 2018.

[56] L. M. Tomaz and C. Capsoni. Analysis of azimuthal variation of rain attenuation. In *2017 SBMO/IEEE MTT-S International Microwave and Optoelectronics Conference (IMOC)*, pages 1–5, Aug 2017.

[57] L. M. Tomaz, L. Luini, and C. Capsoni. Impact of water vapor attenuation on low elevation satcom links. In *2019 13th European Conference on Antennas and Propagation (EuCAP)*, pages 1–5, March 2019.

[58] L. Luini. Modeling and synthesis of 3-d water vapor fields for em wave propagation applications. *IEEE Transactions on Antennas and Propagation*, 64(9):3972–3980, Sep. 2016.

[59] L. Luini and C. G. Riva. Improving the accuracy in predicting water-vapor attenuation at millimeter-wave for earth-space applications. *IEEE Transactions on Antennas and Propagation*, 64(6):2487–2493, June 2016.

[60] L. Luini and C. Capsoni. Modeling high-resolution 3-d cloud fields for earth-space communication systems. *IEEE Transactions on Antennas and Propagation*, 62(10):5190–5199, Oct 2014.

[61] T. Rossi, M. De Sanctis, M. Ruggieri, C. Riva, L. Luini, G. Codispoti, E. Russo, and G. Parca. Satellite communication and propagation experiments through the alphasat q/v band aldo paraboni technology demonstration payload. *IEEE Aerospace and Electronic Systems Magazine*, 31(3):18–27, March 2016.

[62] J. M. Riera, D. Pimienta-del-Valle, P. Garcia-del-Pino, G. A. Siles, and A. Benarroch. Alphasat propagation experiment in madrid: Results on excess and total attenuation. In *2017 11th European Conference on Antennas and Propagation (EUCAP)*, pages 1–4, March 2017.

[63] J. Nessel, J. Morse, M. Zemba, C. Riva, and L. Luini. Performance of the nasa beacon receiver for the alphasat aldo paraboni tdp5 propagation experiment. In *2015 IEEE Aerospace Conference*, pages 1–8, March 2015.

[64] M. Fetescu, , and L. Luini. Private communication. Technical report, Politecnico di Milano, 2019.

[65] ITU-R. Recommendation p.1623-1- prediction method of fade dynamics on earth-space paths. Technical report, ITU-R, 2008.

[66] M. M. J. L. van de Kamp. Statistical analysis of rain fade slope. *IEEE Transactions on Antennas and Propagation*, 51(8):1750–1759, Aug 2003.

[67] C. Kourogiorgas, A. Z. Papafragkakis, P. M. Arapoglou, A. D. Panagopoulos, and S. Ventouras. Total atmospheric attenuation statistics for leo mega-constellations operating at q/v bands. In *2019 13th European Conference on Antennas and Propagation (EuCAP)*, pages 1–5, March 2019.

[68] C. H. Lee, K. Cheung, and C. Ho. A unified low elevation angle scintillation model. In *2011 IEEE International Symposium on Antennas and Propagation (APSURSI)*, pages 821–824, July 2011.

[69] C. I. Kourogiorgas, N. Lyras, A. D. Panagopoulos, D. Tarchi, A. Vanelli-Coralli, A. Ugolini, G. Colavolpe, and P. Arapoglou. Capacity statistics evaluation for next generation broadband meo satellite systems. *IEEE Transactions on Aerospace and Electronic Systems*, 53(5):2344–2358, Oct 2017.

[70] C. I. Kourogiorgas and A. D. Panagopoulos. Space-time stochastic rain fading channel for multiple leo or meo satellite slant paths. *IEEE Wireless Communications Letters*, 7(3):284–287, June 2018.